

**ALGORITHMS FOR CHANNEL ESTIMATION  
AND SPECTRUM SENSING WITH  
IMPLEMENTATION ON SOFTWARE  
DEFINED RADIO**

**Ph.D. Thesis**

*by*

**ABHIJEET BISHNU**



**DISCIPLINE OF ELECTRICAL ENGINEERING  
INDIAN INSTITUTE OF TECHNOLOGY  
INDORE**

**FEBRUARY, 2019**



**ALGORITHMS FOR CHANNEL ESTIMATION  
AND SPECTRUM SENSING WITH  
IMPLEMENTATION ON SOFTWARE  
DEFINED RADIO**

**A THESIS**

*Submitted in partial fulfillment of the  
requirements for the award of the degree*

*of*

**DOCTOR OF PHILOSOPHY**

*by*

**ABHIJEET BISHNU**



**DISCIPLINE OF ELECTRICAL ENGINEERING  
INDIAN INSTITUTE OF TECHNOLOGY  
INDORE**

**FEBRUARY, 2019**







## ACKNOWLEDGEMENTS

There is always a sense of gratitude which one expresses an offer for the helpful and needy services someone renders during all the phases of life. First of all, I would like to thank the Almighty God because He choose this esteemed institute for me without whose blessings I could never achieve this milestone.

I express my heartfelt and profound gratitude to my Ph.D. supervisor Prof. Vimal Bhatia for his invaluable guidance, encouragement, direction throughout my thesis work and specially for his calm nature. It is my great honor and pleasure to work under the esteemed guidance of kind and motivated supervisor like Dr. Vimal Bhatia. I would also like to thank my PSPC committee members Dr. Shaibal Mukherjee and Dr. Somnath Dey for their fruitful discussions and suggestions towards my research.

I am truly thankful to all the faculty members and the staffs of Indian Institute of Technology Indore for their invaluable cooperation throughout my thesis work. I would also like to thank all the members in Signal and Software group (SaSg) for their encouragement and support that helped me to face the hard phase of my life and never letting me feel lonely along this long journey. Specifically, I would like to extend my appreciation to my seniors Dr. Manish Mandloi, Dr. Nagendra Kumar and Dr. Rangeet Mitra. I would also like to extend my appreciation to Sanjeev Sharma, Praveen Kumar Singya and my colleagues who helped me in several ways during my thesis work.

Moreover, whatever little I have achieved in my life, the credit goes to my family members: my parents, my grandparents, my sisters, my uncles and aunts, and cousins whom I take great pride in dedicating this thesis. They have always been a source of inspiration for me and have kept trust and faith in whatever I did.

I would thank Visvesvaraya PhD scheme of Ministry of Electronics and Information Technology, Government of India and IIT Indore for providing financial assistance. I would also take this opportunity to thank Visvesvaraya PhD scheme for funding my conference travels. These conferences helped me meet new people and experts who have helped shape of my PhD thesis.

ABHIJEET BISHNU

*Dedicated to my parents*

## ABSTRACT

Rapid increase in wireless applications and services pose a challenge on the limited licensed spectrum. On the other hand, researchers have found that majority of the licensed spectrum bands in different parts of the world are under-utilized in time, frequency and space. Several researchers around the world through measurements have shown that most of the terrestrial broadcast television (TV) bands in very high frequency (VHF) and ultra-high frequency (UHF) are unoccupied. These vacant/unused channels are known as TV white space (TVWS). The powerful propagation characteristics of VHF/UHF band signals makes these bands suitable for use in rural areas where wired infrastructure is not economical to install, and the line-of-sight wireless solutions are unreliable due to vegetation, nature and man-made features. In 2004, the IEEE 802.22 working group was created to propose protocols for VHF/UHF bands. In September 2006, the working group published functional requirements document for the wireless regional area network (WRAN) system for utilization of TVWS where the WRAN devices act as secondary users (SUs) and digital TV (DTV) acts as primary users (PUs). Hence in this thesis work, channel estimation and spectrum sensing for IEEE 802.22 WRAN (although not limited) standard has been done while considering the challenges posed by TVWS systems and validation of theoretical research on real-time standard implementations. IEEE 802.11ah is also an emerging standard based on orthogonal frequency division multiplexing (OFDM). This standard is introduced for IoT application at sub-1 GHz license-exempt bands. Since large number of IoT devices cause high interference, a receiver structure is proposed for IEEE 802.11ah (although not limited) standard in the presence of interference. The uniqueness of the work is in proposing new algorithms, comparing with existing algorithms and developing analytical insights. The proposed algorithms' performance on practical systems is tested by building a test setup and doing over-the-air real-time testing.

Since the IEEE 802.22 channel is sparse in nature; hence sparse channel estimation algorithms have been proposed in the presence of both Gaussian and non-Gaussian noise. The presence of co-channel and adjacent channel interference in addition to the additive white Gaussian noise can be modeled as non-Gaussian noise. An iterative time-domain based algorithm is proposed for sparse channel estimation in the presence of Gaussian noise. Natural gradient non-parametric maximum likelihood (NG-NPML) algorithm is then proposed for sparse channel estimation in the presence of non-Gaussian noise (due to the presence of co-channel and adjacent channel interference, and impulsive noise). The NG-NPML algorithm converges much faster than the classical stochastic gradient (SG) based NPML. However, the mean square error (MSE) floor is same for both the SG-NPML and the proposed NG-NPML. Thus, to further improve the MSE floor of NG-NPML, an  $l_1$  norm penalty is introduced in the NG-NPML cost function. This  $l_1$  norm penalty introduces a zero-attractor (ZA) term in the NG-NPML weight update recursion which shrinks the coefficients of inactive taps and hence reduces the steady state MSE floor. In addition, the first and second order convergence analysis of both the NG-NPML and ZA-NG-NPML are also derived. The fast convergence of NG-NPML over SG-NPML has been validated by doing the world's first implementation of IEEE 802.22 PHY on National Instruments Universal Software Radio Peripheral (NI-USRP) 2952R in the presence of another IEEE 802.22 transmitter and DTV transmitter as co-channel interference.

IEEE 802.22 is also the first standard which mentions the cognitive radio capability for sensing an active PU. Hence, algorithms for sensing PU's signal in both white Gaussian noise, and colored Gaussian noise are proposed. Grassmann manifold based spectrum sensing is proposed in the presence of white Gaussian noise. Lower bound for the probability of detection of PU's signal is also derived using separating function and distribution of new test statistic. Further, LogDet covariance based spectrum sensing under colored Gaussian noise is proposed. The detection threshold of the proposed algorithm is also derived. Simulation results using real captured data validate performance of the proposed algorithms over existing algorithms, and also validate the derived analytical expressions for the proposed algorithm.

A new OFDM based receiver structure operating in high interference environment is also proposed. The proposed receiver is based on non-parametric maximum likelihood channel estimation followed by Viterbi decoder. Both simulations and real-world experimental results on standard compliant platform show that the proposed algorithm performs better in terms of bit error rate than other receivers in all the considered interference models.

An IEEE 802.22 transceiver framework and its performance analysis on NI-USRP 2952R for TVWS have also been completed. Uniqueness of this work is in building IEEE 802.22 physical layer transceiver. Real measurements of DTV signals was performed in both Delhi and Indore. Implementation of iterative time domain sparse channel estimation algorithm for IEEE 802.22 standard in the presence of Gaussian noise is also completed. The algorithm is implemented on Xilinx Kintex-7 410T FPGA in the NI-USRP 2952R.

# Contents

<b>ABSTRACT</b>	<b>i</b>
<b>LIST OF FIGURES</b>	<b>vii</b>
<b>LIST OF TABLES</b>	<b>xi</b>
<b>LIST OF ABBREVIATIONS</b>	<b>xii</b>
<b>LIST OF SYMBOLS</b>	<b>xii</b>
<b>1 Introduction</b>	<b>1</b>
1.1 Motivation . . . . .	1
1.2 IEEE Standards . . . . .	4
1.2.1 IEEE 802.22 . . . . .	5
1.2.2 IEEE 802.11ah . . . . .	6
1.3 Sparse Channel Models . . . . .	7
1.3.1 COST-207 Typical Urban Channel Model . . . . .	7
1.3.2 Stanford University Interim-6 Channel Model . . . . .	7
1.3.3 International Telecommunication Union Vehicular Channel B Model . . . . .	8
1.3.4 Wireless Regional Area Network Channel Model . . . . .	8
1.4 Universal Software Radio Peripheral 2952R . . . . .	9
1.5 LabVIEW Communication System Design Suite . . . . .	10
1.6 Thesis Contributions and Organizations . . . . .	11
1.7 Organization of Thesis . . . . .	13
<b>2 Sparse Channel Estimation in Presence of Gaussian and non-Gaussian   Noise</b>	<b>15</b>
2.1 Iterative-Time Domain Algorithm . . . . .	17
2.1.1 System Model . . . . .	17
2.1.2 Modified Wiener Filter . . . . .	18
2.1.3 Iterative-Time Domain Algorithm . . . . .	19
2.1.4 Analysis of Threshold ( $\eta$ ) . . . . .	21
2.1.5 Simulation Results and Discussion . . . . .	22
2.2 Natural Gradient Non-Parametric Maximum Likelihood Algorithm . .	24
2.2.1 System Model and Preliminaries . . . . .	24
2.2.2 NG-NPML Algorithm . . . . .	27
2.2.3 Convergence Analysis of NG-NPML . . . . .	29
2.2.4 Simulation Results and Discussion . . . . .	32

2.3	Zero-Attractor Natural Gradient Non-Parametric Maximum Likelihood Algorithm . . . . .	35
2.3.1	ZA-NG-NPML Algorithm . . . . .	35
2.3.2	Convergence Analysis of ZA-NG-NPML . . . . .	36
2.3.3	Simulation Results and Discussion . . . . .	36
2.4	Summary . . . . .	40
<b>3</b>	<b>Spectrum Sensing in Cognitive Radio</b>	<b>41</b>
3.1	System Model . . . . .	44
3.2	Grassmann Manifold based Spectrum Sensing . . . . .	45
3.2.1	Grassmann Manifold . . . . .	45
3.2.2	Proposed Test Statistics . . . . .	47
3.2.3	Distribution Under Two Hypotheses . . . . .	51
3.2.4	Lower Bound for Probability of Detection . . . . .	54
3.2.5	Results and Complexity Discussion . . . . .	56
3.3	LogDet Covariance based Spectrum Sensing under Colored Noise . . . . .	64
3.3.1	LogDet Covariance based Test Statistics . . . . .	64
3.3.2	Analysis Under $\mathcal{H}_0$ . . . . .	66
3.3.3	Simulation Results and Discussion . . . . .	69
3.4	Summary . . . . .	72
<b>4</b>	<b>Non-Parametric Maximum Likelihood based Viterbi Decoder</b>	<b>73</b>
4.1	OFDM based Receiver in Interference Limited Environments . . . . .	74
4.1.1	System Model . . . . .	74
4.1.2	Overview of NPML . . . . .	76
4.1.3	Proposed Receiver Structure . . . . .	77
4.1.4	Results and Discussion . . . . .	79
4.1.5	Experimental Results . . . . .	86
4.2	Summary . . . . .	88
<b>5</b>	<b>Implementation on Software Defined Radio and Field Programmable Gate Arrays</b>	<b>89</b>
5.1	An IEEE 802.22 Transceiver and its Performance Analysis on Software Defined Radio . . . . .	90
5.1.1	IEEE 802.22 Transceiver Implementation and Algorithms . . . . .	90
5.1.2	Results and Discussion . . . . .	94
5.2	FPGA Implementation of Iterative Time-Domain Algorithm . . . . .	99
5.2.1	FPGA Implementation . . . . .	100
5.2.2	Results and Discussion . . . . .	103
5.3	Summary . . . . .	108
<b>6</b>	<b>Conclusion and Future Work</b>	<b>109</b>
6.1	Conclusion . . . . .	109
6.2	Future work . . . . .	110
	<b>Appendix A Derivation of (2.12)</b>	<b>111</b>
	<b>Appendix B Derivation of (2.28)</b>	<b>113</b>

Appendix C Derivation of (2.33)	116
Appendix D Derivation of (2.34)	119
Appendix E Derivation of (2.41)	122
Appendix F Derivation of (3.37)	125
Appendix G Derivation of (3.41)	127
Appendix H Derivation of (4.10)	128
Appendix I Derivation of (4.11)	130
LIST OF PUBLICATIONS	146



# List of Figures

1.1	Application of TV white space [1] . . . . .	2
1.2	Locations for measurement (courtesy: Google maps) . . . . .	3
1.3	Contiguous bandwidth available for a) Mundla Nayta, b) Haryana Khedi and c) Simrol . . . . .	3
1.4	Cumulative distributions of power . . . . .	4
1.5	Block diagram of USRP 2952R © National Instruments . . . . .	10
2.1	mean square error (MSE) vs signal-to-noise ratio (SNR) for Institute of Electrical and Electronics Engineers (IEEE) 802.22 sparse channel estimation under Stanford University Interim (SUI)-6 channel model.	22
2.2	MSE vs SNR for IEEE 802.22 sparse channel estimation under Inter- national Telecommunication Union Vehicular Channel B (ITU-VB) channel model. . . . .	23
2.3	MSE vs SNR for IEEE 802.22 sparse channel estimation under wire- less regional area network (WRAN) channel model. . . . .	24
2.4	System model for channel estimator. . . . .	26
2.5	Transform domain model of Natural gradient (NG)-non-parametric maximum likelihood (NPML) estimator. . . . .	30
2.6	MAE of sparse channel estimation at signal-to-interference ratio (SIR) 5dB and SNR 30dB. . . . .	32
2.7	Theoretical and Monte Carlo simulation of excess MSE (EMSE) of residual error for stochastic gradient (SG)-NPML and NG-NPML at SIR 5dB and SNR 30dB. . . . .	33
2.8	Theoretical and Monte Carlo simulation of MSE of residual error for SG-NPML and NG-NPML at SIR 5dB and SNR 30dB. . . . .	34
2.9	MSE (dB) vs number of iterations under SUI-6 channel model in the presence of impulsive noise as an interferer. . . . .	37
2.10	MSE (dB) vs number of iterations under SUI-6 channel model in the presence of IEEE 802.22 as an interferer. . . . .	38
2.11	MSE (dB) vs number of iterations under WRAN channel model in the presence of impulsive noise as an interferer. . . . .	39
2.12	MSE (dB) vs number of iterations under WRAN channel model in the presence of IEEE 802.22 as an interferer. . . . .	39
3.1	Values of $\rho$ under two hypotheses from 1000 simulations. . . . .	49
3.2	(a) Concentration phenomena of $\rho$ under $\mathcal{H}_0$ and (b) Concentration phenomena of $\rho$ under $\mathcal{H}_1$ . . . . .	50

3.3	(a) Comparison of simulated and theoretical probability density function (PDF)s of $\rho$ under $\mathcal{H}_0$ , (b) Comparison of simulated and theoretical PDFs of $\rho$ under $\mathcal{H}_1$ . . . . .	51
3.4	ROC curves of proposed and conventional methods at -20dB SNR. . . . .	57
3.5	$P_d$ of proposed and conventional method with $P_f$ of 0.01. . . . .	57
3.6	Comparison of simulated and theoretical (a) $P_f$ of proposed method with threshold and (b) $P_d$ of proposed method with $P_f$ of 0.01 and 0.1. . . . .	58
3.7	Comparison of lower bound of $P_d$ with $P_f$ of 0.01 using SF1 and SF2. . . . .	59
3.8	$Q_d$ of proposed method for different values of $N_c$ at $P_f = 0.05$ . . . . .	59
3.9	Comparison of simulated and theoretical $Q_d$ at $P_f = 0.05$ for (a) $N_c = 2$ , (b) $N_c = 3$ and (c) $N_c = 4$ . . . . .	60
3.10	Comparison of lower bound of $Q_d$ at $P_f = 0.05$ using SF1 and SF2 for (a) $N_c = 2$ , (b) $N_c = 3$ and (c) $N_c = 4$ . . . . .	61
3.11	Experimental setup for (a) local spectrum sensing and (b) cooperative spectrum sensing. . . . .	62
3.12	(a) $P_d$ vs average RSS of proposed method, (b) $Q_d$ vs average RSS of proposed method for 2 secondary user. . . . .	63
3.13	$P_d$ vs SNR of signal capture in USA for white noise at $P_f=0.05$ . . . . .	70
3.14	$P_d$ vs SNR of signal capture in USA for colored noise at $P_f=0.05$ . . . . .	70
4.1	Block diagram of orthogonal frequency division multiplexing (OFDM) based transceiver. . . . .	75
4.2	PDF of non-Gaussian noise process. . . . .	76
4.3	Proposed OFDM based receiver structure. . . . .	77
4.4	bit error rate (BER) vs SIR at 30 dB SNR for IEEE 802.15.4 device as an interferer for binary phase-shift keying (BPSK) modulated data with cyclic prefix (CP) of length 8. . . . .	80
4.5	BER vs SIR at 30 dB SNR for IEEE 802.15.4 device as an interferer for BPSK modulated data with CP of length 16. . . . .	81
4.6	BER vs GSIR at 30 dB SNR for impulsive noise as an interferer for BPSK modulated data with CP of length 8. . . . .	82
4.7	BER vs GSIR at 30 dB SNR for impulsive noise as an interferer for BPSK modulated data with CP of length 16. . . . .	82
4.8	BER vs SIR at 30 dB SNR for IEEE 802.15.4 device as an interferer for quadrature phase-shift keying (QPSK) modulated data with CP of length 8. . . . .	83
4.9	BER vs SIR at 30 dB SNR for IEEE 802.15.4 device as an interferer for QPSK modulated data with CP of length 16. . . . .	84
4.10	BER vs SIR at 30 dB SNR for impulsive noise as an interferer for QPSK modulated data with CP of length 8. . . . .	84
4.11	BER vs SIR at 30 dB SNR for impulsive noise as an interferer for QPSK modulated data with CP of length 16. . . . .	85
4.12	Experimental Setup. . . . .	85
4.13	BER vs SIR at 30 dB SNR for IEEE 802.15.4 device as an interferer for BPSK modulated data. . . . .	87
4.14	BER vs SIR at 30 dB SNR for IEEE 802.15.4 device as an interferer for QPSK modulated data. . . . .	87
5.1	Block diagram of IEEE 802.22 transceiver . . . . .	91

5.2	Execution time of (a) Various blocks of IEEE 802.22 and; (b) Comparison of different encoding and decoding technique for QPSK modulation with scrambling. . . . .	95
5.3	Execution time of (a) Comparison of different encoding and decoding technique for 16-QAM modulation with scrambling and; (b) Comparison of different encoding and decoding technique for 64-QAM modulation with scrambling. . . . .	96
5.4	QPSK modulation: (a) Signal constellation diagram after channel equalization at 12 dB Eb/No and; (b) BER vs SNR for convolutional codes (CC) and low density parity check (LDPC) . . . . .	97
5.5	16-QAM modulation: (a) Signal constellation diagram after channel equalization at 15.7 dB Eb/No and; (b) BER vs SNR for CC and LDPC . . . . .	98
5.6	64-QAM modulation: (a) Signal constellation diagram after channel equalization at 18.4 dB Eb/No and; (b) BER vs SNR for CC and LDPC . . . . .	99
5.7	Flow chart of ITD algorithm . . . . .	100
5.8	Top level Graphical Virtual Instrument of ITD algorithm using NI-LabVIEW CSDS on NI-USRP 2952R. . . . .	101
5.9	(a) Parallel FIR filter processing, and (b) Parallel block processing . .	104
5.10	BER vs SNR for QPSK modulation . . . . .	105
5.11	BER vs SNR for 16-quadrature amplitude modulation (QAM) modulation . . . . .	105
5.12	BER vs SNR for 64-QAM modulation . . . . .	106



# List of Tables

1.1	Parameters for COST-207 TU channel model . . . . .	8
1.2	Parameters for SUI-6 channel model . . . . .	8
1.3	Parameters for ITU-VB channel model . . . . .	8
1.4	Parameters for WRAN channel model . . . . .	9
4.1	Simulation parameters . . . . .	79
5.1	System configuration . . . . .	95
5.2	Comparison of resource utilization of Xilinx Kintex-7 410T FPGA by cross-correlation of real value and complex value . . . . .	103
5.3	Simulation parameters . . . . .	104
5.4	Comparison of resource utilization of Xilinx Kintex-7 410T field pro- grammable gate array (FPGA) by Iterative time-domain (ITD) algo- rithm with serial and parallel block processing . . . . .	107
5.5	Clock cycle consumed by various stages of ITD algorithm with serial and parallel block processing . . . . .	107



# List of Abbreviations

**AWGN** additive white Gaussian noise.

**BER** bit error rate.

**BPSK** binary phase-shift keying.

**BS** base station.

**CC** convolutional codes.

**CFO** carrier frequency offset.

**CIR** channel impulse response.

**CP** cyclic prefix.

**CPEs** customer premises equipment.

**CR** cognitive radio.

**CSDS** Communication System Design Suite.

**DTV** digital television.

**ELDRSCM** energy with LDRSCM.

**EMSE** excess MSE.

**FEC** forward error correcting.

**FFT** fast Fourier transform.

**FPGA** field programmable gate array.

**GCM** Grassmann covariance matrix.

**GI** guard interval.

**i.i.d.** independent and identically distributed.

**IEEE** Institute of Electrical and Electronics Engineers.

**IFFT** inverse FFT.

**IoT** Internet of Things.

**ISI** inter-symbol interference.

**ITD** Iterative time-domain.

**ITU-VB** International Telecommunication Union Vehicular Channel B.

**LabVIEW** Laboratory Virtual Instrument Engineering Workbench.

**LANs** local area networks.

**LDPC** low density parity check.

**LDRSCM** LogDet of received samples covariance matrix.

**LMS** least mean square.

**LS** least square.

**LTS** long training sequence.

**MIMO** multi-input multi-output.

**MMSE** minimum MSE.

**MSD** mean square deviation.

**MSE** mean square error.

**NG** Natural gradient.

**NI** National Instruments.

**NPML** non-parametric maximum likelihood.

**OFDM** orthogonal frequency division multiplexing.

**OFDMA** orthogonal frequency division multiple access.

**PDF** probability density function.

**PHY** physical layer.

**PU** primary user.

**QAM** quadrature amplitude modulation.

**QPSK** quadrature phase-shift keying.

**RF** radio frequency.

**SCH** superframe control header.

**SDR** software defined radio.

**SG** stochastic gradient.

**SIR** signal-to-interference ratio.

**SNR** signal-to-noise ratio.

**SS** spectrum sensing.

**STS** short training sequence.

**SU** secondary user.

**SUI** Stanford University Interim.

**SVD** singular value decomposition.

**TU** Typical Urban.

**TVWS** TV white space.

**UHF** ultra high frequency.

**USRP** Universal Software Radio Peripheral.

**VHF** very high frequency.

**WLAN** wireless local area network.

**WM** wireless microphone.

**WRAN** wireless regional area network.

**ZA** zero attractor.

# List of Symbols

$\hat{\mathbf{h}}_k$  estimated channel coefficients vector of dimension  $L \times 1$  at  $k^{th}$  iteration.

$\mu$  step-size.

$\sigma_w^2$  variance of additive white Gaussian noise.

$\xi_\infty$  steady state mean square error.

$\zeta_\infty$  steady state mean square deviation.

$\xi_0$  minimum mean square error.

$\sigma_k$  kernel width.

$L$  length of channel coefficients.

$L_{cp}$  length of cyclic prefix.

$N$  number of subcarriers.

$P_d$  probability of signal detection.

$P_f$  probability of false alarm.

$X(k_c)$  transmitted signal at  $k_c^{th}$  subcarrier.

$Y(k_c)$  received signal at  $k_c^{th}$  subcarrier.

$e(n)$  residual error at  $n^{th}$  time instant.

$i(n)$  interference signal at  $n^{th}$  time instant.

$v(n)$  Gaussian mixture noise at  $n^{th}$  time instant.

$w(n)$  additive white Gaussian noise  $n^{th}$  time instant.

$x(n)$  transmitted signal at  $n^{th}$  time instant.

$y(n)$  received signal at  $n^{th}$  time instant.

$\mathbf{G}_k$  Riemannian metric tensor  $k^{th}$  iteration.

$\mathbf{h}$  true channel coefficients vector of dimension  $L \times 1$ .

$\mathbf{R}_{ww}$  covariance matrix of  $w(n)$ .

$\mathbf{R}_{xx}$  covariance matrix of  $x(n)$ .

$\mathbf{R}_{yy}$  covariance matrix of  $y(n)$ .

$\mathbf{x}(n)$  transmitted signal vector at  $n^{th}$  time instant.

$\mathbf{y}(n)$  received signal vector at  $n^{th}$  time instant.



# Chapter 1

## Introduction

### 1.1 Motivation

With exponential rise in the number of wireless devices using the same limited licensed spectrum poses a great challenge. Several researchers around the world have found that, most licensed bands are either unused or underused [2]. In [3], the researchers have shown that in rural and remote areas, majority of TV band is vacant. These vacant bands are referred to as TVWS. Further, newer TV bands has been made vacant after digital switch over in the UK, Germany, Australia, Singapore [4], and other countries. The powerful propagation characteristics of VHF/UHF signals make them ideal for use in rural areas where wired infrastructure is not cost effective to deploy, and vegetation makes line-of-sight wireless solutions unreliable. In 2004, the IEEE 802.22 working group was created and published the functional requirements documents for the WRAN system in September 2006 [5]. There is later amendment in 2011 in physical layer of IEEE 802.22-2011 standards to support enhanced broadband services and monitoring applications [6], and further enhancement to this evolving standard is in draft [7]. In [8], the performance of IEEE 802.22-2011 network is evaluated in the presence of wireless microphone. Apart from IEEE 802.22, different working group such as IEEE 802.15.4m and IEEE 802.19.1 of IEEE 802 family have proposed standard for TVWS communication [9].

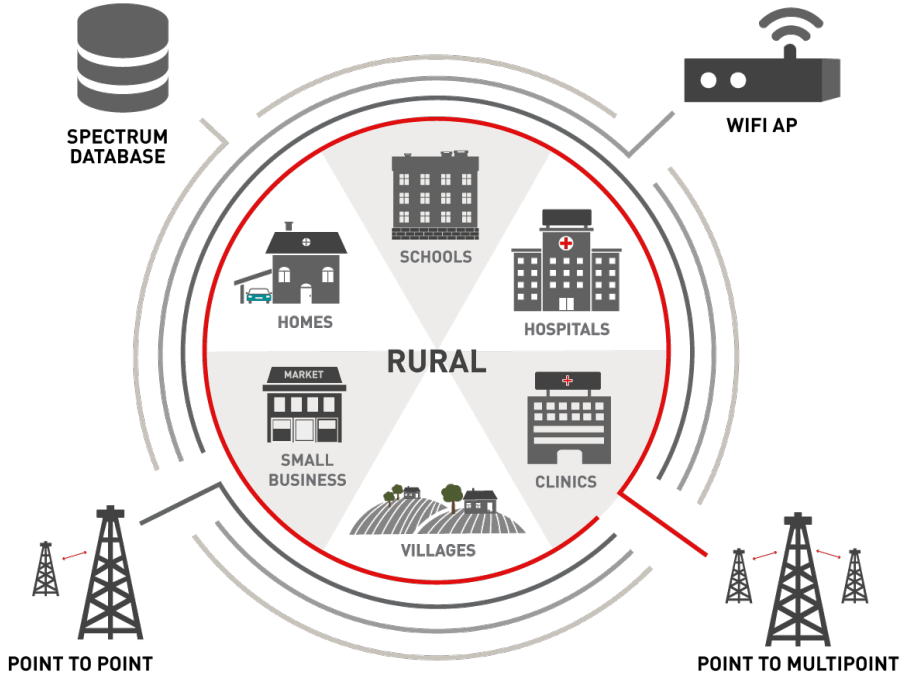


Figure 1.1: Application of TV white space [1]

Additionally, IEEE Dyspan standards committee has proposed IEEE 1900.x standard for TVWS communication [9]. The application of TVWS are in smart grid and monitoring, broadband service extension, environmental monitoring, critical infrastructure and monitoring, homeland security, smart traffic management, emergency broadband infrastructure, remote medical services, marine broadband services etc. [1] as shown in Figure 1.1.

In Maharashtra, India, based on measurements, 80-85 % TV band is vacant in rural areas [10]. The availability of TV white space (TVWS) from 400-900 MHz at different times is measured in Indore, India. The readings were taken at suburban and rural areas around Indore (India), which represents significant area of Central India. There are about 650 villages and rural communities which are sparsely populated in distributed communities over a coverage area of 4500 square kilometer. Thus this region is appropriate for adoption of survey of white space, with Indore serving the nearby villages and rural communities using TVWS. The locations are sub-urban Mundla Nayta (Indore) where some residential area is located including Silver Spring township, rural Harnya Khedi village where IIT Indore was located and another rural Simrol village where IIT Indore permanent campus is located. The

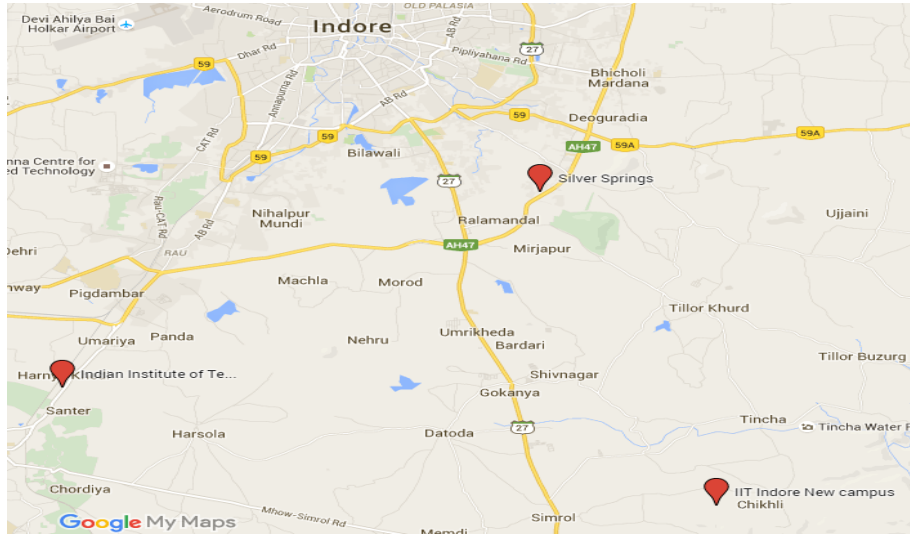


Figure 1.2: Locations for measurement (courtesy: Google maps)

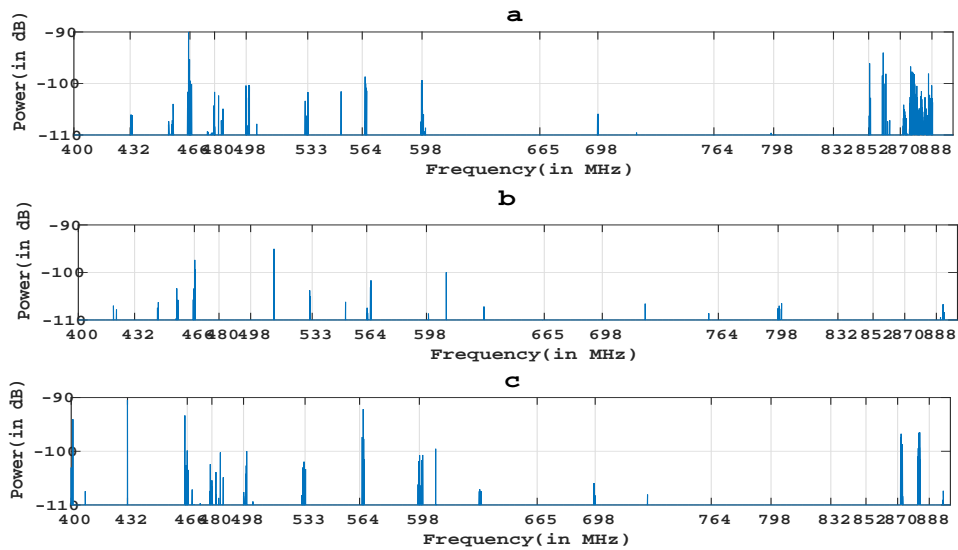


Figure 1.3: Contiguous bandwidth available for a) Mundla Nayta, b) Harnya Khedi and c) Simrol

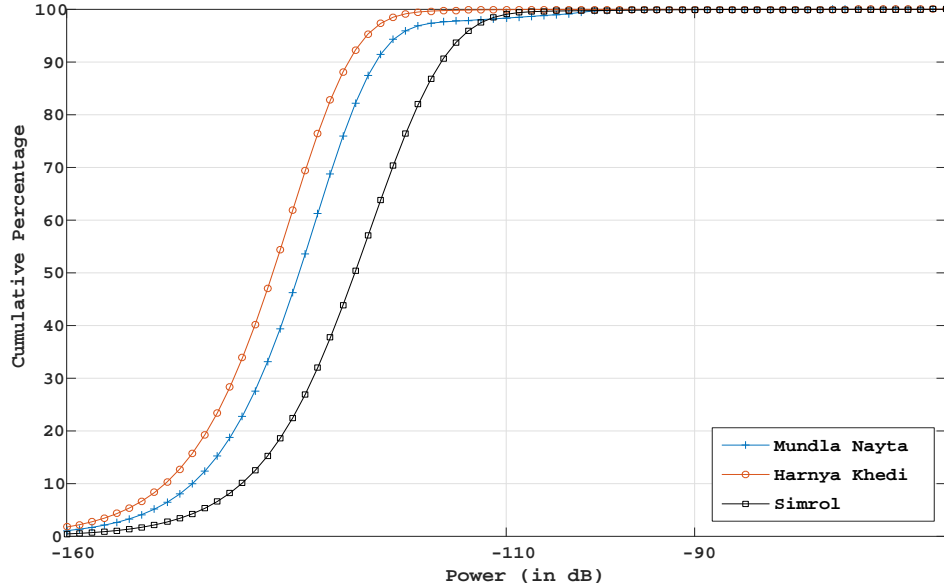


Figure 1.4: Cumulative distributions of power

experimental locations are shown in Figure 1.2. These locations form a triangle and are approximately 20 KM away from each other. Figure 1.3 shows the contiguous bandwidth available for the considered locations. It is observed from Figure 1.3 that the maximum contiguous bandwidth 140 MHz (710 MHz - 850 MHz), 100 MHz (620 MHz - 720 MHz) and 160 MHz (710 MHz - 870 MHz) are available for Mundla Nayta, Harnya Khedi and Simrol, respectively. Fig. 1.4 shows that cumulative distribution of power (cumulative percentage at -115 dBm) which shows that 92%, 98% and 96% of bandwidth is available in Simrol, Harnya Khedi and Mundla Nayta, respectively. Hence, there is a vast availability of white space bands, that may be utilized for wireless communication for rural broadband. In the next section, different IEEE standards are discussed which are used as receiver to validate the various proposed algorithms presented in the subsequent chapters.

## 1.2 IEEE Standards

In this section a brief overview of physical layer of IEEE 802.22 and IEEE 802.11ah is presented which are later used for validation of proposed algorithms and techniques.

### 1.2.1 IEEE 802.22

The IEEE 802.22 standard is envisaged for providing wireless access to rural areas of 17-30 KM of radius or more, and may cover upto 100 KM depends on propagation condition. It provides minimum peak data rate of 1.5 Mbps in downlink (base station (BS) to customer premises equipment (CPEs)) and 384 Kbps in uplink (CPEs to BS). One BS may support upto 255 CPEs with outdoor directional antennas of height 10 meter above the ground level similar to very high frequency (VHF)/ultra high frequency (UHF) TV receiving antenna [11]. The IEEE 802.22 physical layer is relatively closest to IEEE 802.16e among IEEE 802 family. The IEEE 802.22 is based on single air interface of orthogonal frequency division multiple access (OFDMA)). Since IEEE 802.22 is an evolving standard, initially IEEE 802.22 defines time division duplex (TDD) however in future it may support frequency division duplex (FDD) [11].

The IEEE 802.22 system supports various TV channel bandwidths (6, 7 and 8 MHz), various sampling frequency, symbol duration etc. these are detailed below. The OFDMA symbols are created using 2048 fast Fourier transform (FFT) with 1440 data subcarriers, 240 pilot subcarriers and 368 null subcarriers including direct current (DC) [11]. It supports CP of length  $1/4$ ,  $1/8$ ,  $1/16$  and  $1/32$  of symbol duration according to channel delay and spectrum efficiency. There are 60 subchannels in each OFDM symbol consisting of 24 data subcarriers and 4 pilot subcarriers. The IEEE 802.22 defines 12 modes for data communication using three modulations (QPSK, 16-QAM, 64-QAM) with four code rates ( $1/2$ ,  $2/3$ ,  $3/4$ ,  $5/6$ ). The standard defines the only mandatory forward error correcting (FEC) codes is the CC with rate of  $1/2$  and constraint length of 7. The output of the convolutional coder can be punctured to obtain different coding rates. Duo-binary convolutional turbo codes, shorten block turbo codes and LDPC codes are optional advanced FEC to provide better performance [11].

The data transmission is in the form of superframe of 160 ms and each super-

frame consists of frame with 10 ms. The first frame of each superframe consists of superframe preamble, frame preamble, superframe control header (SCH) and then frame payload as per specification [6]. The superframe preamble consists of short training sequence (STS) with CP of 1/4 with BPSK modulation and it is used for frame detection. The frame preamble consists of long training sequence (LTS) with CP of 1/4 is also BPSK modulated. The LTS is used for channel estimation and carrier frequency offset (CFO) estimation. The SCH provides information about the IEEE 802.22 BS, support self-coexistence mechanisms, and support the intraframe and inter-frame mechanisms for management of quiet periods for spectrum sensing (SS). The SCH is QPSK modulated with coding rate of 1/2 and four repetitions. The STS and LTS are known *a priori* at the receiver.

### 1.2.2 IEEE 802.11ah

IEEE 802.11ah is an emerging standard for wireless local area network (WLAN) operating at sub-1-GHz license-exempt bands and is based on OFDM [12]. This standard combines the advantages of Wi-Fi and low power sensor network communication technologies. The IEEE 802.11ah can provide large transmission range (up to 1 km) as compared to the conventional IEEE 802.11 WLANs. This standard is available for radio transmission in some areas, including China, Europe, Japan, Singapore, South Korea, and the USA. The IEEE 802.11ah can be used for various services including large scale sensor and smart meter networks, outdoor extended Wi-Fi, and IoT applications [13].

The IEEE 802.11ah can support data rates ranging from 150 Kbps to 347 Mbps. The minimum data rate is achieved for 1 MHz bandwidth with BPSK modulation, 32 point FFT, a coding rate of 1/2 and single spatial stream. While the maximum data rate is achieved for 16 MHz bandwidth with 256-QAM, 512 point FFT, a coding rate of 5/6 and  $4 \times 4$  multi-input multi-output (MIMO) [14]. IEEE 802.11ah defines 2 MHz, 4 MHz, 8 MHz, and 16 MHz channels which are exactly ten times down-clocked of IEEE 802.11ac channels [15]. IEEE 802.11ah standard [14] uses 32,

64, 128, 256 and 512 point FFT for 1, 2, 4, 8 and 16 MHz bandwidth, respectively. IEEE 802.11ah defines BPSK modulation, QPSK modulation, 16-QAM, 64-QAM and 256-QAM with the combinations of the code rate of 1/2, 2/3, 3/4, and 5/6. The guard interval (GI) duration is 8  $\mu$ s and 4  $\mu$ s for short GI, respectively. The OFDM symbol duration with long GI is 40  $\mu$ s, and 36  $\mu$ s for short GI, respectively. The short training field duration and the long training field duration are at 160  $\mu$ s which have been selected for robustness against multipath fading over long distances [13].

### 1.3 Sparse Channel Models

The channel impulse response (CIR) of a sparse channel is characterized by a few significant channel taps or active taps (or non-zero taps), and majority of zero (or nearly zero) or non-active channel taps. This sparse channel, typically occurs in OFDM based WRAN IEEE 802.22 [16], in Long-Term Evolution (LTE)-Advanced [17], in digital television (DTV) transmission [18], and in millimeter wave MIMO channel for 5G [19]. In this section, a brief overview of some standard channel models considered in this thesis are presented below.

#### 1.3.1 COST-207 Typical Urban Channel Model

The COST-207 channel models are based on 8-10 MHz channel bandwidth in UHF band used for global system for mobile communication. Further this model is also applicable for wideband code division multiple access channel characterisation. The COST-207 Typical Urban (TU) channel model [20] is a non-exponentially decaying and non line of sight channel model with six active taps of 41 taps at 8 MHz sampling rate as given in Table 1.1.

#### 1.3.2 Stanford University Interim-6 Channel Model

The SUI-6 channel model [21] is an exponentially decaying and non-line of sight channel model with three active taps of 121 taps at 8 MHz sampling rate as given

Table 1.1: Parameters for COST-207 TU channel model

Tap#	Delay( $\mu$ s)	Power(dB)
1	0	-3
2	0.2	0
3	0.6	-2
4	1.6	-6
5	2.4	-8
6	5	-10

Table 1.2: Parameters for SUI-6 channel model

Tap#	Delay( $\mu$ s)	Power(dB)
1	0	0
2	14	-10
3	20	-14

in Table 1.2.

### 1.3.3 International Telecommunication Union Vehicular Channel B Model

The ITU-VB channel model [21] is specified in ITU-R recommendation M.1225. This channel model is non-exponentially decaying channel model with six active taps of 121 taps at 8 MHz sampling rate as given in Table 1.3.

### 1.3.4 Wireless Regional Area Network Channel Model

The WRAN channel model [16] is non-exponentially decaying channel model with six active taps of 112 taps at 8 MHz sampling rate as given in Table 1.4.

Table 1.3: Parameters for ITU-VB channel model

Tap#	Delay( $\mu$ s)	Power(dB)
1	0	-2.5
2	0.3	0
3	8.9	-12.8
4	12.9	-10
5	17.1	-25.2
6	20	-16

Table 1.4: Parameters for WRAN channel model

Tap#	Delay( $\mu$ s)	Power(dB)
1	0	-6
2	3	0
3	5	-7
4	7	-22
5	10	-16
6	14	-20

## 1.4 Universal Software Radio Peripheral 2952R

In this section, a brief overview of National Instruments (NI) Universal Software Radio Peripheral (USRP) 2952R is presented using which experimental results are obtained.

The NI-USRP 2952R<sup>1</sup> is used as the peripheral equipment due to its maximum sampling rate of 400 MS/s at the transmitter and 120 MS/s at the receiver, which can be adjusted as per the sampling rate defined in IEEE 802.22 standard. It also supports vast frequency range from 400 MHz to 4.4 GHz with maximum of 120 MHz instantaneous real time bandwidth. The block diagram of USRP 2952R is shown in Fig. 1.5. The major components of USRP 2952R are: the NI-STC3, the FPGA module, analog-to-digital converter (ADC)/ digital-to-analog converter (DAC), and the radio frequency (RF) front-end. The NI-STC3 timing and synchronization technology delivers the advanced digital, triggering, timing, synchronization, bus-mastering, and counter/timer features to this device. The Kintex-7 FPGA is a reconfigurable Laboratory Virtual Instrument Engineering Workbench (LabVIEW) FPGA target that includes digital signal processor (DSP) 48 co-processing for low-latency, and high data rate applications like 3G and 4G wireless, flat panel displays, and video over IP solutions. The USRP 2952R has 16 bit resolution with 80 dB spurious-free dynamic range (sFDR) DAC and 14 bit resolution with 88 dB sFDR ADC. The RF section deals with frequency conversion and band selection. The digital base-band signal is transferred to/from host computer from/to USRP with the help of

<sup>1</sup><http://www.ni.com/pdf/manuals/376326a.pdf>

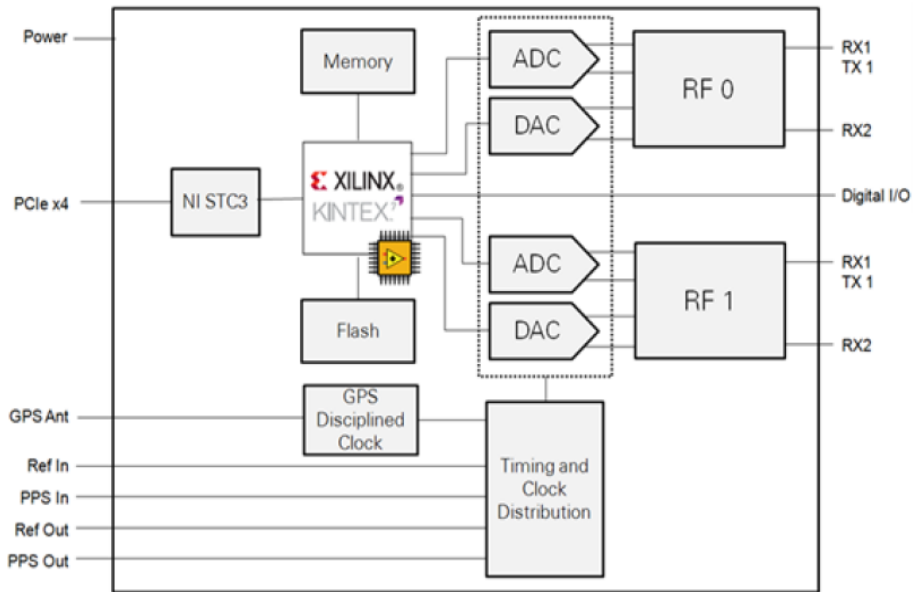


Figure 1.5: Block diagram of USRP 2952R © National Instruments

MXI-Express x4 cable and PCIe-8371 interface card.

## 1.5 LabVIEW Communication System Design Suite

All baseband signal processing of the IEEE 802.22 and IEEE 802.11ah standard are implemented on LabVIEW Communication System Design Suite (CSDS). To program the USRP transceiver, one can use either the NI-USRP application program interface (API) with LabVIEW and LabVIEW FPGA, or LabVIEW CSDS.

LabVIEW Communications provides two programming driver API approaches for the USRP. The host API provides consistent continuity with device for applications running on the general purpose processor (GPP) using the NI-USRP driver. The host API integrates the common open, configure, read/write, close architecture across the LabVIEW platform used for host-based drivers. The USRP RIO Instrument Design Library (IDL) delivers a consistent programming experience for intensify performance and configurability to fulfill more demanding speed, latency, and throughput requirements from the host all the way down to low-level FPGA processing. LabVIEW Communications also offers tools like float to fixed conversion and multirate diagram to faster the process of developing algorithms for the FPGA.

LabVIEW Communications offers upgraded text-based support with text integration nodes. One can use (.c) code and MATLAB (.m) code into the text integration node to rapidly prototype the existing algorithms on USRP hardware. User defined functions can be built or import for .m files.

## 1.6 Thesis Contributions and Organizations

IEEE 802.22 WRANs are designed to operate in the TV bands while ensuring that no harmful interference is caused to the incumbent services such as DTV and low power wireless microphones. The objective of IEEE 802.22 WRAN standard is to allow sharing of unused spectrum allocated to the TV services on a non-interfering basis using cognitive radio techniques, to bring broadband access to rural environments, and is therefore timely and has the potential for worldwide applicability. Since, the communication channel for IEEE 802.22 is sparse in nature and also includes the cognitive radio capability to sense the primary users' signal such as DTV. Thus, in the thesis, sparse channel estimation algorithms have been proposed in the presence of both the Gaussian and non-Gaussian noise. Additionally, SS algorithms are proposed under both white and colored Gaussian noise. Further, OFDM based IEEE 802.11ah are designed for IoT applications operating at sub-1 GHz license-exempt bands. Since large number of IoT devices cause high interference, modified Viterbi decoder is proposed in the presence of interference.

The contribution of this thesis include;

1. ITD algorithm based on adaptive thresholding and least mean square (LMS) is proposed for sparse channel estimation in the presence of Gaussian noise and derivation of analytical expressions of the threshold. The proposed algorithm initially estimates the active channel taps with the help of cross-correlation of the received signal and transmitted preamble. Then an iterative algorithm based on adaptive thresholding and least mean square is used in the time domain for sparse channel estimation. Further, FPGA implementation of

the ITD algorithm is also presented using NI LabVIEW CSDS algorithmic compiler. The algorithmic compiler in the NI LabVIEW CSDS converts the high-level description of entire algorithm to very high speed integrated circuit hardware description language. Actual usage of FPGA's resources such as slices, look up tables and others are also provided for implementation of the considered algorithm.

2. NG-NPML and zero attractor (ZA)-NG-NPML algorithms are proposed for sparse channel estimation in the presence of non-Gaussian noise. In the NG-NPML algorithm, a quadratic warping transformation on the channel coefficients space is proposed which transforms the channel coefficients space from Euclidean space to Riemannian space where NG is applied. In addition, convergence analysis of the proposed NG-NPML algorithm is also presented with derivation of analytical expression for the steady-state MSE. Further, convergence analysis of ZA-NG-NPML algorithm is also presented.
3. Grassmann manifold based test statistic is proposed for primary user (PU)'s signal detection under white Gaussian noise. In this method, Grassmann covariance matrix (GCM) is formed with the help of covariance matrix of the transmitted and the received symbols. By using GCM, a new test statistic is defined which is used to detect the PU's signal. Further, the distribution of new test statistic under null hypothesis and alternative hypothesis is derived. Lower bound for the probability of detection of signal is also derived using separating function and distribution of new test statistic. Experimental verification on NI-USRP 2952R is also performed and it is found that the proposed method fulfills the requirement of maximum protection of the DTV signal as specified in the standard. In addition, LogDet covariance based PU's signal detection is also proposed under colored Gaussian noise. In this method, LogDet of covariance of received samples is used for detecting PU's signal. The LogDet method works extremely well at low signal-to-noise ratio in the presence of both white and colored noise. The detection threshold of the proposed

LogDet based algorithms is also derived.

4. The residual error distribution based branch metric update for Viterbi algorithm is proposed in the presence of interference limited environment. The Viterbi decoder's branch metric is updated based on the distribution of residual error. The proposed receiver structure is tested on IEEE 802.11ah based receiver in the presence of IEEE 802.15.4 device, and impulsive noise as interferer. In addition, analytical expression for the probability of symbol error is also derived.
5. An implementation framework for physical layer of IEEE 802.22 WRAN standard for normal mode is demonstrated. Different blocks of standard IEEE 802.22 receiver based on their execution time are also analyzed, and critical blocks of IEEE 802.22 that should be optimized for real-time applications for commercial product development and field deployments are identified. This work highlighted the difference between theoretical and practical performance of the considered error control codes for IEEE 802.22 specified block size.

## 1.7 Organization of Thesis

This thesis consists of Chapters 1 to 6, whose brief description is as follows:

**Chapter 1. Introduction :** In this chapter, a brief introduction about, TVWS, IEEE standards, sparse channel model, USRP 2952R, motivation, and main contributions of the thesis are provided.

**Chapter 2. Sparse Channel Estimation in the Presence of Gaussian and non-Gaussian noise :** In this chapter, algorithms for sparse channel estimation in the presence of both Gaussian and non-Gaussian noise are proposed. Further, analytical expressions of MSE, and EMSE are derived.

**Chapter 3. Spectrum Sensing in Cognitive Radio :** In this chapter, algorithms are proposed for PU's signal detection in the presence of white and colored Gaussian noise. Further, threshold for signal detection and lower bound on signal detection are also derived.

**Chapter 4. Non-Parametric Maximum Likelihood based Viterbi Decoder :** This chapter presents the residual error distribution based Viterbi decoder metric branch update in the presence of interference and impulsive noise. Further, analytic expression of symbol error for BPSK and QPSK is derived. In addition, experimental validation of robustness of the proposed algorithm is also presented.

**Chapter 5. Implementation on Software Defined Radio and Field Programmable Gate Arrays :** In this chapter, an IEEE 802.22 transceiver framework and its performance analysis on software defined radio (SDR) for TVWS is presented. Further, FPGA implementation of ITD algorithm is also presented using NI LabVIEW CSDS compiler.

**Chapter 6. Conclusion and Future Work:** In this chapter, the conclusions made from proposed algorithms in this thesis are summarized, and suggestions for future research are provided.

## Chapter 2

# Sparse Channel Estimation in Presence of Gaussian and non-Gaussian Noise

Sparse communication channel, typically occurs in OFDM based WRAN IEEE 802.22 [11], LTE-Advanced [17], and DTV transmission [18]. This also occurs in millimeter wave MIMO channel for 5G [19] because of large number of channel taps. After encouraging results in sparse signal processing observed in [22], there has been an interest to exploit sparsity in CIR estimation in the presence of Gaussian noise. Xie et. al. in [23], proposed threshold based taps detection for sparse channel in which (noise) standard deviation based thresholding is applied with least square (LS) to get accurate estimates. In [24], joint time-frequency sparse channel estimation has been proposed which is based on the sparsity adaptive simultaneous orthogonal matching pursuit (SA-SOMP). In [25], a  $p$ -norm constrained least mean fourth (PNC-LMF) algorithm has been proposed. However, the performance of PNC-LMF algorithm is poor for large channel order. Li et. al. in [26], proposed a low-complexity norm-adaption least-mean-square/fourth (LCNA-LMS/F) algorithm to exploit the sparse properties of the wireless channel. Again this algorithm has poor performance for large channel order. In addition, proportionate

normalized LMS (PNLMS) [27] and its various variants [28, 29] had been proposed in which each tap coefficient is updated independently by a step size that is proportional to the magnitude of the coefficient. An alternative approach in separate development has been proposed which favors sparsity by introducing  $l_1$  norm penalty in the cost function [30]. This results in a modified PNLMS update equation with ZA, named as ZAPNLMS algorithm. The presence of the ZA results in shrinkage of the coefficients, especially the inactive taps, thereby leading to lower steady state MSE for sparse systems.

Further, wireless communication channels are highly affected by interference from both the co-channel interference (CCI) [31] and adjacent channel interference due to the extensive growth of wireless services and applications. These interferences along with additive white Gaussian noise (AWGN) can be jointly modeled as Gaussian mixture noise which is non-Gaussian in nature [32]. In addition to interference in the radio channel, the example of non-Gaussian noise sources include symmetric alpha-stable noise [33], double talk in echo cancellation [34], biological noise [35] in the underwater acoustic channels, and variety of natural and man-made sources [36]. SG based NPML adaptive algorithm gives better channel estimates in the presence of Gaussian mixture noise [32]. In the SG-NPML based channel estimator, first, the error signal (which is a Gaussian mixture) is estimated, then the PDF of this error signal is estimated with the help of kernel density estimators [32] and finally, the gradient of the cost function [32] is applied iteratively to approach maximum likelihood estimate. This resulting channel estimate has lower MSE than LSs based channel estimator in the interference limited channels. For sparse channels, SG-NPML based adaptive channel estimation requires a large number of iterations for convergence, and hence increases computational cost of the system. In literature, there are various sparse channel estimators including least absolute shrinkage and selection operator (LASSO) [37], matching pursuit (MP) [38] orthogonal MP (OMP) [39], maximum correntropy criterion (MCC) [40], and maximum versoria criterion (MVC) [41] based channel estimation which have low computational complexity as

compared to SG-NPML. The LASSO, MP, and OMP have good MSE performance in the presence of Gaussian noise, if *a priori* knowledge of an exact number of active taps is provided. However, MSE floor increases for LASSO, MP, and OMP for an interference limited sparse channel, thereby rendering them unsuitable for channel estimation. In [42], sparsity-aware normalized MCC (SA-NMCC) has been proposed which gives lower MSE floor as compared to normalized MCC for sparse channel estimation. However, SA-NMCC and MVC algorithms require very large number of iterations for sparse channel estimation.

This chapter has been organized in three parts: In the first part, an ITD based sparse channel estimation is proposed in the presence of Gaussian noise. The proposed ITD algorithm outperforms various existing algorithms in terms of MSE. In the second part, NG-NPML based sparse channel estimation is proposed in the presence of non-Gaussian noise. The proposed NG-NPML channel estimator outperforms the classical SG-NPML in terms of convergence rate. However, the MSE floor for both SG-NPML and NG-NPML is same. Further, convergence analysis of proposed NG-NPML algorithm is also presented and derive an analytical expression for the steady-state MSE and EMSE. To further improve the MSE floor of the NG-NPML algorithm, ZA-NG-NPML is proposed in the third part.

## 2.1 Iterative-Time Domain Algorithm

In this section, the system model and detailed analysis of the proposed ITD algorithm is discussed followed by simulation results and discussions.

### 2.1.1 System Model

In typical OFDM transmission [43–45], data blocks are converted into time-domain by inverse FFT (IFFT)) after padding zeros in each block. Then each block is extended by CP in time-domain which is copy of the last samples. The CP is used to avoid inter-symbol interference (ISI) between the adjacent OFDM symbols.

For the considered OFDM system, let  $X(k_c)$  be the transmitted symbol on the  $k_c^{th}$  subcarrier. The transmitted complex baseband OFDM signal after IFFT can be expressed as:

$$x(n) = \frac{1}{N} \sum_{k=0}^{N-1} X(k_c) e^{j2\pi k_c n/N} \quad n = 0, \dots, N-1 \quad (2.1)$$

where  $N$  is the total number of subcarriers. Let the sparse CIR be expressed as:

$$\mathbf{h} = [h(0), h(1), \dots, h(L-1)]^T \quad (2.2)$$

where  $\mathbf{h}$  is a vector of dimension  $L \times 1$ , and  $L$  is the length of channel which must be less than  $L_{cp}$  ( $L_{cp}$  is the length of CP). The received complex baseband signal in time-domain is given by:

$$y(n) = \sum_{l=0}^{L-1} h(l)x(n-l) + w(n) \quad (2.3)$$

where  $w(n)$  is a AWGN and assumed to be independent and identically distributed (i.i.d.) with zero mean and variance  $\sigma_w^2$ . The time-domain transmitted signal  $x(n)$ , and the received signal  $y(n)$  are used for initial detection of active taps location.

### 2.1.2 Modified Wiener Filter

Modified Wiener filter (MWF) is modification of the conventional Wiener filter for sparse channel models. MWF gives lower bound for the proposed sparse channel estimation algorithm. According to MWF, the estimated channel coefficients are given as:

$$\hat{\mathbf{h}}_{\text{MWF}} = (\mathbf{R}_{\mathbf{x}H\mathbf{x}}^{-1})_{i,i} (\mathbf{R}_{\mathbf{y}^*\mathbf{x}})_j \quad (2.4)$$

where  $\mathbf{x}$  and  $\mathbf{y}$  are the transmitted and received vectors, respectively,  $\mathbf{R}_{\mathbf{x}H\mathbf{x}}$  is the diagonal matrix of auto-correlation of transmitted vector,  $\mathbf{R}_{\mathbf{y}^*\mathbf{x}}$  is a vector of cross-correlation between transmitted and received vector. The  $(\cdot)^H$  and  $(\cdot)^*$  represents Hermitian and conjugate of  $(\cdot)$ , respectively,  $(\cdot)_{i,i}$  and  $(\cdot)_j$  represents the element of  $(\cdot)$ , and  $i$  and  $j$  represents the active channel tap positions. The MWF helps in

quantifying performance of the proposed algorithm.

### 2.1.3 Iterative-Time Domain Algorithm

The proposed algorithm initially estimates location (index) of the active channel taps with the help of cross-correlation of transmitted preamble and received signal. This is performed as a standard procedure in most commercial receivers for frame synchronization, hence this step does not result in increase in proposed receiver's computational complexity. Next, iteratively estimate the sparse channel with the help of adaptive thresholding, and LMS algorithm. At the receiver, the received time-domain preamble  $y(n)$  without removing CP is correlated with the transmitted time-domain preamble  $x(n)$  to obtain partial sparse common support

$$z(m) = \sum_{n=1}^{L_{cp}} x^*(n)y(m+n), \quad n = 0, 1, \dots, L_{cp} - 1 \quad (2.5)$$

where  $z(m)$  represents the cross-correlation of  $x(n)$  and  $y(n)$ , and  $\mathbf{z} = [z(1), \dots, z(L_{cp})]$  represents a vector.

Due to good correlation property of the preamble, the initial detection of active channel taps location (also referred as partial common support) is represented as:

$$P = m : \hat{z}(m) \geq \gamma, \quad m = 1, 2, \dots, L_{cp} \quad (2.6)$$

where  $\hat{z}(m) = \frac{|z(m)|}{\max(|\mathbf{z}|)}$  and, threshold,  $\gamma$  [24] is given as:

$$\gamma = 3 \left( \sum_{m=1}^{L_{cp}} \hat{z}^2(m) \right)^{1/2} / L_{cp} \quad (2.7)$$

The initial detection of active channel taps location along with  $\mathbf{x}$  (transmitted signal vector of dimension  $1 \times N$ ) and  $\mathbf{y}$  (received signal vector of dimension  $1 \times N$ ) are used as an input to the LMS algorithm, and the updated channel coefficients (after convergence of LMS algorithm) are obtained as output of the LMS algorithm. The estimated output channel vector,  $\hat{\mathbf{h}}$  ( $\hat{\mathbf{h}} = [\hat{h}(0), \dots, \hat{h}(L_{cp} - 1)]$ ), is used to calculate

the threshold  $\eta$  as:

$$\eta = 0.05e^{-\tilde{h}} \quad (2.8)$$

where  $\tilde{h} = \frac{1}{L_{cp}} \sum_{n=0}^{L_{cp}-1} |\hat{h}(n)| / \max(|\hat{\mathbf{h}}|)$ . Then choose the channel coefficients whose absolute value is greater than or equal to  $\eta$ . The threshold,  $\eta$ , also selects the non-active tap positions adjacent to the active tap positions. To discard these adjacent non-active tap positions, blocks of five consecutive channel coefficients are constructed and threshold on each block on the basis of channel coefficients present in the block is applied. The threshold on each block,  $\eta_b$ , is given as:

$$\eta_b = 0.5e^{-\tilde{h}} \quad (2.9)$$

---

**Algorithm 1** Proposed Algorithm

---

**Input:**  $\hat{\mathbf{h}}$ , (after cross-correlation and LMS algorithm),  $\tilde{h}$

**Output:**  $\mathbf{h}_o$ .

```

1:  $\eta \leftarrow 0$ , iter  $\leftarrow 10$ ;
2: for k = 1 : iter
3: TAP_POS=[],  $\eta(k+1) \leftarrow 0.05\exp(-\tilde{h})$ ;
4: if  $\eta(k+1) == \eta(k)$  then
5:   break;
6: else
7:   idx  $\leftarrow \text{find}(|\hat{\mathbf{h}}| \geq \eta(k+1))$ ;
8:    $\hat{\mathbf{h}}^1 \leftarrow \text{zeros}(1, L_{cp})$ ;  $\hat{\mathbf{h}}^1(\text{idx}) \leftarrow \hat{\mathbf{h}}(\text{idx})$ 
9:   for L = 1 : 5 : idx(end)
10:     $\eta_b \leftarrow 0.5\exp(-\text{mean}(|\hat{\mathbf{h}}^1(L:L+4)|))$ ;
11:    POS  $\leftarrow \text{find}(|\hat{\mathbf{h}}^1(L:L+4)| \geq \eta_b)$ ;
12:    TAP_POS=[TAP_POS L+POS-1];
13:   end for
14:    $\hat{\mathbf{h}} = \text{LMS}(\mathbf{x}, \mathbf{y}, \hat{\mathbf{h}}(\text{TAP\_POS}))$ 
15:    $\tilde{h} = \frac{1}{L_{cp}} \sum_{n=0}^{L_{cp}-1} |\hat{h}(n)| / \max(|\hat{\mathbf{h}}|)$ 
16: end if
17: end if
18: end for
19:  $\hat{\mathbf{h}}_o \leftarrow \hat{\mathbf{h}}$ 

```

---

Then choose the channel coefficients for each block whose absolute value is greater than or equal to their corresponding  $\eta_b$ . The chosen channel coefficients are further updated by LMS algorithm, and updated channel vector (after conver-

gence of LMS algorithm) as output is obtained. Again apply (2.8), to make a new block, and repeat the process till maximum number of iterations is reached or the current threshold is equal to the previous threshold. The final estimated sparse channel vector is given by  $\hat{\mathbf{h}}_o$  in Algorithm 1. The proposed algorithm is given in Algorithm 1 ( $\hat{\mathbf{h}}^1$  is the temporary copy of  $\hat{\mathbf{h}}$ ).

Due to very low value of initial thresholding,  $\gamma$ , large number of taps are initially selected with the help of partial common support. Therefore, in each iteration,  $\eta$  must be increased so that non-active taps are rejected. This will happen if  $\tilde{h}$  decreases in each iteration. LMS algorithm provides lower value to non-active taps, and  $\eta_b$  is used to discard the adjacent taps of active tap in each block. Hence, both the LMS algorithm and block thresholding jointly reduce the number of non-active tap coefficients of  $\hat{\mathbf{h}}$  in each iteration.

#### 2.1.4 Analysis of Threshold ( $\eta$ )

Selection of threshold  $\eta$  is based on PDF of the envelope of channel coefficients. Without loss of generality the real and imaginary parts of the channel coefficients are assumed to be normally distributed with zero mean and identical variance. It is also assumed that the absolute value or envelope of the channel coefficients is Rayleigh distributed:

$$f(|\hat{h}(n)|) = \frac{|\hat{h}(n)|}{\sigma^2} e^{-|\hat{h}(n)|^2/2\sigma^2} \quad (2.10)$$

where,  $\sigma$  is the scale parameter of the distribution.

For active taps,  $|\hat{h}(n)| > 0$ , hence the thresholding  $\eta$  (for a threshold  $T_h$ ) can be calculated as:

$$\eta = \int_{T_h}^{\infty} f(|\hat{h}(n)|) d|\hat{h}(n)| = \int_{T_h}^{\infty} \frac{|\hat{h}(n)|}{\sigma^2} e^{-|\hat{h}(n)|^2/2\sigma^2} d|\hat{h}(n)| \quad (2.11)$$

After simple calculation, the thresholding can be written as:

$$\eta = e^{-T_h} \quad (2.12)$$

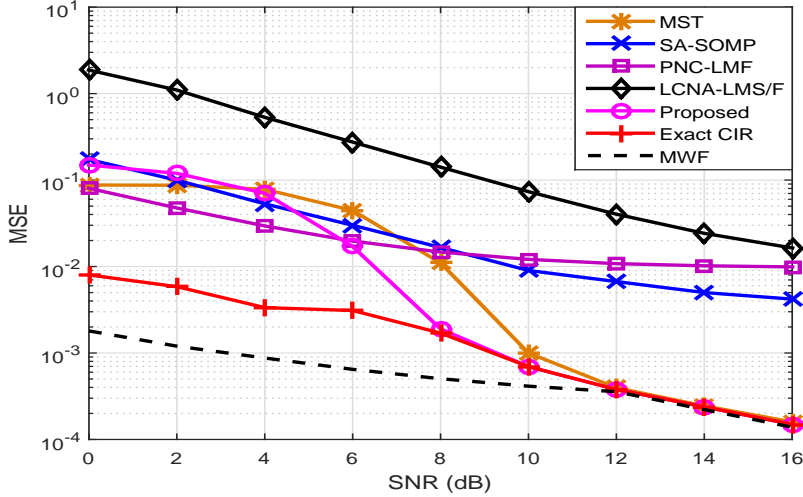


Figure 2.1: MSE vs SNR for IEEE 802.22 sparse channel estimation under SUI-6 channel model.

The proof is given in Appendix A.

### 2.1.5 Simulation Results and Discussion

In this section, the performance of proposed sparse channel estimator for IEEE 802.22 standard under various standard sparse channel model in the presence of AWGN is investigated. The simulation parameters (from the standard) are summarized as follows: the system bandwidth is 6 MHz; LTS is used as preamble of length 2048 for channel estimation, and  $L_{cp} = 512$ . The simulations are carried over an ensemble of 200-runs with step-size for LMS algorithm equal to 0.005. Three sparse channel models are considered, which are SUI-6, ITU-VB and WRAN channel model. The MSE of CIR which is given as  $(\|\mathbf{h} - \hat{\mathbf{h}}\|_2^2$  where  $\|\cdot\|_2$  is an Euclidean norm) is used as performance metric for comparison.

Fig. 2.1 shows the MSE vs SNR for IEEE 802.22 sparse channel estimation under SUI-6 channel model. Fig. 2.1 shows that the proposed algorithm performs much better than all the conventional algorithms, and the MSE of the proposed algorithm is same as exact CIR (Exact CIR means knowledge of active tap positions known *a priori* at the receiver with use of LMS algorithm) after 8 dB SNR. The MSE of MWF gives lower bound for the proposed estimator. Fig. 2.2 shows the MSE vs SNR

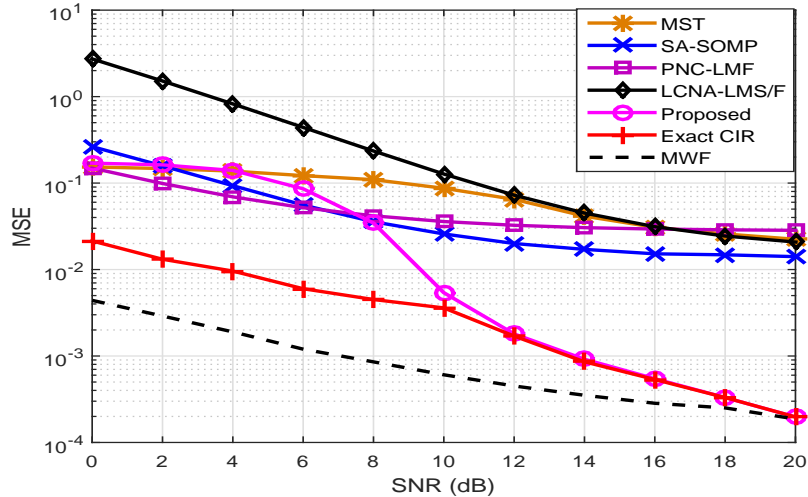


Figure 2.2: MSE vs SNR for IEEE 802.22 sparse channel estimation under ITU-VB channel model.

for IEEE 802.22 sparse channel estimation under ITU-VB channel model (with zero Doppler frequency). Fig. 2.2 again shows superiority of the proposed algorithm over conventional algorithm and the MSE of the proposed algorithm approaches exact CIR after 12 dB SNR. Fig. 2.3 shows the MSE vs SNR for IEEE 802.22 sparse channel estimation under WRAN channel model. It is observed from Fig. 2.3 that the proposed algorithm outperforms all the conventional algorithms and the MSE of the proposed algorithm is same as exact CIR after 8 dB SNR. It is observed from Fig. 2.1-2.3 that the proposed algorithm is robust to all type of channel models than conventional algorithms and approaches optimum estimator.

The computational complexity analysis of proposed and conventional algorithm in terms of multiplication is as follows: MST requires  $\mathcal{O}(\frac{N}{2}\log_2 N + L_{cp}) + \mathcal{O}(\frac{L_{cp}}{2}\log_2 L_{cp})$ , SA-SOMP requires  $\mathcal{O}(bN(2L_{cp} + P + b))$ , PNC-LMF requires  $\mathcal{O}(10NL_{cp} + 2N)$ , LCNA-LMS/F requires  $\mathcal{O}(9NL_{cp})$ , and proposed algorithm requires  $\mathcal{O}(8NP + L_{cp} + P)$  per iteration (where  $b$  [24] is compensation factor, and  $P$  is number of detected taps per iteration). For the proposed algorithm computational complexity decreases as iteration increases because  $P$  decreases as iteration increases. Hence, although the complexity of the proposed algorithm is higher than MST, SA-SOMP, PNC-LMF, and LCNA-LMS/F. The increased performance gain (i.e. working in optimal

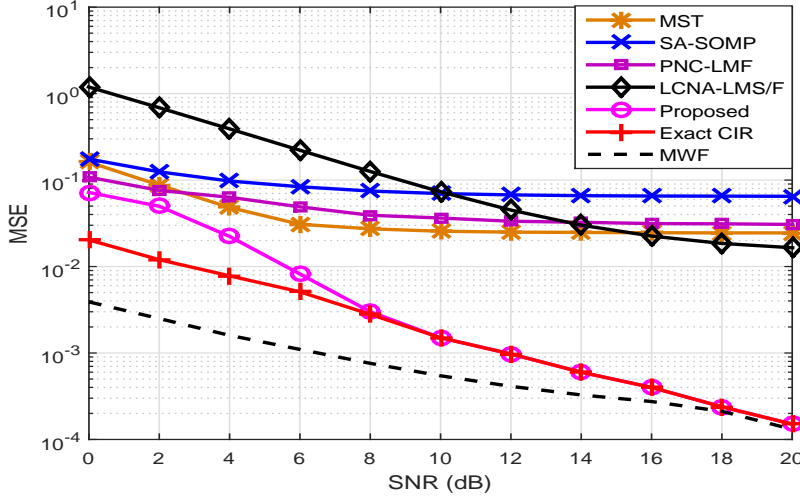


Figure 2.3: MSE vs SNR for IEEE 802.22 sparse channel estimation under WRAN channel model.

region) outweighs the increase in computational complexity. Moreover, the computational complexity of the proposed algorithm can be reduced by using fast LMS algorithm and parallel processing of blocks (Step 9 to 13 in the Algorithm 1).

## 2.2 Natural Gradient Non-Parametric Maximum Likelihood Algorithm

In this section, system model and brief overview of SG-NPML is discussed followed by the proposed NG-NPML algorithm with first and second order convergence analysis. The second order convergence is more important as it provides better analysis of algorithms and insights about working of algorithms as compared to the first order convergence analysis.

### 2.2.1 System Model and Preliminaries

In this subsection, the system model for real valued channel estimation as shown in Fig. 2.4 and overview of SG-NPML and NG adaptive algorithm are explained. Let  $x(n)$ ,  $\mathbf{x}(n) = [x(n), x(n-1), \dots, x(n-L+1)]^T$ ,  $\mathbf{h}$ ,  $w(n)$ ,  $i(n)$ ,  $\hat{\mathbf{h}}_k$ ,  $e(n)$  and  $v(n) =$

$w(n) + i(n)$  represent the source signal, vector of source signal of dimension  $L \times 1$ , true channel impulse response vector, AWGN, CCI signal, adaptive (estimated) filter coefficient vector, residual error and Gaussian mixture noise, respectively. Here  $L$ ,  $k$ , and  $n$  represent the channel length, iteration index, and time index, respectively. The joint PDF of AWGN and CCI follow the Gaussian mixture. Let the received signal be given by:

$$y(n) = \sum_{l=0}^{L-1} h(l)x(n-l) + v(n) \quad (2.13)$$

In SG-NPML technique, an iterative gradient ascent method is used for channel estimation [32]. The cost function is given by [32]

$$\mathcal{J}(\hat{\mathbf{h}}_k) = \mathcal{L}(\hat{\mathbf{h}}_k | \mathbf{y}) = \log f(\mathbf{y} | \hat{\mathbf{h}}_k) = \sum_{m=1}^M \log f(e(m)) \quad (2.14)$$

where  $\mathcal{L}(\cdot)$  represents the log likelihood function and  $f(e(m))$  is the PDF of Gaussian mixture noise which is estimated by kernel density estimation with  $M$  measured data samples.  $e(m)$  can be calculated as:

$$e(m) = y(m) - \sum_{l=0}^{L-1} \hat{h}_k(l)x(m-l) \quad (2.15)$$

PDF of the Gaussian mixture noise is estimated by (2.16):

$$\hat{f}(e(i)) = \frac{1}{M} \sum_{j=1}^M K(e(i) - e(j)) \quad i = 1, 2, \dots, M \quad (2.16)$$

where  $K(\cdot)$  is assumed to be Gaussian kernel [46] and defined as:

$$K(t) = \frac{1}{\sqrt{(2\pi\sigma_k^2)}} \exp\left(\frac{-t^2}{2\sigma_k^2}\right) \quad (2.17)$$

where  $\sigma_k$  is the kernel width [46]. The channel update equation at  $(k+1)^{th}$  iteration is given by

$$\hat{\mathbf{h}}_{k+1} = \hat{\mathbf{h}}_k + \mu \nabla_{\hat{\mathbf{h}}_k} \mathcal{J}(\hat{\mathbf{h}}_k) \quad (2.18)$$

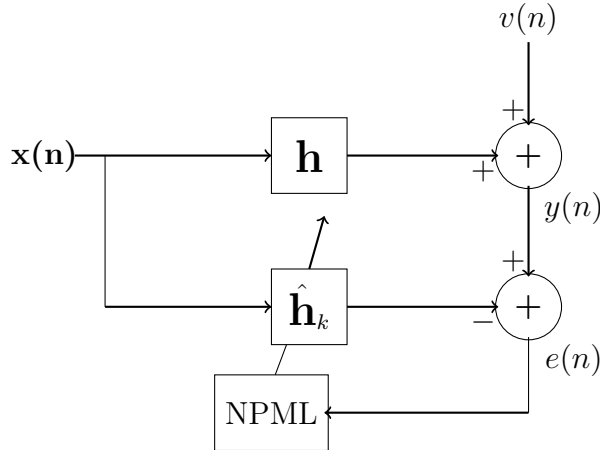


Figure 2.4: System model for channel estimator.

where  $\mu$  is the step-size and for SG-NPML, the gradient of cost function which minimize (2.14) is given by [32]

$$\begin{aligned} \nabla_{\hat{\mathbf{h}}_k} \mathcal{J}(\hat{\mathbf{h}}_k) &= \frac{1}{\sigma_k^2} \sum_{i=1}^M \frac{\sum_{j=1}^M (e(i) - e(j))(\mathbf{x}(i) - \mathbf{x}(j))K(e(i) - e(j))}{\sum_{k=1}^M K(e(i) - e(k))} \end{aligned} \quad (2.19)$$

After substituting (2.19) into (2.18), the channel update equation is given by:

$$\hat{\mathbf{h}}_{k+1} = \hat{\mathbf{h}}_k + \frac{\mu}{\sigma_k^2} \sum_{i=1}^M \left( \frac{\sum_{j=1}^M e_k \mathbf{q} K(e_k)}{\sum_{j=1}^M K(e_k)} \right) \quad (2.20)$$

where  $e_k = e(i) - e(j)$ ,  $\mathbf{q} = \mathbf{x}(i) - \mathbf{x}(j)$  of dimension  $L \times 1$ . After iterations, the above equation tends to convergence and the maximum likelihood estimate of the channel vector in additive Gaussian mixture noise is obtained [32]. However, for a large channel, the convergence is slow and is computationally more complex.

On the other hand, if the channel is sparse; an adaptation algorithm that updates the channel coefficients by taking advantage of sparseness of parameter solution space is needed. It is shown in [47], that the NG based adaptation provides a better solution for sparse channels. This is because in NG adaptation, Riemannian metric tensor provides large step-size for active tap coefficients, and small step-size for inactive tap coefficients and hence gives faster convergence. The estimator coefficients are updated based on a “non-straight line” distance metric defined by

the Riemannian metric structure. In Riemannian space, distance is not measured according to the Euclidean norm. Once the parameter space is warped, then the NG update of  $\mathbf{h}$  at  $(k + 1)^{th}$  iteration is given by [47]:

$$\hat{\mathbf{h}}_{k+1} = \hat{\mathbf{h}}_k + \mu \mathbf{G}_k^{-1} \nabla_{\hat{\mathbf{h}}_k} \mathcal{J}(\hat{\mathbf{h}}_k) \quad (2.21)$$

where  $\mathbf{G}_k$  is the Riemannian metric tensor (gain matrix) which is a positive-definite matrix that describes the local curvature of the parameter space at  $\hat{\mathbf{h}}_k$ , and  $\mathbf{G}_k^{-1}$  is the inverse of  $\mathbf{G}_k$ .

To derive the natural gradient, a distance metric (as given in [47]) is chosen, which is not Euclidean, but Riemannian:

$$\begin{aligned} D &= |d_{\hat{h}_k(l)}(\hat{h}_k(l), \hat{h}_k(l) + r_{k+1}(l))|^2 \\ &= \sum_{l=0}^{L-1} |F(\hat{h}_k(l) + r_{k+1}(l)) - F(\hat{h}_k(l))|^2 \end{aligned} \quad (2.22)$$

where the  $\mathbf{r}_{k+1}$  ( $r_{k+1}(0), r_{k+1}(1), \dots, r_{k+1}(L-1)^T$ ) is a column vector of  $L \times 1$  dimension having elements of small real value data and  $F(\cdot)$  is a warping transformation on  $(\cdot)$ . By using Taylor series approximations in the above equation, the distance metric can be written as [47]:

$$D = \mathbf{r}_{k+1}^T \mathbf{G}_k \mathbf{r}_{k+1} \quad (2.23)$$

$\mathbf{G}_k$  for the proposed NG-NPML algorithm is calculated using (2.22) and (2.23).

### 2.2.2 NG-NPML Algorithm

In this section, the proposed iterative algorithm by transforming the parameter space is derived and calculate the gain matrix. The gain matrix  $\mathbf{G}_k$  is updated at each iteration, hence it provides large step-size for active taps and small step-size for inactive taps, thereby leading to faster convergence. The gain matrix  $\mathbf{G}_k$  depends on the estimated channel coefficients at each iterations. As shown in (2.22) and (2.23),

the gain matrix  $\mathbf{G}_k$  also depends on the transformation. The transformation can include linear, quadratic, and higher orders. The transformation can be generalized to any order as given below:

$$F(\hat{h}_k(l)) = \sqrt{\alpha_k \left( \left| |\hat{h}_k(l)| - |\hat{h}_k(l)|^2 \dots - |\hat{h}_k(l)|^{p-1} - |\hat{h}_k(l)|^p \right| + \beta \right)} \quad (2.24)$$

where  $p$  is the order of transformation,  $\beta$  is a regularization parameter and  $\alpha_k$  is a normalization term which is given as:

$$\alpha_k = \frac{1}{L} \sum_{l=0}^{L-1} \left| |\hat{h}_k(l)| - |\hat{h}_k(l)|^2 \dots - |\hat{h}_k(l)|^{p-1} - |\hat{h}_k(l)|^p \right| + \beta \quad (2.25)$$

The convergence of NG-NPML can be made faster by using higher order transformation. However, the computational complexity also increases as the order of the transformation increases. Hence, to balance computational complexity and faster convergence rate, quadratic warping transformation on the channel coefficient space is considered which is given by:

$$F(\hat{h}_k(l)) = \sqrt{\alpha_k \left( \left| |\hat{h}_k(l)| - |\hat{h}_k(l)|^2 \right| + \beta \right)} \quad (2.26)$$

After substituting (2.26) in (2.22), the distance metric is given by (2.27).

$$D = \sum_{l=0}^{L-1} \left| \sqrt{\alpha_k \left( \left| |\hat{h}_k(l) + r_{k+1}(l)| - |\hat{h}_k(l) + r_{k+1}(l)|^2 \right| + \beta \right)} - \sqrt{\alpha_k \left( \left| |\hat{h}_k(l)| - |\hat{h}_k(l)|^2 \right| + \beta \right)} \right|^2 \quad (2.27)$$

Here, assume that  $|r_{k+1}(l)| \ll 1$  and  $\|\hat{\mathbf{h}}_k\| \gg \|\mathbf{r}_{k+1}\|$ . In the above equation, two cases,  $\hat{h}_k(l)r_{k+1}(l) > 0$  and  $\hat{h}_k(l)r_{k+1}(l) < 0$  are considered. For both the cases, the final channel update equation at  $(k+1)^{th}$  iteration is given as:

$$\hat{\mathbf{h}}_{k+1} = \hat{\mathbf{h}}_k + \mu \frac{\left( \left| |\hat{\mathbf{H}}_k| - |\hat{\mathbf{H}}_k|^2 \right| + \beta \mathbf{I} \right)}{\alpha_k \mathbf{\Gamma}_2} \nabla_{\hat{\mathbf{h}}_k} \mathcal{J}(\hat{\mathbf{h}}_k) \quad (2.28)$$

where  $\mathbf{\Gamma}_2$  is a matrix of dimension  $L \times L$ ,  $|\hat{\mathbf{H}}_k|$  and  $|\hat{\mathbf{H}}_k|^2$  are  $L \times L$  diagonal matrix. The proof of the above equation is given in Appendix B. Similarly, the channel update equation at  $(k+1)^{th}$  iteration for  $p^{th}$  order transformation is given by:

$$\hat{\mathbf{h}}_{k+1} \approx \hat{\mathbf{h}}_k + \mu \frac{\left( \left| |\hat{\mathbf{H}}_k| - \dots - |\hat{\mathbf{H}}_k|^p \right| + \beta \mathbf{I} \right)}{\alpha_k \mathbf{\Gamma}_p} \nabla_{\hat{\mathbf{h}}_k} \mathcal{J}(\hat{\mathbf{h}}_k) \quad (2.29)$$

where  $\mathbf{\Gamma}_p = (\mathbf{I} + 2|\hat{\mathbf{H}}_k| + \dots + p|\hat{\mathbf{H}}_k|^{p-1})^2$ . After substituting (2.19) into (2.28), the channel update equation at  $(k+1)^{th}$  iteration for quadratic transformation can be written as:

$$\hat{\mathbf{h}}_{k+1} = \hat{\mathbf{h}}_k + \frac{\tilde{\mu}}{\sigma_k^2} \sum_{i=1}^M \frac{\sum_{j=1}^M e_k \mathbf{G}_k \mathbf{q} K(e_k)}{\sum_{j=1}^M K(e_k)} \quad (2.30)$$

where  $\mathbf{G}_k = \left( \left| |\hat{\mathbf{H}}_k| - |\hat{\mathbf{H}}_k|^2 \right| + \beta \mathbf{I} \right) / (\alpha_k \mathbf{\Gamma}_2)$  is a diagonal gain matrix with  $g_k(l) = \mathbf{G}_k(l, l)$  and satisfying  $\sum_{l=0}^{L-1} g_k(l) = 1$  ( $0 < g_k(l) < 1$ ).

### 2.2.3 Convergence Analysis of NG-NPML

In this subsection, convergence analysis of NG-NPML algorithm is described. The convergence analysis of NG-NPML algorithm is not straightforward as used in the least mean square algorithm because of the presence of  $\mathbf{G}_k$  and  $K(e_k)$ . In order to analyze convergence of the proposed algorithm in the presence of  $\mathbf{G}_k$ , ‘transform’ domain model of PNLMS algorithm [48] is used. Further, since  $K(e_k)$  consists of exponential term, it is approximated by its Taylor series expansion for mathematical tractability. Let  $\mathbf{R}_{\tilde{\mathbf{q}},k} = \mathbb{E}[\tilde{\mathbf{q}}_k \tilde{\mathbf{q}}_k^T]$  and  $\mathbf{R}_{\mathbf{q}} = \mathbb{E}[\mathbf{q} \mathbf{q}^T]$  is the correlation matrix (diagonal) of transformed input  $\tilde{\mathbf{q}}_k$  and  $\mathbf{q}$ , respectively of dimension  $L \times L$ .

#### Transform Domain Model of the NG-NPML Algorithm

The transform domain model of the NG-NPML algorithm is shown in Fig. 2.5, where  $\mathbf{G}_k^{1/2}$  is a transform domain diagonal matrix of dimension  $L \times L$ ,  $\mathbf{s}(n)$  and  $\check{\mathbf{h}}_k = [\check{h}_k(0), \check{h}_k(1), \dots, \check{h}_k(L-1)]^T$  are the transformed input and filter coefficient vector, respectively with  $\mathbf{s}(n) = \mathbf{G}_k^{1/2} \mathbf{x}(n)$  and  $\check{\mathbf{h}}_k = \mathbf{G}_k^{-1/2} \hat{\mathbf{h}}_k$ , such that  $\check{\mathbf{h}}_k^T \mathbf{s}(n) =$

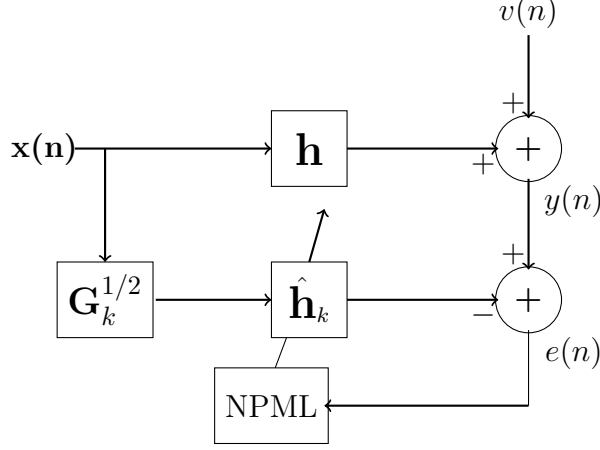


Figure 2.5: Transform domain model of NG-NPML estimator.

$\hat{\mathbf{h}}_k^T \mathbf{x}(n)$ . The update equation of  $\check{\mathbf{h}}$  at  $(k+1)^{th}$  iteration is given according to the SG-NPML:

$$\check{\mathbf{h}}'_{k+1} = \check{\mathbf{h}}_k + \frac{\mu}{\sigma_k^2} \sum_{i=1}^M \frac{\sum_{j=1}^M e_k \tilde{\mathbf{q}}_k K(e_k)}{\sum_{j=1}^M K(e_k)} \quad (2.31)$$

where,  $\tilde{\mathbf{q}}_k = \mathbf{s}(i) - \mathbf{s}(j)$  of dimension  $L \times 1$ . From (2.30), the  $\hat{\mathbf{h}}_{k+1}$  can be computed as  $\hat{\mathbf{h}}_{k+1} = \mathbf{G}_k^{1/2} \check{\mathbf{h}}'_{k+1}$ . Now,  $\check{\mathbf{h}}_{k+1} = \mathbf{G}_{k+1}^{-1/2} \hat{\mathbf{h}}_{k+1}$  which can be written as  $\check{\mathbf{h}}_{k+1} = \mathbf{G}_{k+1}^{1/2} \mathbf{G}_k^{1/2} \check{\mathbf{h}}'_{k+1}$ . It is reasonable to assume  $\mathbf{G}_{k+1}^{1/2} \approx \mathbf{G}_k^{1/2}$  near convergence and/or large order channel [48] and this implies  $\check{\mathbf{h}}'_{k+1} = \check{\mathbf{h}}_{k+1}$ . Hence, (2.31) can be written as:

$$\check{\mathbf{h}}_{k+1} = \check{\mathbf{h}}_k + \frac{\mu}{\sigma_k^2} \sum_{i=1}^M \frac{\sum_{j=1}^M e_k \tilde{\mathbf{q}}_k K(e_k)}{\sum_{j=1}^M K(e_k)} \quad (2.32)$$

It is also assumed that the  $\tilde{\mathbf{q}}_k$  is zero mean Gaussian random variable for large order channel by the central limit theorem [49]. The above equation is used for the convergence analysis of the proposed algorithm in terms of mean weight error.

### Mean Weight Error Convergence Analysis

With a zero-mean Gaussian transformed input  $\tilde{\mathbf{q}}_k$  and its correlation matrix  $\mathbf{R}_{\mathbf{q},k}$ , the proposed algorithm produces stable performance with respect to mean weight error if the step-size  $\mu$  satisfies the below criterion:

$$0 < \mu < \frac{2\sigma_k^2}{M\lambda_{\mathbf{q},k}^{max}} \quad (2.33)$$

where  $\lambda_{\mathbf{q},k}^{max}$  is the maximum eigenvalue of  $\mathbf{R}_{\mathbf{q},k}$ . The proof of the above equation is given in Appendix C.

### Steady-State Mean Square Error Performance Analysis

In this subsection, the analytical expression for the steady-state MSE based on Taylor series expansion is derived and show that to achieve lower MSE floor, step-size must be small. With a zero-mean Gaussian transformed input  $\tilde{\mathbf{q}}_k$ , correlation matrix  $\mathbf{R}_{\mathbf{q},k}$  and using the Taylor series expansion of the exponential function, the steady-state MSE is given by:

$$\xi_\infty = \xi_0 + \lim_{k \rightarrow \infty} \frac{\mu M \text{Tr}(\mathbf{R}_{\mathbf{q},k}) \mathbb{E}[\exp\left(\frac{-\tilde{v}^2}{\sigma_k^2}\right) \tilde{v}^2] \mathbb{E}[\exp\left(\frac{-\tilde{v}^2}{2\sigma_k^2}\right)]}{2\sigma_k^2 \mathbb{E}[\exp\left(\frac{-\tilde{v}^2}{2\sigma_k^2}\right) \left(1 - \frac{\tilde{v}^2}{\sigma_k^2}\right)] \mathbb{E}[\exp\left(\frac{-\tilde{v}^2}{\sigma_k^2}\right)]} \quad (2.34)$$

where,  $\xi_0 = \mathbb{E}[\tilde{v}^2]$  is the minimum MSE (MMSE),  $\tilde{v} = v(i) - v(j)$ ,  $\xi_\infty = \mathbb{E}[e_k^2]$  at steady-state, and  $\text{Tr}(\cdot)$  is the trace of  $(\cdot)$ . The proof of the above equation is given in Appendix D. With the help of above equation, observations can be derived as corollary

- **Corollary 1**

The steady-state MSE of the proposed NG-NPML algorithm is independent of the gain matrix which is given as:

$$\xi_\infty = \xi_0 + \frac{\mu M \sigma_{\mathbf{q}}^2 \mathbb{E}[\exp\left(\frac{-\tilde{v}^2}{\sigma_k^2}\right) \tilde{v}^2] \mathbb{E}[\exp\left(\frac{-\tilde{v}^2}{2\sigma_k^2}\right)]}{2\sigma_k^2 \mathbb{E}[\exp\left(\frac{-\tilde{v}^2}{2\sigma_k^2}\right) \left(1 - \frac{\tilde{v}^2}{\sigma_k^2}\right)] \mathbb{E}[\exp\left(\frac{-\tilde{v}^2}{\sigma_k^2}\right)]} \quad (2.35)$$

where  $\sigma_{\mathbf{q}}^2$  is the variance of  $\mathbf{q}$ .

*Proof.* Since,  $\tilde{\mathbf{q}}_k = \mathbf{G}_k^{1/2} \mathbf{q}$ ,  $\mathbf{R}_{\mathbf{q},k} = \mathbb{E}[\tilde{\mathbf{q}}_k \tilde{\mathbf{q}}_k^T]$  which is equal to  $\mathbb{E}[\mathbf{G}_k^{1/2} \mathbf{q} \mathbf{q}^T \mathbf{G}_k^{1/2}]$ , the gain matrix  $\mathbf{G}_k$  satisfy  $\sum_{l=0}^{L-1} g_k(l) = 1$  and at steady-state the variation of gain matrix is very small. Hence, at steady-state  $\text{Tr}(\mathbf{R}_{\mathbf{q},k}) = \text{Tr}(\mathbb{E}[\mathbf{G}_k^{1/2} \mathbf{R}_{\mathbf{q}} \mathbf{G}_k^{1/2}]) = \sigma_{\mathbf{q}}^2$  and by using above condition in (2.34) leads to (2.35).  $\blacksquare$

**Remark 1.** *The steady-state EMSE which is the second term on right hand side*

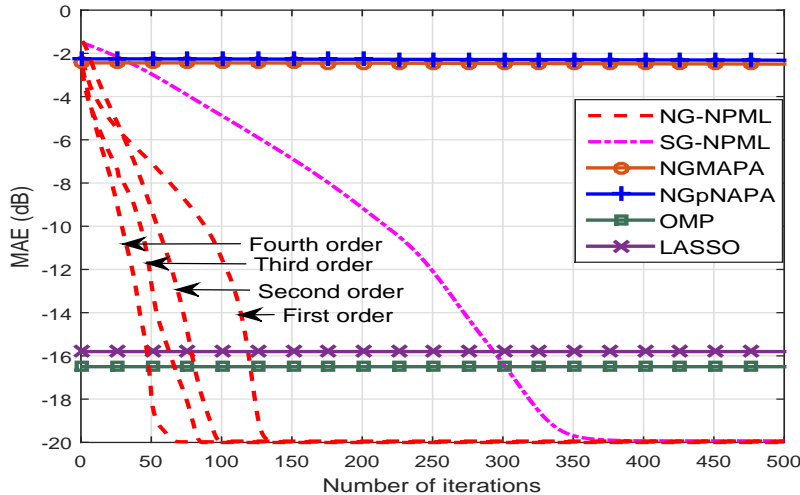


Figure 2.6: MAE of sparse channel estimation at SIR 5dB and SNR 30dB.

of (2.35) does not depend on the gain matrix. Hence both the MSE and EMSE at steady-state does not depend on the transformation  $F(\cdot)$ .

## 2.2.4 Simulation Results and Discussion

In this subsection, effectiveness of the proposed algorithm and its convergence analysis is validated by numerical simulation and experimental results. The performance of conventional SG-NPML algorithm, and the proposed NG-NPML algorithm on IEEE 802.22 based transceiver are compared. The Gaussian mixture noise considered in this paper, is due to the presence of unknown (at receiver) CCI and AWGN. For simulation, only one strong co-channel interferer is assumed.  $M = 2560$  (large) samples for better PDF estimation of Gaussian mixture noise and COST-207 TU channel model [20] are considered. The channel coefficients are Rayleigh faded. For both the algorithms, the adaptation step-size,  $\mu$ , was taken to be  $5 \times 10^{-6}$ ,  $\beta = 0.01$ , and all the simulation results were obtained by taking an ensemble of 250 runs. It is assumed that knowledge of the position of non-zero coefficient are known. However, there are various techniques to identify the position of active taps coefficients [50].

Fig. 2.6 shows the convergence curve for SG-NPML and NG-NPML (with different order of transformation) which shows the mean absolute error (MAE) of sparse channel estimation ( $10 \log_{10}(\mathbb{E}[\frac{1}{L_a} \sum_{l=0}^{L-1} |h(l) - \hat{h}(l)|])$ ), where  $L_a$  is the number of

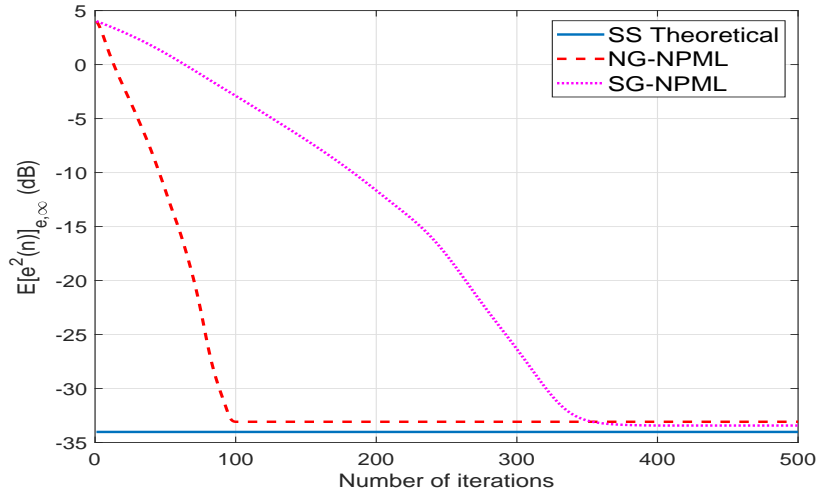


Figure 2.7: Theoretical and Monte Carlo simulation of EMSE of residual error for SG-NPML and NG-NPML at SIR 5dB and SNR 30dB.

active taps) against number of iterations at 5 dB SIR and 30 dB SNR. Fig. 2.6 shows that the proposed NG-NPML converges much faster than SG-NPML for the same MSE floor and requires about  $1/4^{th}$  iterations as compared to SG-NPML for convergence, thereby resulting in huge savings in both computations and time. Fig. 2.6 also shows that the proposed NG-NPML algorithm converges much faster as the order of transformation increases, however the complexity is also increased with the increase in the order of transformation. In Fig. 2.6, the proposed algorithm with other popular algorithms namely NG-based M-estimate affine projection algorithm (NGMAPA), NG-based p-norm affine projection algorithm (NGpNAPA), LASSO, and OMP are also compared which shows that the proposed algorithm outperforms all existing techniques for sparse channel estimation. Fig. 2.6 also shows that the performance of NGMAPA, NGpNAPA, LASSO, and OMP degrade under additive CCI and AWGN (Gaussian mixture noise).

Fig. 2.7 shows good agreement between the theoretical expression of steady-state EMSE ( $\mathbb{E}[e^2(n)]_{e,\infty}$ ) calculated in (D.19) and Monte Carlo simulation of the proposed algorithm, for comparison, the Monte Carlo simulation of the SG-NPML algorithm is also shown. In Fig. 2.7, the legend ‘SS Theoretical’ represents the theoretical steady-state of EMSE. A small deviation is attributed to the approximate

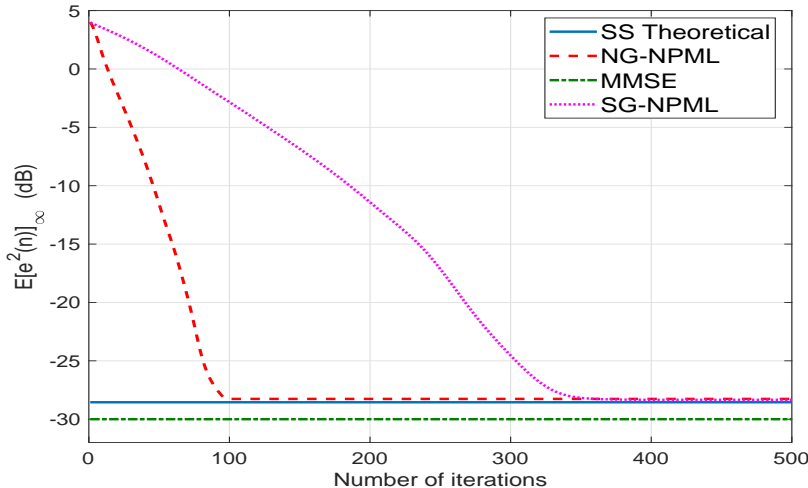


Figure 2.8: Theoretical and Monte Carlo simulation of MSE of residual error for SG-NPML and NG-NPML at SIR 5dB and SNR 30dB.

expression of (D.19). The steady-state EMSE for both the algorithm is same because the proposed algorithm is independent of the gain matrix at steady-state as given in **Corollary 1**. Fig. 2.8 shows good agreement between the theoretical expression of steady-state MSE ( $\mathbb{E}[e^2(n)]_\infty$ ) calculated in (D.21) and Monte Carlo simulation of proposed algorithm. Again for comparison, the Monte Carlo simulation of the SG-NPML algorithm is also shown. In Fig. 2.8, the legend ‘SS Theoretical’ represents the theoretical steady-state of MSE. MMSE ( $\xi_0$ ) = -30 dB (which is equivalent to the variance of AWGN) is chosen since the NPML based algorithms mitigate the effect of additive interference.

The computational complexity per iteration for both SG-NPML and NG-NPML is same as both require  $O(M^2L)$  multiplications,  $O(M^2L)$  additions and  $O(M)$  division. It is observed from Fig. 2.6 that in terms of total computational complexity NG-NPML is 3-5 times faster than SG-NPML. The computational complexity of NG-NPML is slightly high as compared to OMP ( $O(ML)$ ) and LASSO ( $O(L^3)$ ), and high as compared to NGMAPA ( $O(M)$ ) and NGpNAPA ( $O(L)$ ) per iteration. However, the improvement in MSE/BER is substantial by using proposed NG-NPML algorithm. Additionally, the complexity of PDF estimation in NG-NPML can be reduced by using fast or reduced density estimation techniques.

## 2.3 Zero-Attractor Natural Gradient Non-Parametric Maximum Likelihood Algorithm

In this section, detailed analysis of the proposed ZA-NG-NPML algorithm with first and second order convergence analysis is discussed followed by discussion.

### 2.3.1 ZA-NG-NPML Algorithm

It is observed from Fig 2.6 that both SG-NPML and NG-NPML have same MSE floor. In order to further improve performance of sparse channel estimation, the ZA concept to the NG-NPML algorithm is extended. In the proposed ZA-NG-NPML algorithm, once the faster convergence of NG-NPML algorithm is achieved, ZA is used in order to restrict the weights of inactive taps to zero by introducing  $l_1$  norm penalty into the cost function of NG-NPML. The cost function of the ZA-NG-NPML is given below:

$$J_k = \mathbf{G}_k \mathcal{J}(\hat{\mathbf{h}}_k) - \rho \|\hat{\mathbf{h}}_k\|_1 \quad (2.36)$$

where  $\rho$  ( $0 < \rho < 1$ ) is a constant and  $\|\cdot\|_1$  denotes  $l_1$  norm given as:

$$\|\hat{\mathbf{h}}_k\|_1 = \sum_{l=0}^{L-1} |\hat{\mathbf{h}}_k(l)| \quad (2.37)$$

However,  $\rho$  must be very small for shrinkage of coefficients of inactive taps. The second term of right hand side in (2.36) is known as ZA which restricts the inactive tap coefficients to nearly zero and hence leads to lower MSE [51]. The channel update equation at  $(k+1)^{th}$  iteration for the proposed ZA-NG-NPML is given as:

$$\hat{\mathbf{h}}_{k+1} = \hat{\mathbf{h}}_k + \nabla_{\hat{\mathbf{h}}_k} (J_k) \quad (2.38)$$

By taking sub-gradient of the cost function of (2.36), the above equation can be written as:

$$\hat{\mathbf{h}}_{k+1} = \hat{\mathbf{h}}_k - \rho \nabla_{\hat{\mathbf{h}}_k} (\|\hat{\mathbf{h}}_k\|_1) + \frac{\mu}{\sigma_k^2} \sum_{i=1}^M \frac{\sum_{j=1}^M e_k \mathbf{G}_k \mathbf{q} K(e_k)}{\sum_{k=1}^M K(e_k)} \quad (2.39)$$

where

$$\nabla_{\hat{\mathbf{h}}_k} (\|\hat{\mathbf{h}}_k\|_1) = \begin{cases} \text{sgn}(\hat{\mathbf{h}}_k), & |\hat{\mathbf{h}}_k| > 0 \\ 1, & \hat{\mathbf{h}}_k = 0, T > 0 \\ -1, & \hat{\mathbf{h}}_k = 0, T < 0 \\ 0, & \hat{\mathbf{h}}_k = 0, T = 0 \end{cases} \quad (2.40)$$

$T$  is the third term of (2.39).

### 2.3.2 Convergence Analysis of ZA-NG-NPML

In this subsection, convergence analysis of proposed ZA-NG-NPML algorithm is described. Because of the presence of  $\mathbf{G}_k$  and  $K(e_k)$ , the convergence analysis of ZA-NG-NPML algorithm is based on ‘transform’ domain model. The transform domain model is shown in Fig. 2.5.

#### Mean Weight Error Convergence Analysis

With a zero-mean Gaussian transformed input  $\tilde{\mathbf{q}}_k$  and its correlation matrix  $\mathbf{R}_{\mathbf{q},k}$ , the proposed algorithm produces stable performance with respect to mean weight error if the step-size  $\mu$  satisfies the below criterion:

$$0 < \mu < \frac{2\sigma_k^2}{M\lambda_{\mathbf{q},k}^{max}} \quad (2.41)$$

The proof of the above equation is given in Appendix E.

### 2.3.3 Simulation Results and Discussion

In this subsection, the performance of proposed ZA-NG-NPML algorithm for sparse channel estimation at IEEE 802.22 standard based receiver under various standard sparse channel model in the presence of impulsive noise and CCI from another IEEE

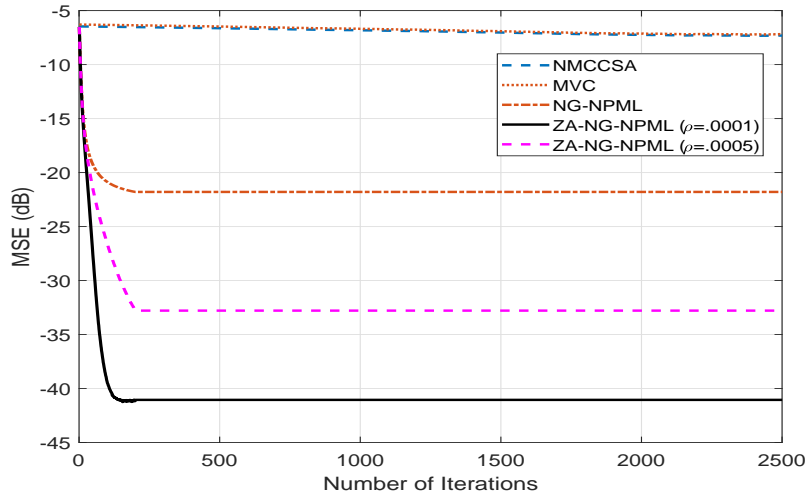


Figure 2.9: MSE (dB) vs number of iterations under SUI-6 channel model in the presence of impulsive noise as an interferer.

8022.22 transmitter investigated. Impulsive noise (SaS) is generated with  $\alpha = 1$  and  $\gamma = 0.1$ . The simulations are carried over an ensemble of 500-runs with step-size for ZA-NG-NPML algorithm equal to  $5 \times 10^{-6}$ , and  $\rho = 0.0001$  and  $0.0005$  at SNR = 30 dB and SIR = 10 dB. SUI-6 and WRAN channel model are considered as sparse channel model. In the legend of all simulation results “NMCCSA” represents sparsity aware NMCC. The MSE of the channel impulse response is given as:

$$\text{MSE}(\text{dB}) = 10\log_{10}(\|\mathbf{h} - \hat{\mathbf{h}}\|_2^2) \quad (2.42)$$

is used as performance metric for comparison.

Fig. 2.9 shows the MSE (dB) vs number of iterations under SUI-6 channel model in the presence of impulsive noise as an interferer. It is observed from Fig. 2.9 that the ZA-NG-NPML provides significant 10 dB and 20 dB gain as compared to NG-NPML for  $\rho = 0.0005$  and  $0.0001$ , respectively. Fig. 2.10 shows the MSE (dB) vs number of iterations under SUI-6 channel model in the presence of IEEE 802.22 as an interferer. It is observed from Fig. 2.10 that the ZA-NG-NPML provides 5 dB and 11 dB gain as compared to NG-NPML for  $\rho = 0.0005$  and  $0.0001$ , respectively. Fig. 2.11 shows the MSE (dB) vs number of iterations under WRAN channel model in the presence of impulsive noise as an interferer. It is observed from Fig. 2.11

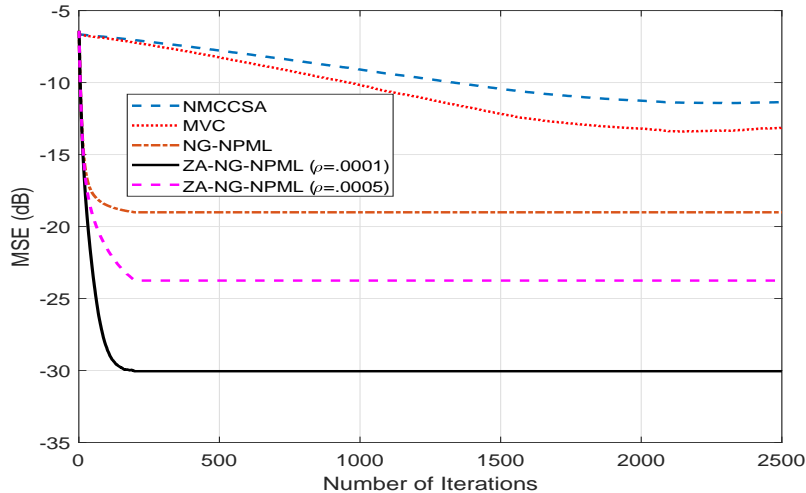


Figure 2.10: MSE (dB) vs number of iterations under SUI-6 channel model in the presence of IEEE 802.22 as an interferer.

that the ZA-NG-NPML provides 5 dB and 20 dB gain as compared to NG-NPML for  $\rho = 0.0005$  and  $0.0001$ , respectively. Fig. 2.12 shows the MSE (dB) vs number of iterations under WRAN channel model in the presence of IEEE 802.22 as an interferer. It is observed from Fig. 2.12 that the ZA-NG-NPML provides 4 dB and 13 dB gain as compared to NG-NPML for  $\rho = 0.0005$  and  $0.0001$ , respectively.

From simulations, it is observed that the NG-NPML channel estimator performs better as compared to MVC and sparsity aware NMCC, and the proposed ZA-NG-NPML outperforms the NG-NPML algorithm. Hence, ZA-NG-NPML provides significant gain in terms of channel estimation as compared to all other considered techniques. However, the performance of ZA-NG-NPML degrades as the number of active taps increases. In terms of computational complexity, MVC requires  $\mathcal{O}(L)$ , sparsity aware NMCC requires  $\mathcal{O}(L)$ , NG-NPML requires  $\mathcal{O}(M^2L)$ , and ZA-NG-NPML requires  $\mathcal{O}(M^2L+L)$  multiplications at each iteration. It is observed that the computational complexity of ZA-NG-NPML is much high as compared to MVC and sparsity aware NMCC because of calculation of PDF of  $e$  at each iteration. However, the performance gain of ZA-NG-NPML is very high as compared to MVC and sparsity aware NMCC. Additionally, the computational complexity of ZA-NG-NPML is nearly the same as NG-NPML per iteration with improved MSE performance.

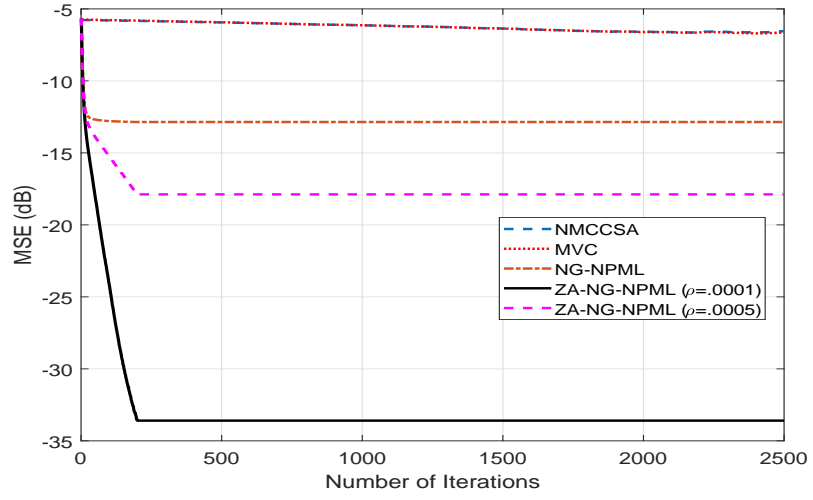


Figure 2.11: MSE (dB) vs number of iterations under WRAN channel model in the presence of impulsive noise as an interferer.

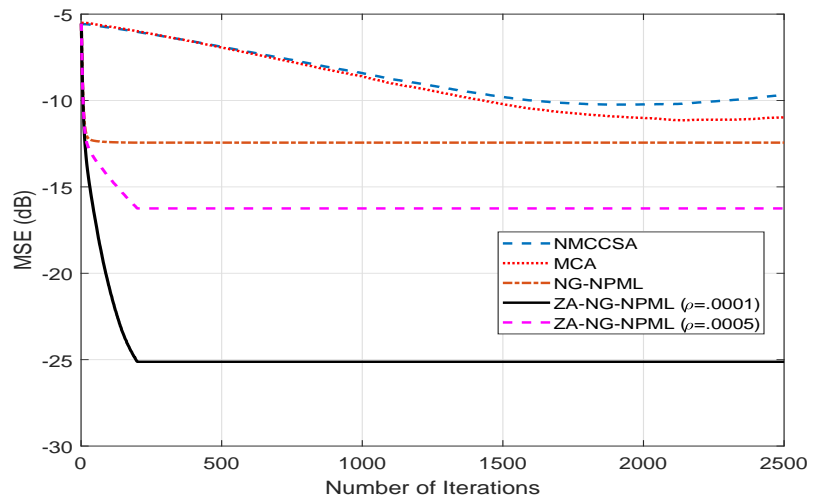


Figure 2.12: MSE (dB) vs number of iterations under WRAN channel model in the presence of IEEE 802.22 as an interferer.

## 2.4 Summary

In this chapter, an ITD algorithm is proposed to improve sparse channel estimation in the presence of Gaussian noise. The proposed ITD algorithm has better MSE performance than conventional (MST, SA-SOMP, PNCLMF, LCNA-LMS/F) sparse channel estimation algorithms. Simulations demonstrate robustness of the proposed ITD algorithm for different sparse exponentially and non-exponentially decaying standardized channel models. The proposed ITD estimator approaches the MWF solution at high SNR and can be applied to other standards. Further, NG-NPML algorithm for sparse channel estimation in the interference limited environments is proposed. Quadratic warping transformation to balance the computational complexity of transformation and faster convergence rate is used. The proposed algorithm is found to be robust to CCI as compared with other algorithms. The proposed algorithm is applied on IEEE 802.22 based transceiver and the simulation results show that the proposed NG-NPML algorithm has much faster convergence compared to conventional SG-NPML in high interference. The stability condition of proposed algorithm in terms of mean weight error and the approximated analytical expression of steady state MSE and EMSE is also derived. In order to further improve the MSE floor, ZA-NG-NPML is proposed.

## Chapter 3

# Spectrum Sensing in Cognitive Radio

RF spectrum is a scarce natural resource allocated to the licensed primary users PUs in a cognitive radio (CR) communication system. With the rapid growth in wireless services, demand on the RF spectrum is extremely high. Thus, CR based communication systems are proposed to enable efficient utilization of available spectrum by using dynamic spectrum allocation [52]. In CR based dynamic spectrum access, the secondary user (SU)s can utilize the spectrum opportunistically without interfering with the PUs using three approaches: underlay, overlay, and interweave techniques [52]. In fact, the IEEE 802.22 WRAN is the first wireless standard to include interweave CR in its specification [11] where PUs are DTV and wireless microphone (WM), and SUs are CPEs. One of the main challenges in CR based communication system is to find vacant spectrum for data transmission. Vacant spectrum can be found by using SS, a geolocation database, or a beacon signal [53]. In SS, each SU should be able to sense PU's signal accurately in low SNR to avoid interference. SS techniques can be categorized into blind and non-blind techniques. In blind techniques, such as eigenvalue based SS, a priori knowledge of PU's signal characteristics is not needed [54]. Whereas, in the non-blind techniques, such as cyclostationary based SS, SUs have to know some of the PU's signal features [55].

In general, the SS can be cast as a binary hypothesis signal detection problem. A good SS algorithm must provide high detection probability ( $P_d$ ) for low false alarm probability ( $P_f$ ) and under a low SNR regime. However for low SNR, the difference between the two hypothesis (null hypothesis  $\mathcal{H}_0$  under noise and alternative hypothesis  $\mathcal{H}_1$  under PU's signal) is, by any measure, very small and hence poses challenges for SS [56]. Most SS algorithms used in CR, are based on statistical covariance and eigenvalue of the received sample covariance matrix (RSCM). Covariance absolute value (CAV) [57] algorithm depends on the RSCM, whereas eigenvalue based detection algorithms like scaled largest eigenvalue (SLE) are based on the scaled largest eigenvalue of the RSCM [58], maximum eigenvalue (ME) [59] are based on the largest eigenvalue of RSCM, and principal component analysis (PCA) [60] depends on the summation of  $r$  largest eigenvalue of the RSCM, which also gives the maximum energy of the received signal. There are other eigenvalue based algorithms which are insensitive to noise variance such as maximum-minimum eigenvalue (MME) detection [61] which depends on the ratio of maximum eigenvalue to minimum eigenvalue of the RSCM, and energy with minimum eigenvalue (EME) [61] based on the energy of the received samples to the minimum eigenvalue of RSCM. Another class of algorithms based on feature template matching (FTM) [62] is based on the leading eigenvector of RSCM and transmitted sample covariance matrix, while the function of matrix based detection (FMD) [63] is based on the trace of the RSCM. There is another class of algorithm based on energy is three-event energy detector (3EED) [64] in which the signal detection is based on the energy of the received signal at three slots (current, previous and next). Hence, all the above detection methods except FTM do not require features of transmitted signal *a priori*. Additionally, all the considered detection methods except 3EED are based on the covariance matrix (which is also symmetric positive definite (SPD) matrix) of uncorrelated samples. Thus, the above algorithms are unsuitable for correlated or colored noise as found in many practical systems [65]. There are few algorithms such as standard-condition-number (SCN) [65], and maximum eigenvalue detection (MECN) [66] used for SS

in the presence of colored noise. However, the performance of SCN and MECN degrades at low SNR of PU and thus increases the probability of misdetection which leads to interference to the PU.

Moreover, in a wireless communication channel noise uncertainty, shadowing, and multi-path fading degrades the performance of SS. When the PU's SNR is below the receiver's SNR wall, reliable spectrum detection is impossible even with a large sensing time. If SUs are unable to detect PU's transmission, while the primary receiver is within the SUs transmission range, a hidden PU problem occurs, which leads to interference to the PU's. To circumvent the noise uncertainty, shadowing, and multi-path fading, cooperative SS (CSS) has been proposed in [67]. CSS exploits the independent fading channels and multiuser diversity. It improves the reliability of spectrum detection, increases the detection probability to protect a PU's transmitted signal, and increases the utilization of the unused spectrum by reducing the false alarm rate. In CSS, data fusion and final decision making can be performed either in centralized or decentralized mode. In the centralized mode, there is a fusion center or central controller which coordinates the cooperation among SUs and generate overall sensing information [68]. In the decentralized mode, since the central controller does not exist, SUs exchange their local sensing results and make the final decision by themselves in the second and third phase [69]. Most CSS is performed in the centralized mode [68].

This chapter has been organized in two parts: In the first part, Grassmann manifold based SS is proposed in the presence of AWGN. The proposed algorithm in detail is analyzed and also validated for robustness of the proposed algorithm with simulation and experimental results. In the second part, LogDet covariance based is proposed in the presence of colored Gaussian noise. The proposed algorithms work extremely well at low SNR in the presence of both white and colored noise. Simulation results show robustness of the proposed algorithms over existing algorithms on the captured DTV signal.

### 3.1 System Model

Let  $y(t)$  be the continuous-time signal received by a secondary user, which is sampled at Nyquist rate  $1/T_s$ . The discrete time received sample is represented as  $y(n) = y(nT_s)$ . In order to detect the PU's signal, the binary hypothesis detection model [52] can be cast as:

$$\begin{aligned}\mathcal{H}_0 : y(n) &= w(n) \\ \mathcal{H}_1 : y(n) &= x(n) + w(n)\end{aligned}\tag{3.1}$$

where,  $x(n)$  and  $w(n)$  are PU's signal samples and noise samples, respectively. However, the PU's signal which is the captured DTV signal is correlated because of filters, amplifiers, and due to oversampling [57]. In the considered two hypotheses model, PU's signal is absent in  $\mathcal{H}_0$ , and present in  $\mathcal{H}_1$ .

It is assumed that the SS is based on the statistic of each sensing segment consisting of  $N_s$  samples. Each sensing segment is further divided into  $M_s$  sub-segments, which consists of  $L_s$  (smoothing factor) consecutive samples. Thus, the sample covariance matrix of the received signal in each sensing segment can be calculated as:

$$\mathbf{R}_{yy} = \frac{1}{M_s} \sum_{i=1}^{M_s} \mathbf{y}(i)\mathbf{y}^T(i)\tag{3.2}$$

where  $\mathbf{y}(i)$  is of  $L_s \times 1$  dimension and  $(.)^T$  is transpose of  $(.)$ .

Similarly, the covariance matrix of the PU's samples in each sensing segment can be represented as:

$$\mathbf{R}_{xx} = \frac{1}{M_s} \sum_{i=1}^{M_s} \mathbf{x}(i)\mathbf{x}^T(i)\tag{3.3}$$

and the covariance matrix of noise sample is given as:

$$\mathbf{R}_{ww} = \frac{1}{M_s} \sum_{i=1}^{M_s} \mathbf{w}(i)\mathbf{w}^T(i)\tag{3.4}$$

where  $\mathbf{x}(i)$  and  $\mathbf{w}(i)$  are of  $L_s \times 1$  dimension.

Two probabilities of interest to evaluate the detection performance are:  $P_d = P(\mathcal{H}_1|y(n) = x(n) + w(n))$ , and  $P_f = P(\mathcal{H}_1|y(n) = w(n))$ . In cognitive radio,  $P_f$  relates to the spectral utilization, and  $P_d$  relates to the interference to the PU [56].

For accurate detection of PU's signal, simultaneous sensing at multiple location is performed in [70]. The sensing performance of  $N_c$ -cooperative sensors is given as in [71] :

$$Q_{md} = (P_{md})^{N_c} \quad \text{and} \quad Q_f = 1 - (1 - P_f)^{N_c} \quad (3.5)$$

where  $P_{md}$  and  $Q_{md}$  are the probability of misdetection for local SS (LSS) ( $N_c = 1$ ) and the probability of misdetection for CSS, respectively, whereas  $Q_f$  is the false alarm probability for CSS.

## 3.2 Grassmann Manifold based Spectrum Sensing

In this section, brief overview of Grassmann manifold is discussed followed by the proposed test statistics for SS algorithm. The distribution of new test statistic under null hypothesis and alternative hypothesis is derived. Lower bound for the probability of detection of signal is also derived using separating function and distribution of new test statistic. Additionally, the proposed method for the CSS is extended and derive the distribution under both hypotheses. Experimental verification on the software defined radio is also performed and it is found that the proposed method fulfills the requirement of maximum protection of the DTV signal. This section briefly reviews the Grassmann manifold with calculation of principal angles, and the corresponding Grassmann metric.

### 3.2.1 Grassmann Manifold

The Grassmann manifold  $\mathcal{G}(p, D)$  is the set of  $p$ -dimensional linear subspace of the  $\mathbb{R}^D$ . The  $\mathcal{G}(p, D)$  is a dimension of  $p \times (D - p)$  compact Riemannian manifold. An element of  $\mathcal{G}(p, D)$  can be represented by an orthonormal matrix  $\mathbf{Y}$  of dimension  $D \times p$  such that  $\mathbf{Y}^T \mathbf{Y} = \mathbf{I}_p$  ( $\mathbf{I}_p$  is an identity matrix of dimension  $p \times p$ ). If  $\text{span}(\mathbf{Y}_1)$

=  $\text{span}(\mathbf{Y}_2)$ , then only two matrices  $\mathbf{Y}_1$  and  $\mathbf{Y}_2$  are considered to be same, where  $\text{span}(\mathbf{Y})$  denotes the subspace spanned by the column vectors of  $\mathbf{Y}$  [72].

### Principal Angles

Let  $\mathbf{Y}_1$  and  $\mathbf{Y}_2$  be the two orthonormal matrices of dimension  $D \times p$ . The principal angles  $0 \leq \theta_1 \leq \dots \leq \theta_p \leq \pi/2$  between the two subspaces  $\text{span}(\mathbf{Y}_1)$  and  $\text{span}(\mathbf{Y}_2)$ , are defined as [72]:

$$\cos\theta_p = \max_{\mathbf{u}_p \in \text{span}(\mathbf{Y}_1)} \max_{\mathbf{v}_p \in \text{span}(\mathbf{Y}_2)} \mathbf{u}_p^T \mathbf{v}_p \quad (3.6)$$

subject to  $\mathbf{u}_p^T \mathbf{u}_p = \mathbf{v}_p^T \mathbf{v}_p = 1$ , and  $\mathbf{u}_p^T \mathbf{u}_i = \mathbf{v}_p^T \mathbf{v}_i = 0$ , ( $i = 1, \dots, p-1$ ).

The principal angles can be computed from the singular value decomposition (SVD) of  $\mathbf{Y}_1^T \mathbf{Y}_2$  as [72]:

$$\mathbf{Y}_1^T \mathbf{Y}_2 = \mathbf{U}(\cos\Theta)\mathbf{V}^T \quad (3.7)$$

where  $\mathbf{U} = [\mathbf{u}_1, \dots, \mathbf{u}_p]$ ,  $\mathbf{V} = [\mathbf{v}_1, \dots, \mathbf{v}_p]$ , and  $\cos\Theta = \text{diag}(\cos\theta_1, \dots, \cos\theta_p)$ . The cosines of the principal angles are also known as *canonical correlations*.

### Grassmann Metric

The main Grassmann distance (or metric) are as follows [72]:

- Projection Distance

This distance is the 2-norm of the sine of the principal angles.

$$d_{PD}(\mathbf{Y}_1, \mathbf{Y}_2) = \left( p - \sum_{i=1}^p \cos^2\theta_i \right)^{1/2} \quad (3.8)$$

- Binet-Cauchy Distance

This distance is defined as the product of the square of canonical correlations.

$$d_{BC}(\mathbf{Y}_1, \mathbf{Y}_2) = \left( 1 - \prod_i \cos^2\theta_i \right)^{1/2} \quad (3.9)$$

### 3.2.2 Proposed Test Statistics

A new method for detecting the presence of PU's signal in a Grassmann manifold is proposed. A Grassmann manifold is a collection of vector subspaces of a vector space [72] which is same as the dominant eigenspace of a signal. In [73], the dominant eigenspace is termed as Grassmann covariance matrix (GCM). The GCM is used because of its compact representation of signal, as most significant singular vectors are selected for making GCM [73]. By using GCM of the PU's signal and the received signal, principal angles based test statistic is defined, which is a modification of Binet-Cauchy metric. The cosines of principal angles are known as canonical correlation, and hence, the proposed method is based on the canonical correlation analysis (CCA). CCA is used to identify and measure the relationship between two sets of variables [74]. CCA determines a set of canonical variates which shows the maximum correlation of two data sets (the two data sets are received signal and PU's signal) and provides useful information about linear correlation between two data sets, while the PCA fails to explore this information. The new test statistic follows the concentration phenomena and hence, gives a valid test statistic.

Additionally in this work, CSS is also performed, where the secondary base station acts as fusion center or central controller. To minimize the communication overhead, OR-rule based decision at the fusion center is chosen, where each SU share's 1-bit decision ( $\mathcal{H}_0$  or  $\mathcal{H}_1$ ). In the OR-rule based decision [75], a fusion center declares the presence of primary transmitter if one of the SU shares the presence of a primary transmitter in its decision.

The proposed method is based on the CCA between the two data sets. These two data sets are formed with the help of the dominant eigenspace of  $\mathbf{R}_{yy}$  (given in (3.2)) and the dominant eigenspace of  $\mathbf{R}_{xx}$  (given in (3.3)). This dominant eigenspace is termed as GCM as defined in [73]. A GCM is formed with the help of selecting the most significant singular vectors of sample covariance matrix of a signal. The formation of GCM follows the same procedure as given in [73], however, the Grassmann

metric or test statistic is different from [73], which is further analyzed in detail for SS. The new test statistic depends on the principal angles between the two data sets or GCM. In the following subsections, the formation of GCM, and the validity of choosing test statistic for SS in CR are discussed.

### GCM Formation

In the proposed method, the generation of GCM is as follows: Let  $\mathbf{R}$  be a symmetric covariance matrix of dimension  $D \times D$ , which is orthogonalized by SVD as:

$$\mathbf{R} = \mathbf{Y}\Sigma\mathbf{Y}^T \quad (3.10)$$

where  $\mathbf{Y} = [\mathbf{y}_1, \dots, \mathbf{y}_D]$  is an orthonormal matrix and  $\Sigma$  is a diagonal matrix of non-negative singular values. The first  $p$  ( $p \ll D$ ) column vectors of  $\mathbf{Y}$  contains the most important features of a signal. The sets of  $p$ -dimensional subspace of the  $\mathbb{R}^D$  form the Grassmann manifold  $\mathcal{G}(p, D)$  for SS, where  $\bar{\mathbf{Y}}$  ( $\bar{\mathbf{Y}} = [\mathbf{y}_1, \dots, \mathbf{y}_p]$ ) is denoted as GCM. Hence for two GCMs,  $\bar{\mathbf{Y}}_1$  and  $\bar{\mathbf{Y}}_2$ , the principal angles are calculated as given in (3.7).

For SS, the SVD of  $\mathbf{R}_{xx}$  and  $\mathbf{R}_{yy}$  can be written as:

$$\mathbf{R}_{xx} = \mathbf{X}\Sigma_x\mathbf{X}^T, \quad \text{and} \quad \mathbf{R}_{yy} = \mathbf{Y}\Sigma_y\mathbf{Y}^T \quad (3.11)$$

where  $\mathbf{R}_{xx}$  is the sample covariance matrix of PU's signal,  $\mathbf{R}_{yy}$  is the sample covariance matrix of the received signal,  $\mathbf{X}$  and  $\mathbf{Y}$  are the orthonormal matrices of dimension  $D \times D$ .  $\Sigma_x$  and  $\Sigma_y$  are the diagonal matrices of dimension  $D \times D$  of  $\mathbf{X}$  and  $\mathbf{Y}$ , respectively.

Let the two GCMs be  $\bar{\mathbf{X}}$  and  $\bar{\mathbf{Y}}$  which are formed by selecting the first  $p$  column vectors of  $\mathbf{X}$  and  $\mathbf{Y}$ , respectively. The principal angles between  $\bar{\mathbf{X}}$  and  $\bar{\mathbf{Y}}$  are calculated as given in (3.7). On the basis of principal angles a new test statistic ( $\rho$ ) is defined which is the modification of Binet-Cauchy distance. The new test statistic

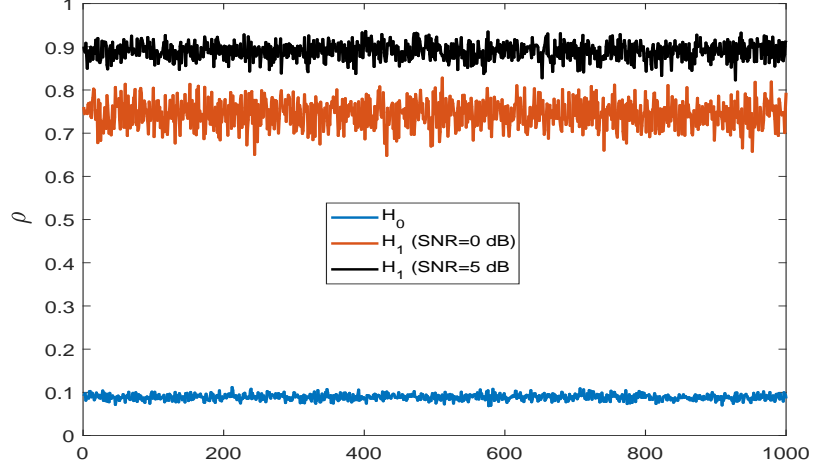


Figure 3.1: Values of  $\rho$  under two hypotheses from 1000 simulations.

$\rho$  ( $0 \leq \rho \leq 1$ ) is defined as:

$$\rho = \left( \prod_i^p \cos^2 \theta_i \right)^{1/2} \quad (3.12)$$

Thus, from Fig. 3.1, under  $\mathcal{H}_0$ ,  $\mu_\rho \rightarrow 0$ , and under  $\mathcal{H}_1$ ,  $\mu_\rho \rightarrow 1$ , where  $\mu_\rho$  is the mean of  $\rho$ .

In [62] through simulation, it is verified that the eigenvectors corresponding to the  $p$  largest eigenvalue of the captured DTV signal are stable and robust over time. Thus, the GCM,  $\bar{\mathbf{X}}$ , corresponding to the PU's as *a priori* information is used for calculating the proposed test statistic.

### Validity of Test Statistic ( $\rho$ )

The validity of  $\rho$  is proven by concentration inequality. According to concentration phenomenon [56], for a small value of  $\epsilon$  ( $\epsilon > 0$ ), there is a high probability that

$$\mu_\rho - \epsilon \leq |\rho| \leq \mu_\rho + \epsilon \quad (3.13)$$

The inequality shows that the  $|\rho|$  is not spread over its whole support  $[0,1]$ , rather than  $|\rho|$  is highly concentrated around  $\mu_\rho$ . Hence, under  $\mathcal{H}_0$ , there is a high probability that

$$\mu_{\rho_0} - \epsilon \leq |\rho| \leq \mu_{\rho_0} + \epsilon \quad \text{under } \mathcal{H}_0 \quad (3.14)$$

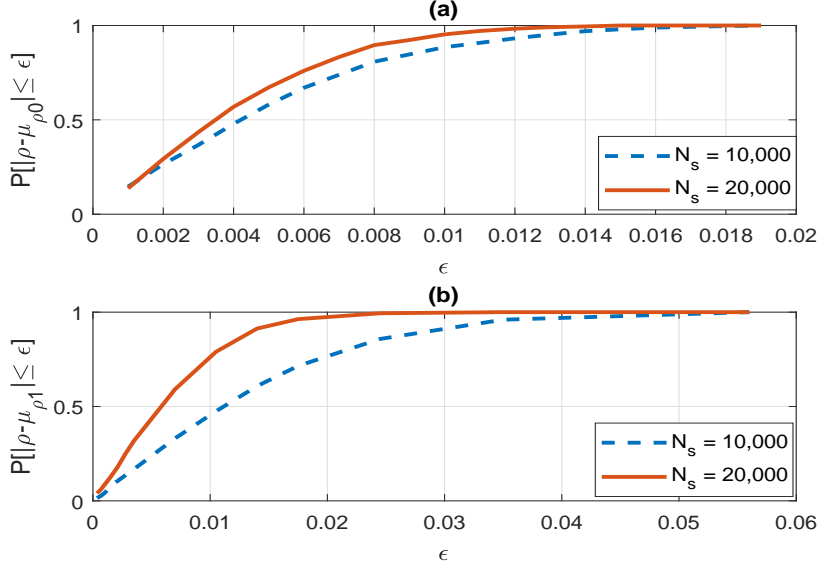


Figure 3.2: (a) Concentration phenomena of  $\rho$  under  $\mathcal{H}_0$  and (b) Concentration phenomena of  $\rho$  under  $\mathcal{H}_1$ .

and under,  $\mathcal{H}_1$

$$\mu_{\rho_1} - \epsilon \leq |\rho| \leq \mu_{\rho_1} + \epsilon \quad \text{under } \mathcal{H}_1 \quad (3.15)$$

where  $\mu_{\rho_0}$  and  $\mu_{\rho_1}$  are the mean value of  $\rho$  under  $\mathcal{H}_0$  and  $\mathcal{H}_1$ , respectively and  $\mu_{\rho_1} > \mu_{\rho_0}$  as shown in Fig. 3.1.

Fig. 3.2 (a) and (b) show the concentration phenomena of  $\rho$  under  $\mathcal{H}_0$  and  $\mathcal{H}_1$  (5 dB SNR), respectively. It is observed from both Fig. 3.2 (a) and (b) that the concentration of  $\rho$  around its mean increases as the number of  $N_s$  increases. Hence, the test statistic  $\rho$  follows the concentration phenomena.

Thus, in order to detect PU, the test statistic of the proposed method is given as:

$$T_{GCM} = \rho \quad (3.16)$$

Hence, on basis of the above test statistic,  $\mathcal{H}_1$  is true if  $T_{GCM} > \gamma_{GCM}$ . In the next section, the distribution of  $\rho$  under both the hypothesis is derived.

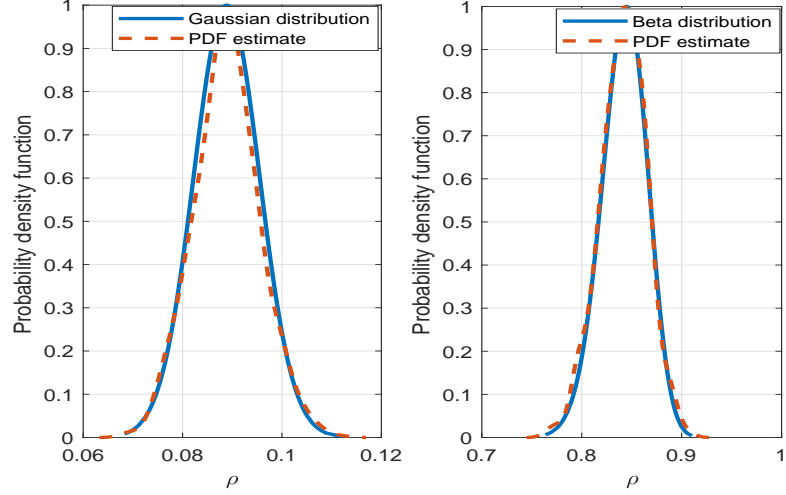


Figure 3.3: (a) Comparison of simulated and theoretical PDFs of  $\rho$  under  $\mathcal{H}_0$ , (b) Comparison of simulated and theoretical PDFs of  $\rho$  under  $\mathcal{H}_1$ .

### 3.2.3 Distribution Under Two Hypotheses

In this section, the PDF or distribution of  $\rho$  is estimated on the basis of simulation under two hypotheses. Then, signal detection threshold ( $\gamma_{GCM}$ ) on the basis of distribution of  $\rho$  under  $\mathcal{H}_0$ , and  $P_d$  and  $Q_d$  on the basis of distribution of  $\rho$  under  $\mathcal{H}_1$  are derived.

#### Distribution under $\mathcal{H}_0$

The PDF of  $\rho$  under  $\mathcal{H}_0$ , is required to estimate the threshold for PU's signal detection. From Fig. 3.3 (a), it is observed that the PDF of  $\rho$  under  $\mathcal{H}_0$  can be approximated by Gaussian distribution with mean  $\mu_{\rho_0}$  and variance  $\sigma_{\rho_0}^2$ . The  $\rho$  follows Gaussian distribution under  $\mathcal{H}_0$ , which is validated by Kolmogorov-Smirnov (KS) test. The KS test is used to decide if a sample comes from a population with a specific distribution. The "PDF estimate" in Fig. 3.3 (a) is obtained from the simulated  $\rho$  by non-parametric PDF estimation technique using Matlab function *ksdensity* which also shows the Gaussian distribution of  $\rho$  under  $\mathcal{H}_0$ . Thus, the PDF of  $\rho$  under  $\mathcal{H}_0$  can be written as:

$$f(\rho) = \frac{1}{\sqrt{2\pi\sigma_{\rho_0}^2}} e^{-\left(\frac{(\rho-\mu_{\rho_0})^2}{2\sigma_{\rho_0}^2}\right)} \quad (3.17)$$

Let  $P_f$  be the probability of false alarm, and  $\gamma_{GCM}$  be the threshold, then

$$P_f = \int_{\gamma_{GCM}}^{\infty} f(\rho) d\rho \quad (3.18)$$

Let

$$\frac{\rho - \mu_{\rho_0}}{\sigma_{\rho_0}} = t \quad (3.19)$$

then

$$d\rho = \sigma_{\rho_0} dt \quad (3.20)$$

After substituting (3.17), (3.19), and (3.20) in (3.18),  $P_f$  can be rewritten as:

$$P_f = \frac{1}{\sqrt{2\pi}} \int_{\frac{\gamma_{GCM} - \mu_{\rho_0}}{\sigma_{\rho_0}}}^{\infty} e^{-\left(\frac{t^2}{2}\right)} dt \quad (3.21)$$

$$P_f = Q\left(\frac{\gamma_{GCM} - \mu_{\rho_0}}{\sigma_{\rho_0}}\right) \quad (3.22)$$

Hence,  $\gamma_{GCM}$  can be calculated as:

$$\gamma_{GCM} = Q^{-1}(P_f)\sigma_{\rho_0} + \mu_{\rho_0} \quad (3.23)$$

## Distribution under $\mathcal{H}_1$

- **Local spectrum sensing**

It is observed that the PDF of  $\rho$  under  $\mathcal{H}_1$  can be approximated by Beta distribution ( $\beta(p, q)$ ) with mean  $\mu_{\rho_1}$  and variance  $\sigma_{\rho_1}^2$  as shown in Fig. 3.3 (b). The  $\rho$  follows the Beta distribution under  $\mathcal{H}_1$  is also validated by KS test. Hence, the pdf of  $\rho$  under  $\mathcal{H}_1$  can be written as:

$$f(\rho) = \frac{\rho^{p-1}(1-\rho)^{q-1}}{B(p, q)} \quad (3.24)$$

where  $p > 0$  and  $q > 0$  are scale parameters, and  $B(p, q)$  [76] is the Beta function.

The mean and variance of  $\rho$  under  $\mathcal{H}_1$  can be written as:

$$\mu_{\rho_1} = \frac{p}{p+q} \quad (3.25)$$

and

$$\sigma_{\rho_1}^2 \approx \frac{pq}{(p+q)^3}, \quad p, q \gg 1 \quad (3.26)$$

The detection probability,  $P_d$ , can be calculated as:

$$P_d = \int_{\gamma_{GCM}}^{\infty} f(\rho) d\rho \quad (3.27)$$

After substituting (3.24) into (3.27), leads to

$$P_d = \frac{1}{B(p, q)} \int_{\gamma_{GCM}}^{\infty} \rho^{p-1} (1-\rho)^{q-1} d\rho \quad (3.28)$$

$$P_d = 1 - \frac{1}{B(p, q)} \int_0^{\gamma_{GCM}} \rho^{p-1} (1-\rho)^{q-1} d\rho \quad (3.29)$$

$$P_d = 1 - I_{\gamma_{GCM}}(p, q) \quad (3.30)$$

where  $I_{\gamma_{GCM}}(p, q)$  is the regularized incomplete Beta function [76]. The  $p$  and  $q$  can be calculated (from  $\rho$ ) under  $\mathcal{H}_1$  as:

$$p = \frac{2\mu_{\rho_1} M_d - M_d}{3(M_d - \mu_{\rho_1})} \quad (3.31)$$

and

$$q = p \frac{(1 - \mu_{\rho_1})}{\mu_{\rho_1}} \quad (3.32)$$

where  $M_d$  is the median of  $\rho$  under  $\mathcal{H}_1$ .

- **Cooperative spectrum sensing**

The detection probability ( $Q_d$ ) for CSS can be calculated using (3.30). From (3.5),  $Q_d$  can be written as:

$$Q_d = 1 - Q_{md} = 1 - (P_{md})^{N_c} = 1 - (1 - P_d)^{N_c} \quad (3.33)$$

After substituting (3.30) into (3.33),  $Q_d$  can be rewritten as:

$$Q_d = 1 - (I_{\gamma_{GCM}}(p, q))^{N_c} \quad (3.34)$$

### 3.2.4 Lower Bound for Probability of Detection

In this section, the lower bound for the probability of signal detection for both the LSS and CSS using two different separating function (SF), and Fisher information matrix (FIM) are derived. An SF transforms the unknown parameters under  $\mathcal{H}_0$  and  $\mathcal{H}_1$  into two interval or axis. In [77], it is shown that if the minimum variance unbiased estimator (MVUE) of any SF exists then MVUE serves as the optimal test statistics for the uniformly most powerful unbiased test. It has been shown in the Section 3.2.3 that the proposed test statistic follows the  $\beta$  distribution, and it is complicated to find MVUE for  $\beta$  distribution with two unknown parameters  $p$  and  $q$ . Hence, an alternative is proposed (in [77]) to use other estimates of the unknown parameters and substitute in SF to get a sub-optimal bound.

Thus for the given problem, SF be represented as  $g(\cdot)$ , then by using Paley-Zygmund inequality [78], for an arbitrary  $c \in (0, 1)$  from [79]:

$$P\{\hat{g}(\theta) > c\mu_{\hat{g}(\theta)}\} \geq \frac{(1-c)^2\mu_{\hat{g}(\theta)}^2}{\sigma_{\hat{g}(\theta)}^2 + (1-c)^2\mu_{\hat{g}(\theta)}^2} \quad (3.35)$$

where  $\hat{g}(\theta)$  is the estimated SF,  $\mu_{\hat{g}(\theta)}$  is mean of  $\hat{g}(\theta)$ , and  $\sigma_{\hat{g}(\theta)}^2$  is variance of  $\hat{g}(\theta)$ . Let  $c = T_h/\hat{g}(\theta)$ , consider that  $\hat{g}(\theta)$  and  $\mu_{\hat{g}(\theta)}$  asymptotically tend to  $g(\theta)$  [79], and  $\sigma_{\hat{g}(\theta)}^2$  asymptotically tends to  $\frac{\partial g(\theta)^T}{\partial \theta} \mathbf{F}_\theta^{-1} \frac{\partial g(\theta)}{\partial \theta}$  which is the FIM of  $g(\theta)$  for all values of  $P_f$ . Thus, the above inequality can be written as:

$$P_d = P\{\hat{g}(\theta) > T_h\} \geq \frac{(g(\theta) - T_h)^2}{\frac{\partial g(\theta)^T}{\partial \theta} \mathbf{F}_\theta^{-1} \frac{\partial g(\theta)}{\partial \theta} + (g(\theta) - T_h)^2} \quad (3.36)$$

The above equation is only valid for  $\{\theta : g(\theta) > T_h\}$ . Thus, two SF based on  $\mu_\rho$  are taken and calculate the lower bound for  $P_d$ . One SF transforms the parameter  $A$  (or  $\mu_\rho$ ) into imaginary axis under  $\mathcal{H}_0$  and real axis under  $\mathcal{H}_1$ . While, the other SF transforms  $A$  into negative real value under  $\mathcal{H}_0$  and positive real value under  $\mathcal{H}_1$ .

## Separating Function 1 (SF1)

- Local spectrum sensing

Let SF1 be  $g(A) = \sqrt{\ln(A/\gamma_{GCM})}$ , as  $g(A)$  under  $\mathcal{H}_0$  is on the imaginary axis and under  $\mathcal{H}_1$  on the real axis. After employing inequality (3.36), a lower bound for  $P_d$  for SF1 is :

$$P_d \geq \frac{(\sqrt{\ln(\frac{A}{\gamma_{GCM}})} - \gamma_{GCM})^2}{\mathbf{b}^T \mathbf{C}^{-1} \mathbf{b} + (\sqrt{\ln(\frac{A}{\gamma_{GCM}})} - \gamma_{GCM})^2} \quad (3.37)$$

where

$$\mathbf{b} = \frac{1}{2A} \ln\left(\frac{A}{\gamma_{GCM}}\right)^{-1/2} \begin{bmatrix} q & -p \\ (p+q)^2 & (p+q)^2 \end{bmatrix}^T \quad (3.38)$$

and  $\mathbf{C}$  is given by:

$$\mathbf{C} = M_s \begin{bmatrix} \frac{(\Gamma p \Gamma'' p - (\Gamma' p)^2)}{(\Gamma p)^2} - \frac{(\Gamma(p+q) \Gamma''(p+q) - (\Gamma'(p+q))^2)}{(\Gamma(p+q))^2} & - \frac{(\Gamma(p+q) \Gamma''(p+q) - (\Gamma'(p+q))^2)}{(\Gamma(p+q))^2} \\ - \frac{(\Gamma(p+q) \Gamma''(p+q) - (\Gamma'(p+q))^2)}{(\Gamma(p+q))^2} & \frac{(\Gamma q \Gamma'' q - (\Gamma' q)^2)}{(\Gamma q)^2} - \frac{(\Gamma(p+q) \Gamma''(p+q) - (\Gamma'(p+q))^2)}{(\Gamma(p+q))^2} \end{bmatrix} \quad (3.39)$$

where  $\Gamma, \Gamma'$  and  $\Gamma''$  represent gamma function, first order derivative of gamma function and second order derivative gamma function, respectively. The proof of (3.37) is given in Appendix F.

- Cooperative spectrum sensing

After substituting (3.37) into (3.33), a lower bound for  $Q_d$  for SF1 can be calculated as:

$$Q_d \geq 1 - \left( \frac{(\sqrt{\ln(\frac{A}{\gamma_{GCM}})} - \gamma_{GCM})^2}{\mathbf{b}^T \mathbf{C}^{-1} \mathbf{b} + (\sqrt{\ln(\frac{A}{\gamma_{GCM}})} - \gamma_{GCM})^2} \right)^{N_c} \quad (3.40)$$

## Separating Function 2 (SF2)

- Local spectrum sensing

Let SF2 be  $g(A) = \ln(A/\gamma_{GCM})$ , as  $g(A)$  under  $\mathcal{H}_0$  is the negative real value and under  $\mathcal{H}_1$  is the positive real value. After employing inequality (3.36), a lower bound for  $P_d$  for SF2 is :

$$P_d \geq \frac{(\ln(\frac{A}{\gamma_{GCM}}) - \gamma_{GCM})^2}{\mathbf{d}^T \mathbf{C}^{-1} \mathbf{d} + (\ln(\frac{A}{\gamma_{GCM}}) - \gamma_{GCM})^2} \quad (3.41)$$

where

$$\mathbf{d} = \frac{1}{A} \begin{bmatrix} q & -p \\ (p+q)^2 & (p+q)^2 \end{bmatrix}^T \quad (3.42)$$

The proof of (3.41) is given in Appendix G.

### Cooperative spectrum sensing

After substituting (3.41) into (3.33), a lower bound for  $Q_d$  for SF2 can be calculated as:

$$Q_d \geq 1 - \left( \frac{(\ln(\frac{A}{\gamma_{GCM}}) - \gamma_{GCM})^2}{\mathbf{d}^T \mathbf{C}^{-1} \mathbf{d} + (\ln(\frac{A}{\gamma_{GCM}}) - \gamma_{GCM})^2} \right)^{N_c} \quad (3.43)$$

### 3.2.5 Results and Complexity Discussion

In this section, the performance of proposed method by simulation and experiments is evaluated. Comparison of computational complexity of the proposed method with the conventional methods is discussed.

#### Simulation Results

To evaluate performance of the proposed method, real world measurement of DTV signal [80] captured with the duration of approximately 25 seconds in Washington DC, USA as a PU's signal is used. Received SNR and communication channel between the transmitter and the receiver are unknown. DTV signal is used as PU for simulation since it is a major source of primary transmission for IEEE 802.22 WRAN, which operates on TVWS [20]. For all the results, 1000 Monte Carlo simulations are performed with  $L_s = 50$ ,  $M_s = 200$ , and number of samples,  $N_s(L_s \times M_s) = 10,000$ . To obtain various SNR level, Gaussian noise is added to the primary signal as given in IEEE 802.22 standard [81]. In SS, the  $p$  largest eigenvectors of the

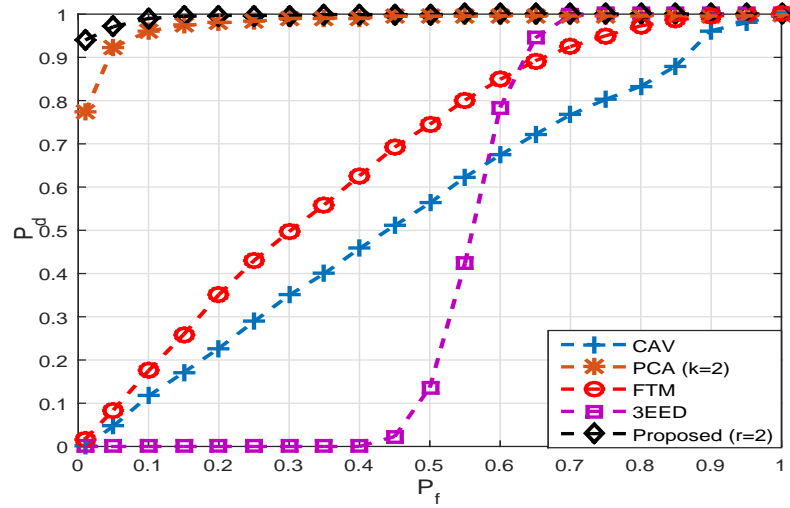


Figure 3.4: ROC curves of proposed and conventional methods at -20dB SNR.

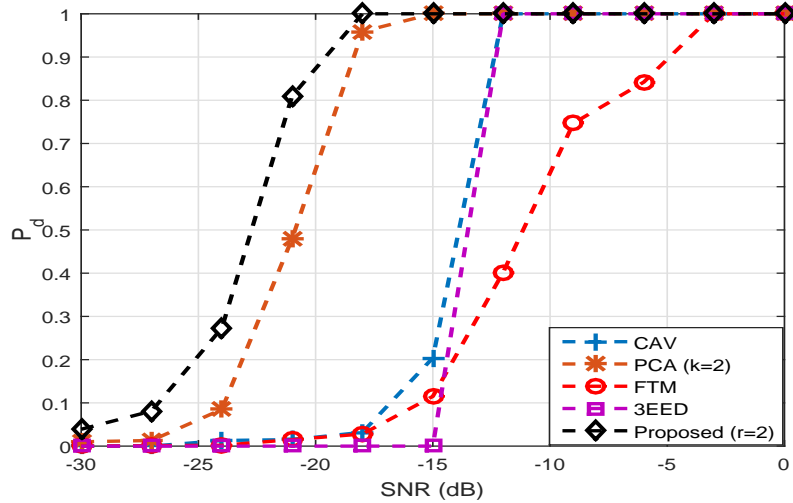


Figure 3.5:  $P_d$  of proposed and conventional method with  $P_f$  of 0.01.

captured DTV signal is considered *a priori* as a PU's feature in [56]. Similarly, in [62], the principal eigenvector of the captured DTV signal is used as *a priori* signal feature. Thus, similar to [56, 62], the  $p$  largest eigenvectors of DTV signal *a priori* is used to form  $\bar{\mathbf{X}}$  which is one of the GCMs.

Fig. 3.4 shows the receiver operating characteristic (ROC) curve for the proposed and the conventional methods at the SNR of -20dB. ROC curve shows the  $P_d$  vs  $P_f$ . Fig. 3.4 shows that at -20dB SNR, the proposed method detects signal ( $P_d = 1$ ) at  $P_f = 0.1$ , whereas other conventional methods like CAV, FTM, and 3EED require very large  $P_f$  to detect signal. Hence, the proposed method improves the spectrum

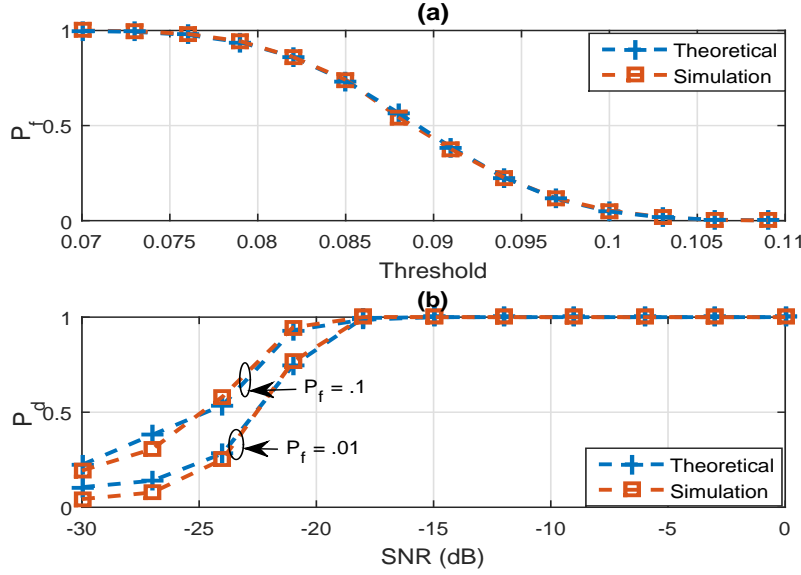


Figure 3.6: Comparison of simulated and theoretical (a)  $P_f$  of proposed method with threshold and (b)  $P_d$  of proposed method with  $P_f$  of 0.01 and 0.1.

utilization as compared to the conventional methods. Fig. 3.5 shows the  $P_d$  vs SNR graph for the proposed and the conventional methods with  $P_f = 0.01$ . It is observed from Fig. 3.5 that the proposed method provides 3dB SNR gain as compared to PCA, 6 dB SNR gain as compared to CAV and 3EED, and 15dB SNR gain as compared FTM at  $P_d = 1$ . Hence, the proposed method detects very low power PU's signal and, thus avoids the SUs to interfere with PU. It is observed from Fig. 3.4 and Fig. 3.5 that the performance of PCA based detector is better than CAV, FTM, and 3EED since the PU's signal can be reduced into low-dimension subspace. However, PCA fails to explore the correlation between the two data sets, while CCA uses this information and hence the CCA based proposed detector performs better as compared to the PCA based detector.

Fig. 3.6 (a) shows comparison of the simulated and the theoretical  $P_f$  of the proposed method, and Fig. 3.6 (b) shows the comparison of simulated and theoretical  $P_d$  of the proposed method with  $P_f$  of 0.01 and 0.1. It is observed from Fig. 3.6 (a) that the simulation results follow the theoretical results, and also from Fig. 3.6 (b) that the simulation results approximately follow the theoretical result which validates the statistics derived under two hypotheses. Fig. 3.7 shows comparison of

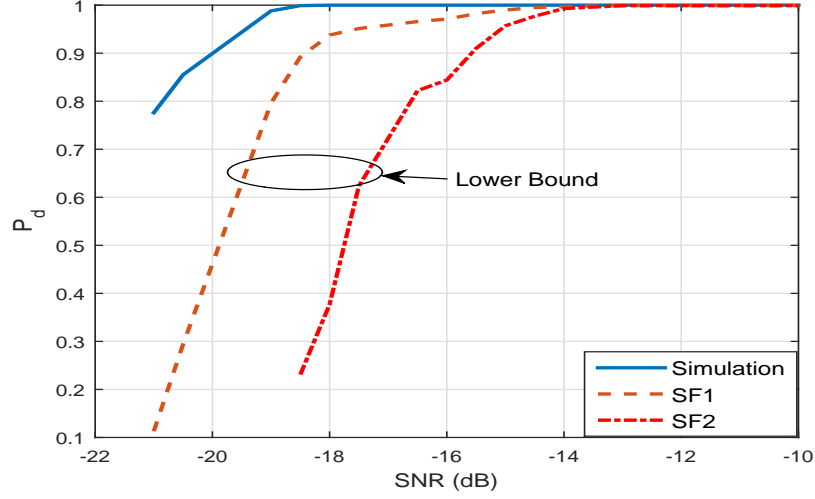


Figure 3.7: Comparison of lower bound of  $P_d$  with  $P_f$  of 0.01 using SF1 and SF2.

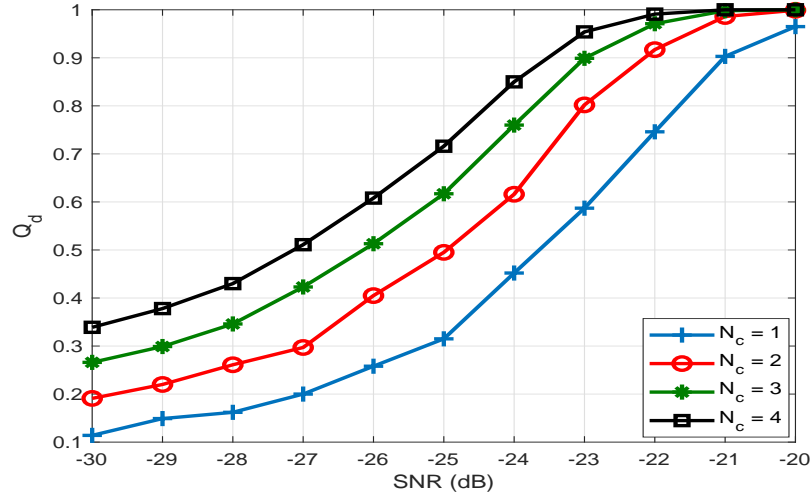


Figure 3.8:  $Q_d$  of proposed method for different values of  $N_c$  at  $P_f = 0.05$ .

the lower bound of  $P_d$  with  $P_f = 0.01$  using SF1 and SF2. Both SF1 and SF2 give lower bound, however SF1 has a larger valid region and provides tighter bound as compared to SF2 as shown in Fig. 3.7. Hence, there are various SFs for a particular problem which gives different bounds.

Fig. 3.8 shows the  $Q_d$  vs SNR for the proposed method at  $P_f = 0.05$  for different values of  $N_c$  and the channels between the primary transmitter and SUs are assumed to be i.i.d.. It is observed from Fig. 3.8, that the CSS increases the detection probability as compared to LSS ( $N_c = 1$ ) for same SNR and  $P_f$ . It is also observed from Fig. 3.8 that the CSS significantly improves the average SNR for detection.

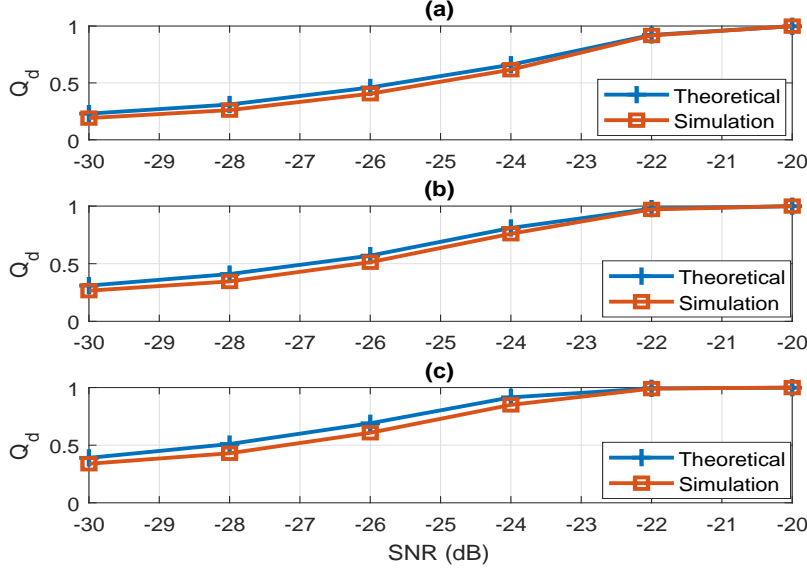


Figure 3.9: Comparison of simulated and theoretical  $Q_d$  at  $P_f = 0.05$  for (a)  $N_c = 2$ , (b)  $N_c = 3$  and (c)  $N_c = 4$ .

In particular, for a  $P_d$  equal to 0.9, LSS requires  $\text{SNR} = -21$  dB while CSS with  $N_c = 4$  requires  $\text{SNR}$  of  $-23.5$  dB for individual SUs. However, the performance of CSS degrades if the channels between the primary transmitter and the SUs are correlated.

Fig. 3.9 shows the comparison of theoretical and simulated  $Q_d$  at  $P_f = 0.05$  for different values of  $N_c$ . It is observed from Fig. 3.9 that the simulation results of  $Q_d$  follow the theoretical  $Q_d$  given in (3.34) for different values of  $N_c$ . It is also observed from Fig. 3.9 that the theoretical  $Q_d$  gives upper bound since (3.34) is derived under perfect i.i.d. channels between the primary transmitter and the SUs. Fig. 3.11 shows comparison of lower bound  $Q_d$  at  $P_f = 0.05$  using SF1 and SF2 for different value of  $N_c$ . It is observed from Fig. 3.11 that both SF1 and SF2 give lower bound. However, SF1 has larger valid region and provides tighter bound as compared to SF2.

## Experimental Results

To validate the algorithm while considering practical constraints, real world measurement of DTV signal captured with the duration of about 25 seconds in New

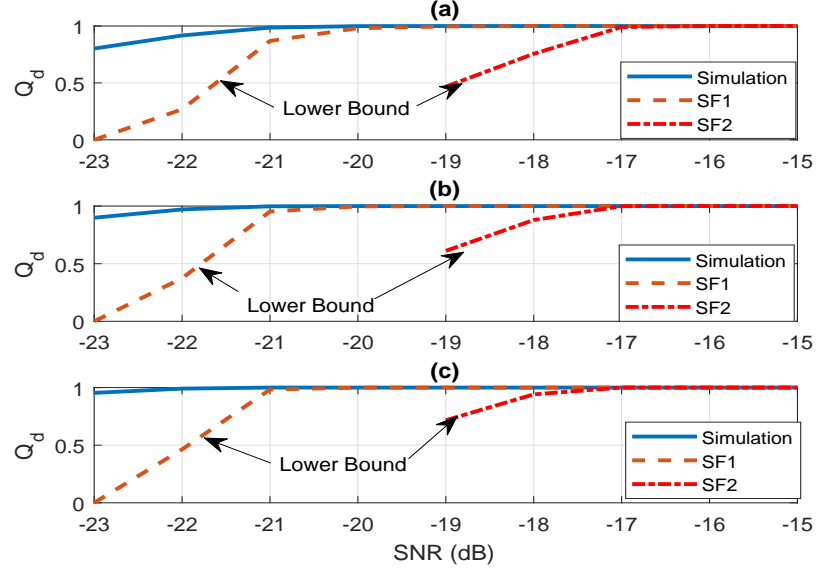


Figure 3.10: Comparison of lower bound of  $Q_d$  at  $P_f = 0.05$  using SF1 and SF2 for (a)  $N_c = 2$ , (b)  $N_c = 3$  and (c)  $N_c = 4$ .

Delhi, India at 538 MHz as a PU signal is used [82]. Again the received SNR and communication channel between the transmitter and the receiver are unknown. Similar to the simulation subsection, the  $p$  largest eigenvectors of DTV signal *a priori* is used to form  $\bar{\mathbf{S}}$ , which is one of the GCMs. The Federal Communications Commission has set a strict guideline on in-band sensing in order to obtain maximum protection of PUs. For example, in IEEE 802.22 WRAN, the PU's signal should be detected within 2 second with the  $P_f(Q_f) \leq 0.1$ ,  $P_{md}(Q_{md}) \leq 0.1$  and  $P_d(Q_d) \geq 0.9$  [20]. Hence, in order to meet these requirements, in-band sensing must be run once every 2 seconds and a detection method (e.g., energy or feature detection) that give better performance should be used. The effect of SS on SUs' quality-of-service should also be considered since sensing is performed during *quiet periods* within which communication between SUs are suspended [83]. The IDT of DTV signal is -116 dBm at 6 MHz bandwidth [71] which means the IEEE 802.22 device must vacate channel if it detects received signal strength (RSS) of -116 dBm or above. Hence, the  $P_d(Q_d)$  is calculated on the basis of RSS.

An experimental station has been set up at Signal and Software Group research lab in IIT Indore as shown in Fig. 3.11 to evaluate the performance of proposed

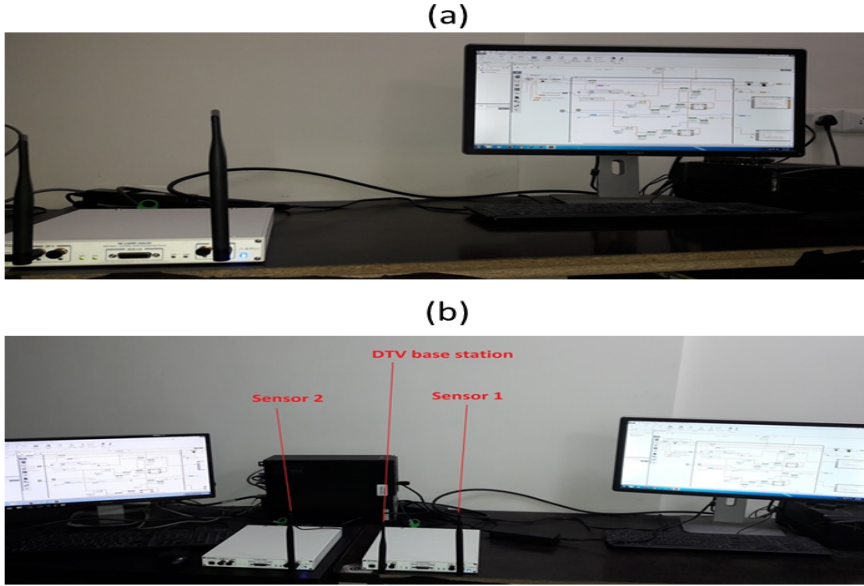


Figure 3.11: Experimental setup for (a) local spectrum sensing and (b) cooperative spectrum sensing.

signal detection method in real time. It consists of a desktop (having Intel(R) Xenon(R) CPU E5-1260 v3 @ 3.50 GHz processor with 64 GB RAM) which is connected with NI-USRP 2952R board. A USRP 2952R board can operate in 400 MHz-4.4 GHz with 40 MHz real time bandwidth and is used as transceiver which transmits and receives the signal at 550 MHz with 6 MHz sampling rate. Fig. 3.11 (a) shows the setup for LSS.

Fig. 3.12 (a) shows the  $P_d$  vs average RSS of the proposed method at  $P_f = 0.05$  and 0.1. It is observed from Fig. 3.12 (a) that when  $N_s = 20000$  ( $L_s = 50$ ,  $M_s = 400$ ), the proposed method for both values of  $P_f$  fulfills the IDT requirement of DTV signal as the  $P_d > 0.9$  for average RSS of -116 dBm and above. It is also observed from Fig. 3.12 (a) that when  $N_s = 10000$  the proposed method for both values of  $P_f$  fails to achieve the IDT requirement of DTV signal. However, the sensing time (sensing time includes  $N_s$  captured and computational time) for  $N_s = 10000$  is very low (about 6.911 ms) as compared to  $N_s = 20000$  (about 22.7475 ms). However, sensing time can be reduced by CSS by deploying sensors at multiple locations.

For IEEE 802.22, CPEs can be used as sensors for detecting DTV signal. Fig. 3.11 (b) shows the experimental setup for CSS where two sensors are used to detect

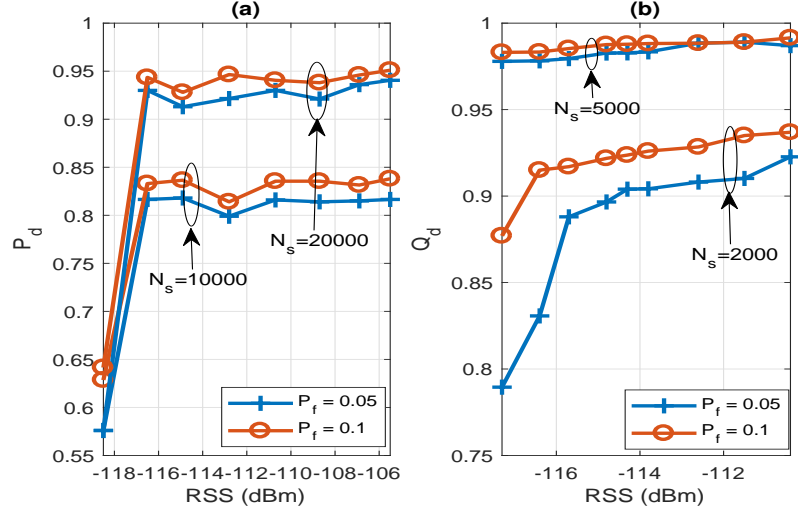


Figure 3.12: (a)  $P_d$  vs average RSS of proposed method, (b)  $Q_d$  vs average RSS of proposed method for 2 secondary user.

the DTV signal. Fig. 3.12 (b) shows the  $Q_d$  vs average RSS at  $P_f = 0.05$  and  $0.1$  for  $N_s = 2000$  ( $L_s = 20, M_s = 100$ ) and  $5000$  ( $L_s = 20, M_s = 250$ ) with 2 sensors. It is observed from Fig. 3.12 (b) that both the values of  $N_s$  fulfill the IDT requirement of DTV signal as the  $Q_d > 0.9$  ( $P_f = 0.1$ ) for average RSS of  $-116$  dBm and above. Moreover, the sensing time for  $N_s = 5000$  and  $N_s = 2000$  is about  $5.0343$  ms and  $4.2575$  ms, respectively. It is also observed from Fig. 3.12 (b) that the DTV base station and Sensor-1 is connected to the same USRP and Sensor-2 is connected to another USRP, hence for same  $P_f$ ,  $P_d$  of Sensor-1 is higher than Sensor-2 because of being on the same board, the transmitter and the receiver are automatically synchronized. However, in real-world scenario, CPEs are not synchronized with transmitted DTV signal and hence on the basis of  $P_d$  of Sensor-2 (which is not synchronized with DTV signal), from (3.5) it is found that at least 3 and 7 sensors are required for  $N_s = 5000$  and  $2000$ , respectively for fulfillment of the IDT requirement for DTV signal.

### Computational Complexity

Computation of the sample covariance matrix and its SVD are the two major computationally complex parts of the proposed algorithm. For sample covariance matrix,

all the methods except 3EED detector need  $(M_s(L_s(L_s + 1)/2))$  multiplications and  $((M_s - 1)L_s(L_s + 1)/2)$  additions. 3EED has least complexity because of only energy calculation, FTM needs additional  $2O(L_s^3)$  computations for eigenvalue decomposition (EVD) of  $\mathbf{R}_{yy}$  and  $\mathbf{R}_{xx}$ , and PCA needs additional  $O(L_s^3)$  computation for EVD of  $\mathbf{R}_{yy}$ . Proposed method needs extra  $2O(2L_s^3)$  computation for SVD of  $\mathbf{R}_{yy}$  and  $\mathbf{R}_{xx}$ , and  $O(p^3)$  computation of singular values between  $\bar{\mathbf{X}}$  and  $\bar{\mathbf{Y}}$ . However, since  $p \ll D$ , hence extra computation complexity of the proposed algorithm is  $\approx 2O(2L_s^3)$ . Hence, the computational complexity of the proposed method is higher than CAV, and PCA, and is closer to FTM. With the use of fast PCA algorithm [84], computation of EVD and SVD can be further reduced, and hence the proposed method is suitable for real-time hardware implementation.

### 3.3 LogDet Covariance based Spectrum Sensing under Colored Noise

In this section, the LogDet covariance based test statistics is proposed in the presence of colored Gaussian noise. The detection threshold of the proposed algorithms are also derived. Simulation results show robustness of the proposed algorithms over existing algorithms on the captured DTV signal.

#### 3.3.1 LogDet Covariance based Test Statistics

The covariance matrix of received signal in the presence of colored noise may have swelling effect due to spurious variation to the signal [85], and hence Euclidean geometry is unsuitable for SPD. The influence of swelling effect on the signal is observed by the condition number (ratio of the maximum eigenvalue to the minimum eigenvalue) of the covariance matrix of the signal. If the signal is influenced by the swelling effect, then the condition number is much greater than one otherwise it is nearly equal to one. The positive-definiteness constraint induces a Riemannian manifold of negative curvature [85] and thus in this subsection, LogDet metric is used as

it is closely related to the Riemannian metric. In this subsection, two LogDet based metric known LogDet of received samples covariance matrix (LDRSCM), and energy with LDRSCM (ELDRSCM) are proposed. Since, threshold is used for identifying presence of PU, the threshold used in LDRSCM depends on the noise variance, whereas the threshold used in ELDRSCM does not. This makes ELDRSCM more robust and versatile than LDRSCM. Let the RSCM of  $j^{th}$  sub-segment be denoted as:

$$\mathbf{R}_{yy,j} = \frac{1}{M_s} \sum_{i=(j-1)M_s+1}^{(j-1)M_s+M_s} \mathbf{y}(i)\mathbf{y}^T(i) \quad (3.44)$$

For large number of samples, it is assumed that  $x$  and  $w$  are uncorrelated, and hence

$$\mathbf{R}_{yy,j} = \mathbf{R}_{xx,j} + \mathbf{R}_{ww,j} \quad (3.45)$$

In the presence of PU for white Gaussian noise

$$\mathbf{R}_{yy,j} > \mathbf{R}_{ww,j} \quad (3.46)$$

From Minkowski determinant theorem [86], for two SPD  $\mathbf{A}$  and  $\mathbf{B}$

$$\det(\mathbf{A} + \mathbf{B}) \geq \det(\mathbf{A}) + \det(\mathbf{B}) \quad (3.47)$$

where  $\det(\cdot)$  represents the determinant of the matrix. From the above equation

$$\det(\mathbf{A} + \mathbf{B}) > \det(\mathbf{A}) \text{ or } \det(\mathbf{B}) \quad (3.48)$$

Since,  $\log(x)$  is an increasing continuous function for  $x > 0$ , hence from (3.48)

$$\log\det(\mathbf{A} + \mathbf{B}) > \log\det(\mathbf{A}) \text{ or } \log\det(\mathbf{B}) \quad (3.49)$$

Thus from (3.45), (3.46) and (3.49), and in the presence of PU's signal

$$\log\det(\mathbf{R}_{yy,j}) > \log\det(\mathbf{R}_{ww,j}) \quad (3.50)$$

In order to make the proposed metric robust, the average of sample covariance matrix is calculated and hence from (3.50)

$$\log\det\left(\frac{1}{J}\sum_{j=1}^J(\mathbf{R}_{yy,j})\right) > \log\det\left(\frac{1}{J}\sum_{j=1}^J(\mathbf{R}_{ww,j})\right) \quad (3.51)$$

Thus, the LDRSCM metric for signal detection is given as:

$$\rho_{p_1} = \log\det\left(\frac{1}{J}\sum_{j=1}^J(\mathbf{R}_{yy,j})\right) = \log\det(\mathbf{R}_{yy}^j) \quad (3.52)$$

However, the threshold of above metric depends on the noise variance as discussed in the next section. Thus, another metric known as ELDRSCM is proposed for both white and colored noise whose threshold does not depend on the noise variance as:

$$\rho_{p_2} = \begin{cases} \rho_{p_2}^w = \frac{\rho_{p_1}}{\log(T(N_s))}, & \text{for white noise} \\ \rho_{p_2}^c = \frac{\log(T(N_s))}{\rho_{p_1}}, & \text{for colored noise} \end{cases} \quad (3.53)$$

The correlation coefficient of white noise samples is nearly zero, while the correlation coefficient of colored noise samples is very high. Hence, on the basis of correlation coefficient the above metric is chosen.

### 3.3.2 Analysis Under $\mathcal{H}_0$

Since the signal detection is sensitive to selection of threshold, the threshold  $\gamma_{p_1}$  is derived for the LDRSCM which is based on PDF of  $\rho_{p_1}$  and  $P_f$  under  $\mathcal{H}_0$  in the presence of white noise. The  $\rho_{p_1}$  can also be written as:

$$\rho_{p_1} = \sum_{l=1}^{L_s} \log(\beta_l) \quad (3.54)$$

where  $\beta_l$  are the eigenvalue of  $\mathbf{R}_{yy}^j$ .

For large number of samples  $N_s (= L_s \times M_s)$ ,  $(\beta_{\max} - \mu)/\sigma$  can be approximated

as Tracy-Widom distribution of order 1 under  $\mathcal{H}_0$  with mean (or centering),  $\mu_{tw}$  and standard deviation (or scaling),  $\sigma_{tw}$  as in [61]

$$\mu_{tw} = \frac{\sigma_w^2}{N_s} (\sqrt{N_s} + \sqrt{L_s})^2 \quad (3.55)$$

and

$$\sigma_{tw} \approx \frac{\sigma_w^2}{N_s} (\sqrt{N_s} + \sqrt{L_s}) \left( \frac{1}{\sqrt{N_s}} + \frac{1}{\sqrt{L_s}} \right)^{1/3} \approx \frac{\mu}{(\sqrt{N_s} + \sqrt{L_s})} \left( \frac{1}{\sqrt{N_s}} + \frac{1}{\sqrt{L_s}} \right)^{1/3} \quad (3.56)$$

Since the LDRSCM metric also depends on the eigenvalue, PDF of  $(\rho_{p_1} - \mu_{p_1}^w)/\sigma_{p_1}^w$  can also be approximated as Tracy-Widom distribution of order 1 with centering,  $\mu_{p_1}^w$  and scaling,  $\sigma_{p_1}^w$  under  $\mathcal{H}_0$  in the presence of white noise as:

$$\mu_{p_1}^w = L_s \log(\sigma_w^2) \quad \text{and} \quad \sigma_{p_1}^w = \frac{|\log(|\mu_{p_1}^w|)|}{(\sqrt{N_s} + \sqrt{L_s})} \left( \frac{1}{\sqrt{N_s}} + \frac{1}{\sqrt{L_s}} \right)^{1/3} \quad (3.57)$$

The  $P_f$  can be calculated as:

$$P_f = \int_{\gamma_{p_1}^w}^{\infty} f(\rho_{p_1}) d\rho_{p_1} \quad (3.58)$$

where  $f(\rho_{p_1})$  is the PDF of  $\rho_{p_1}$  under  $\mathcal{H}_0$ . By using (3.57) and (3.58),  $\gamma_{p_1}^w$  can be calculated as:

$$\gamma_{p_1}^w = F_1^{-1}(1 - P_f) \frac{|\log(|\mu_{p_1}^w|)|}{(\sqrt{N_s} + \sqrt{L_s})} \left( \frac{1}{\sqrt{N_s}} + \frac{1}{\sqrt{L_s}} \right)^{1/3} + L_s \log(\sigma_w^2) \quad (3.59)$$

where  $F_1^{-1}(\cdot)$  is the inverse of Tracy-Widom distribution function of order 1. Hence, if  $\rho_{p_1} > \gamma_{p_1}^w$ , then PU signal ( $\mathcal{H}_1$ ) exists otherwise not.

Similarly, the PDF of  $(\rho_{p_1} - \mu_{p_1}^c)/\sigma_{p_1}^c$  in the presence of colored noise can again be approximated as Tracy-Widom distribution of order 1 with centering,  $\mu_{p_1}^c$  and scaling,  $\sigma_{p_1}^c$  under  $\mathcal{H}_0$  as:

$$\mu_{p_1}^c = \alpha L_s \log(\sigma_w^2) \quad \text{and} \quad \sigma_{p_1}^c = \frac{\alpha^2 |\log(|\mu_{p_1}^c|)|}{(\sqrt{N_s} + \sqrt{L_s})} \left( \frac{1}{\sqrt{N_s}} + \frac{1}{\sqrt{L_s}} \right)^{1/3} \quad (3.60)$$

where  $\alpha$  depends on the auto-correlation coefficients of colored noise upto  $L_s$  samples. Thus, by using (3.60),  $\gamma_{p_1}^c$  can be calculated as:

$$\gamma_{p_1}^c = F_1^{-1}(1 - P_f) \frac{\alpha^2 |\log(|\mu_{p_1}^c|)|}{(\sqrt{N_s} + \sqrt{L_s})} \left( \frac{1}{\sqrt{N_s}} + \frac{1}{\sqrt{L_s}} \right)^{1/3} + \alpha L_s \log(\sigma_w^2) \quad (3.61)$$

Both the thresholds derived in (3.59) and (3.61) for white and colored noise, respectively depend on the noise variance. Further, two threshold for ELDRSCM ( $\rho_{p_2}$ ) are derived in the presence of both white and colored noise, respectively, and show that these thresholds are independent of the noise variance. In the presence of white noise under  $\mathcal{H}_0$ , the PDF of  $\log T(N_s)$  can be approximated as Gaussian distribution with mean and standard deviation as  $\log(\sigma_w^2)$  and  $2L_s \log(\sigma_w^2)/N_s$ , respectively. Hence, the  $P_f$  for threshold  $\gamma_{p_2}^w$  can be calculated as:

$$P_f = P(\rho_{p_1} > \gamma_{p_2}^w \log(T(N_s))) = 1 - P\left(\log(T(N_s)) > \frac{\rho_{p_1}}{\gamma_{p_2}^w}\right) \quad (3.62)$$

According to concentration inequalities, a random variable is concentrated around its mean for large number of samples. Thus, for large number of  $N_s$ ,  $\rho_{p_1}$  with its mean  $L_s \log(\sigma_w^2)$  is replaced in equation (3.62). Thus, the (3.62) can be rewritten as:

$$\begin{aligned} 1 - P_f &= P\left(\log(T(N_s)) > \frac{L_s \log(\sigma_w^2)}{\gamma_{p_2}^w}\right) \quad (3.63) \\ &= P\left(\frac{\log(T(N_s)) - \log(\sigma_w^2)}{\frac{2L_s \log(\sigma_w^2)}{N_s}} > \frac{\frac{L_s \log(\sigma_w^2)}{\gamma_{p_2}^w} - \log(\sigma_w^2)}{\frac{2L_s \log(\sigma_w^2)}{N_s}}\right) = Q\left(\frac{\frac{L_s \log(\sigma_w^2)}{\gamma_{p_2}^w} - \log(\sigma_w^2)}{\frac{2L_s \log(\sigma_w^2)}{N_s}}\right) \end{aligned} \quad (3.64)$$

where  $Q(t) = 1/\sqrt{2\pi} \int_t^\infty e^{-x^2/2} dx$ . Thus  $\gamma_{p_2}^w$  can be calculated as:

$$\gamma_{p_2}^w = \frac{N_s L_s}{N_s + 2L_s Q^{-1}(1 - P_f)} \quad (3.65)$$

Thus, from (3.65), the threshold is not related to the noise power, and hence can be pre-computed based only on the known data. Similarly, in the presence of colored noise under  $\mathcal{H}_0$ , the PDF of  $\log T(N_s)$  can be approximated as Gaussian distribution

with mean and standard deviation as  $\log(\sigma_w^2)$  and  $\log(\sigma_w^2)/\alpha\sqrt{L_s N_s}$ , respectively. Hence, the  $P_f$  for threshold  $\gamma_{p_2}^c$  can be calculated as:

$$P_f = P(\log(T(N_s)) > \gamma_{p_2}^c \rho_{p_1}) \quad (3.66)$$

Similarly,  $\gamma_{p_2}^c$  can be calculated as:

$$\gamma_{p_2}^c = \frac{\alpha\sqrt{N_s L} + Q^{-1}(P_f)}{\alpha^2 L_s \sqrt{N_s L_s}} \quad (3.67)$$

Similar to  $\gamma_{p_2}^c$ , the above threshold is also not related to noise variance and can be pre-computed. Since, the variation of  $\alpha$  is much slower than the variation of noise power with time, and hence ELDRSCM is more robust and versatile than LDRSCM.

### 3.3.3 Simulation Results and Discussion

In this section, the performance of proposed algorithm in terms of signal detection on real world DTV signal captured in Washington DC, USA [80] as PU's is investigated. The colored noise used in the simulation is modeled as pink noise or flicker noise having power spectral density inversely proportional to the frequency of signal and falls off at 3 dB per octave. The detection is carried over an ensemble of 500-runs with  $M_s=1000$ ,  $L_s=10$ , and  $J=10$ . The existing algorithms and the proposed algorithms for SS are categorized into two classes based on the threshold used for signal detection. The detection threshold for Class-1 depends on the noise variance and Class-1 includes the ME, FTM, FMD, MECN and the proposed LDRSCM based detection algorithms. Whereas, the detection threshold for Class-2 is independent of noise variance and Class-2 includes CAV, SLE, MME, EME, SCN, and the proposed ELDRSCM based detection algorithms. Hence, the algorithms under Class-2 are more robust than the algorithms in Class-1 in the presence of noise uncertainty.

Fig. 3.13 shows the  $P_d$  vs SNR of signal capture in USA for white noise at  $P_f=0.05$ . It is observed that, LDRSCM provides 3 dB gain over ME, and 10 dB gain over FTM. It is also observed from Fig. 3.13 that the ELDRSCM provides 3

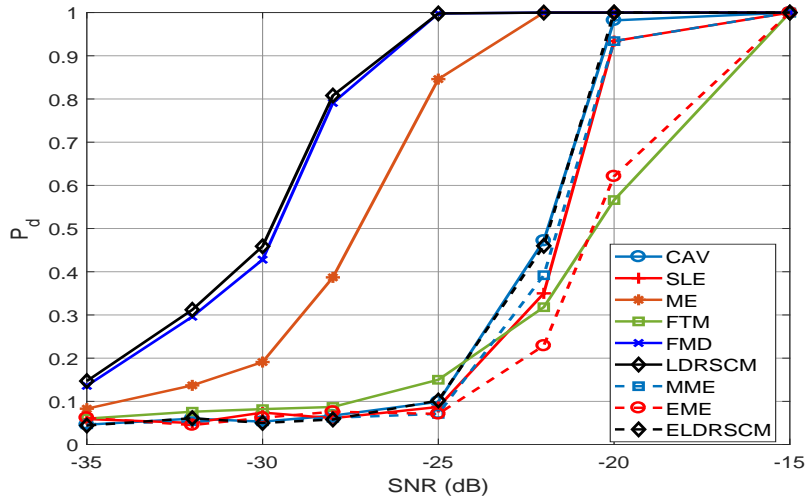


Figure 3.13:  $P_d$  vs SNR of signal capture in USA for white noise at  $P_f=0.05$ .

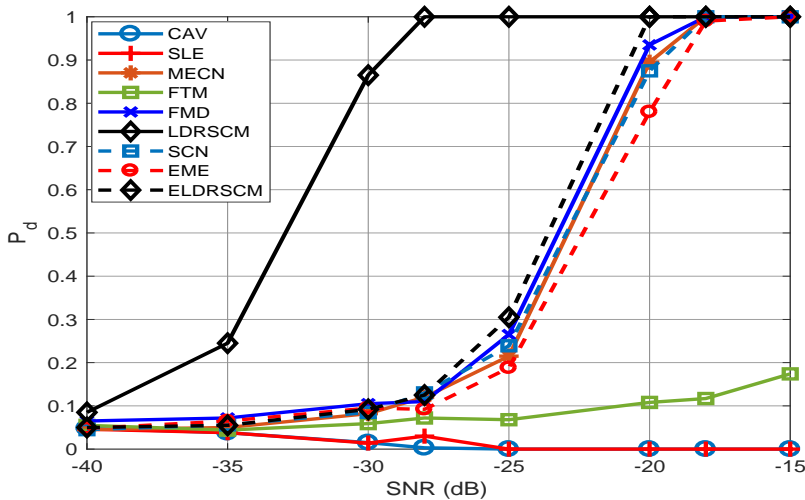


Figure 3.14:  $P_d$  vs SNR of signal capture in USA for colored noise at  $P_f=0.05$ .

dB gain than MME, SLE and CAV, 5 dB gain than EME. The performance of FMD and LDRSCM is same as observed from 3.13. The proposed metric again provides 3 dB gain over ME and 10 dB gain over FTM.

Fig. 3.14 shows the  $P_d$  vs SNR of signal capture in USA for colored noise at  $P_f=0.05$ . It is observed from Fig. 3.14 that LDRSCM significantly improves the signal detection than existing metrics. Fig. 3.14 shows that the LDRSCM provides 10 dB gain and ELDRSCM provides 2 dB gain over EME, FMD, SCN and MECN. It is also observed from Fig. 3.14 that CAV, SLE, and FTM fail to detect the signal in the presence of colored noise. The ME in Fig. 3.13 represents the

maximum eigenvalue of the covariance matrix of the received signal in the presence of white noise, whereas, MECN in Fig. 3.14 represents the maximum eigenvalue of the covariance matrix of the received signal in the presence of colored noise. It is observed from 3.13 and 3.14 that the LDRSCM performs much better than ELDRSCM, however the performance of LDRSCM is sensitive to noise variance which makes ELDRSCM more suitable for practical systems.

It is also observed from Fig. 3.13 and 3.14 that the SLE and CAV fails to detect the signal in the presence of colored noise. The reason is follows: The samples are uncorrelated for white noise, less correlated for the captured DTV signal and highly correlated for colored noise. In the presence of PU, the correlation coefficient of the received samples reaches the correlation coefficient of the captured DTV signal. This implies that in the presence of white noise, the correlation coefficient of the received samples increases from  $\mathcal{H}_0$  to  $\mathcal{H}_1$ . While in the presence of colored noise, the correlation coefficient of the received samples decreases from  $\mathcal{H}_0$  to  $\mathcal{H}_1$ . For uncorrelated samples, eigenvalues of covariance matrix are nearly equal and the off-diagonal elements of covariance matrix are nearly zero. While, for highly correlated samples, largest eigenvalue is very high as compared to smallest eigenvalue of covariance matrix and the off-diagonal elements are greater than zero. Thus, the signal detection threshold for SLE detector in the presence of white noise is nearly one and in the presence of PU signal, the value of test statistic for SLE is greater than one. However, the signal detection threshold for SLE detector in the presence of colored noise is much greater than one and in the presence of PU signal, the value of test statistic for SLE is greater than one (not much greater than one). Similarly, the signal detection threshold for CAV detector in the presence of white noise is less than one and in the presence of PU signal, the value of test statistic for CAV is greater than one. However, the signal detection threshold for CAV detector in the presence of colored noise is much greater than one and in the presence of PU signal, the value of test statistic for CAV is greater than one (not much greater than one). Hence SLE and CAV method perform well in the white noise, but fail to detect

signal in the presence of colored noise.

The absolute difference between simulation threshold and derived threshold for  $L_s=J=10$  and  $M_s=1000$  given in (3.59), (3.61), (3.66), and (3.68) are  $2.6 \times 10^{-3}$ ,  $8 \times 10^{-3}$ ,  $3.5 \times 10^{-3}$ , and  $1.4 \times 10^{-4}$ , respectively. Hence, the above differences validate the theoretical calculation of thresholds for the proposed metrics. In terms of computational complexity, the CAV requires  $\mathcal{O}(M_s L_s^2)$  computation, FMD requires  $\mathcal{O}((M_s + 1)L_s^2)$  computation, where SLE, ME, FTM, MME, EME, SCN, MECN and the proposed metrics or algorithms require  $\mathcal{O}(M_s L_s^2 + L_s^3)$  computation. However, since  $L_s \ll M_s$ , hence the computational complexity of the proposed algorithms is slightly higher ( $\approx 5\%$ ) than FMD, albeit with LDRSCM performing far better than FMD in the presence of colored noise.

### 3.4 Summary

In this chapter, new method for SS in Grassmann manifold for cognitive radios is proposed. The proposed method performs well in detecting PU's signal and also provides significant improvement as compared to CAV, FTM, and 3EED. Simulation of distributions of proposed method agrees with the derived expression under both hypotheses. Experimental results demonstrate robustness and feasibility of proposed method for SS. Further, sensing time can be reduced by cooperative SS by making the proposed method feasible for real-time sensing.

Further a robust LDRSCM and ELDRSCM based SS are proposed for CR under low SNR. Simulation results demonstrate robustness of the proposed metrics on DTV signal captured at different location for both white and colored noise, as compared to existing algorithms in the presence of colored noise.

## Chapter 4

# Non-Parametric Maximum

# Likelihood based Viterbi Decoder

In a communication system, when there is no interference and additive noise is assumed to be Gaussian distributed, the LS based channel estimation is optimal [87]. Additionally, the Hamming distance for the binary symmetric channel (BSC) and the Euclidean distance for the continuous-output channel based Viterbi decoder gives ML performance in the presence of AWGN [88]. However, in the presence of interference, the LS based channel estimator and Euclidean distance based Viterbi decoder are no longer optimal [89]. In case of high interference, there are various techniques such as NPML [32], MCC [40], and robust adaptive algorithm (RAA) [90] based estimators that perform better than LS based channel estimator. The BER performance of MCC and RAA is comparable to the LS estimator, for the preamble with small number of samples. However, as MCC and RAA are adaptive algorithms, they require large number of iterations to converge. Hence, to overcome large number of iterations and to improve BER performance, NPML based channel estimation is chosen. Since NPML converges much faster than MCC and RAA, and is thus suitable for use with a small number of subcarriers as in IEEE 802.11ah.

The log-likelihood function of the conventional Viterbi decoder is based on the Euclidean distance between the received signal and transmitted signal. However, in

the presence of non-Gaussian noise, the received signal after equalization follows a non-Gaussian distribution, and hence the performance of Euclidean distance based branch metric for Viterbi decoder degrades. Thus, the calculation of branch metric based on the PDF of the residual error for the Viterbi decoder in the presence of non-Gaussian noise is proposed. The proposed Viterbi decoder gives better BER performance as compared to the conventional algorithms as demonstrated in results and analysis section. Since no *a priori* knowledge of type of interferers is assumed, the proposed algorithm is generic and suitable for any type of interference.

In this chapter, non-parametric maximum likelihood based Viterbi decoder for OFDM system in the presence of interference is discussed followed by simulation and experimental results.

## 4.1 OFDM based Receiver in Interference Limited Environments

In this section, system model for OFDM system and overview of NPML are discussed. The proposed receiver based on non-parametric maximum likelihood channel estimation followed by Viterbi decoder is discussed. The Viterbi decoder's branch metric is updated based on the distribution of residual error. The proposed receiver structure is tested on IEEE 802.11ah based receiver in two different type of additive interference: 1) IEEE 802.15.4 device, and 2) impulsive noise. Both simulations and real-world experimental results on standard compliant platform show that the proposed algorithm performs better in terms of BER than other receivers in all the considered interference models. Additionally, analytical expression for the probability of symbol error is derived.

### 4.1.1 System Model

Block diagram of generic OFDM based transceiver is shown in Fig. 4.1. The binary data source,  $s(n)$ , is channel encoded with FEC codes. This encoded data is repre-

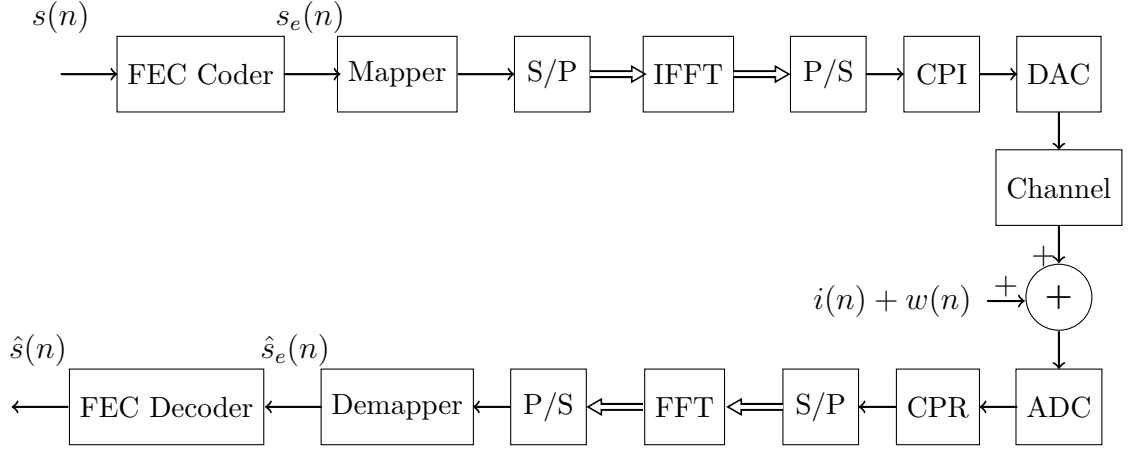


Figure 4.1: Block diagram of OFDM based transceiver.

sented by,  $s_e(n)$ . The discrete frequency domain modulated sample at  $k_c^{th}$  subcarrier after serial-to-parallel conversion is given by  $X(k_c)$ . After performing IFFT on a block of  $N$  symbols of  $X(k_c)$ , the discrete time domain samples are given by:

$$x(n) = \frac{1}{N} \sum_{k_c=0}^{N-1} X(k_c) \exp\left(\frac{j2\pi k_c n}{N}\right) \quad n = 0, \dots, N-1 \quad (4.1)$$

After IFFT and parallel-to-serial conversion, CP is inserted and then converted into analog signal by using a DAC and transmitted over the RF link. At the receiver, the received signal in the discrete time domain can be represented as:

$$y(n) = \sum_{l=0}^{L-1} h(l)x(n-l) + i(n) + w(n) \quad (4.2)$$

where  $\mathbf{h} = [h(0), h(1), \dots, h(L-1)]$  represent the fading CIR coefficients vector of dimension  $L \times 1$ ,  $i$  and  $w$  represent the discrete time domain samples of interference and AWGN, respectively. After removing CP followed by FFT on  $\mathbf{y}$  (where  $\mathbf{y}$  is the received signal vector of dimension  $N \times 1$ ), the discrete frequency domain sample at the  $k_c^{th}$  subcarrier is given by:

$$Y(k_c) = \sum_{n=0}^{N-1} y(n) \exp\left(-\frac{j2\pi k_c n}{N}\right) \quad K = 0, \dots, N-1 \quad (4.3)$$

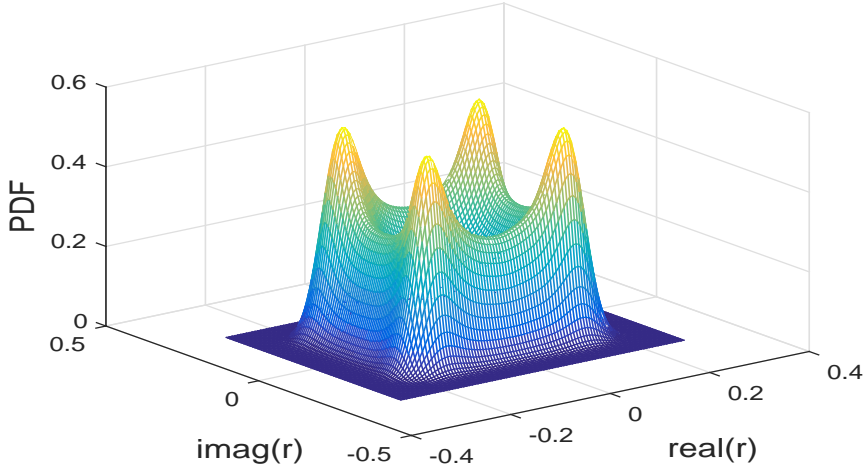


Figure 4.2: PDF of non-Gaussian noise process.

without loss of generality, the received frequency domain samples at  $k_c^{th}$  subcarrier can also be written as:

$$Y(k_c) = H(k_c)X(k_c) + I(k_c) + W(k_c) \quad (4.4)$$

where  $H$ ,  $I$  and  $W$  represents the Fourier transform of  $\mathbf{h}$ ,  $\mathbf{i}$  and  $\mathbf{w}$ , respectively.

In the LS based frequency domain channel estimator, the receiver knows *a priori* consecutive samples of  $X(k_c)$  referred to as preamble, and with the help of this preamble the estimated channel coefficients in the frequency domain is given by:

$$\hat{H}(k_c) = \frac{Y(k_c)}{X(k_c)} \quad (4.5)$$

The LS solution is optimal when there is no interference for the desired user [87]. However, when interference is present the overall mixture noise ( $v(n) = i(n) + w(n)$ ) is no longer Gaussian distributed as shown in Fig. 4.2, and hence the performance of LS based channel estimator degrades.

#### 4.1.2 Overview of NPML

In the case of non-Gaussian noise process, the NPML based channel estimation performs better as compared to LS based channel estimation [32]. The detail description

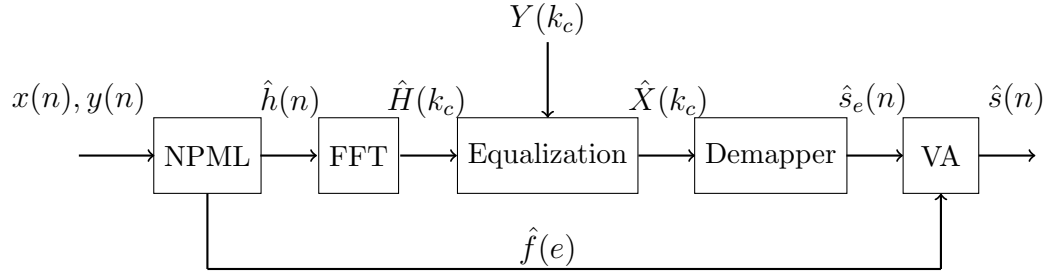


Figure 4.3: Proposed OFDM based receiver structure.

of NPML technique is given in Section 2.2.1.

The update equation of channel coefficients [32] at  $k^{th}$  iteration is given by:

$$\hat{\mathbf{h}}_k = \hat{\mathbf{h}}_{k-1} + \mu \nabla_{\hat{\mathbf{h}}_{k-1}} \mathcal{J}(\hat{\mathbf{h}}_{k-1}) \quad (4.6)$$

Hence, with the help of above equation the channel is iteratively estimated.

### 4.1.3 Proposed Receiver Structure

The proposed OFDM based receiver structure in interference affected environment is shown in Fig. 4.3. The branch metric calculation of the proposed Viterbi decoder is based on the PDF of the residual error. The residual error can be calculated with the help of equalized received signal and transmitted signal. Since, NPML technique is used for channel estimation in the presence of non-Gaussian noise; it gives channel estimates, residual error, and PDF of the residual error as the outcome. Thus, NPML based channel estimation is chosen. The proposed decoder works as follow: First, the joint PDF of additive interference and Gaussian noise is modeled and estimated as a non-Gaussian process with the help of kernel density estimation [46]. Then with the help of this estimated PDF of the non-Gaussian noise process and use of NPML technique the CIR is estimated [32]. After CIR estimation, the ML equalization is performed on the received data. Then with the help of estimated PDF of the residual error, the transition probability for the soft Viterbi decoder is calculated. Finally, the branch metrics are calculated with the help of transition probability, which is used in the Viterbi algorithm to decode the data. The NPML

algorithm is used for CIR estimation over the known preamble. The legacy long training field (L-LTF) of IEEE 802.11ah is used for CIR estimation which consists of 53 subcarriers (including the value 0 at DC), and BPSK modulated for 2 MHz bandwidth. In this work, NPML is used for CIR estimation on L-LTF.

### Branch Metric Calculation

In the conventional Viterbi decoder, the branch metric is calculated as [88]:

$$B(Y(k_c)|X(k_c)) = \log p(Y(k_c)|X(k_c)) = -\frac{\tilde{E}_s}{N_0}(Y(k_c) - X(k_c))^2 + \frac{N}{2} \log \frac{\tilde{E}_s}{\pi N_0} \quad (4.7)$$

where  $p(Y(k_c)|X(k_c))$  is the conditional PDF of the received symbol  $Y(k_c)$  given the transmitted symbol  $X(k_c)$  at  $k_c^{th}$  subcarrier,  $\tilde{E}_s$  represents symbol energy, and  $N_0$  represents noise power spectral density.

In the proposed decoder, the branch metric is calculated as:

$$B(Y(k_c)|X(k_c)) = \log \frac{1}{\sqrt{2\pi\sigma_k^2}N} \sum_{J=1}^N \exp\left(\frac{-(E(K) - E(J))^2}{2\sigma_k^2}\right) \quad (4.8)$$

where  $E$  is the FFT of the residual error.

### Probability of Symbol Error

After taking the FFT of  $\hat{\mathbf{h}}$  and  $\mathbf{y}$ , the ML equalization (assume that the transmitted signals are equiprobable) of  $Y(k_c)$  is given by:

$$\hat{X}(k_c) = \arg \max_{X \in C} [\hat{f}(Y(k_c)|\hat{H}(k_c))] \quad (4.9)$$

where  $C$  is the constellation of the transmitted signal.

The average probability of symbol error for BPSK modulated data in AWGN channel is given as:

$$P_e = \frac{1}{2N} \sum_{j=1}^N \frac{1}{2} \operatorname{erfc}\left(\frac{\sqrt{\tilde{E}_s} - E_R(j)}{\sqrt{2\sigma_k^2}}\right) + \frac{1}{2N} \sum_{j=1}^N \frac{1}{2} \operatorname{erfc}\left(\frac{\sqrt{\tilde{E}_s} + E_R(j)}{\sqrt{2\sigma_k^2}}\right) \quad (4.10)$$

Proof of the above equation is given in Appendix H.

Similarly the probability of error for QPSK modulated data in AWGN channel is given as:

$$\begin{aligned}
P_e = & \frac{1}{2N} \sum_{j=1}^N \frac{1}{2} \operatorname{erfc} \left( \frac{\sqrt{\tilde{E}_s/2 + E_R(j)}}{\sqrt{2\sigma_k^2}} \right) + \frac{1}{2N} \sum_{j=1}^N \frac{1}{2} \operatorname{erfc} \left( \frac{\sqrt{\tilde{E}_s/2 - E_R(j)}}{\sqrt{2\sigma_k^2}} \right) \\
& + \frac{1}{2N} \sum_{j=1}^N \frac{1}{2} \operatorname{erfc} \left( \frac{\sqrt{\tilde{E}_s/2 + E_I(j)}}{\sqrt{2\sigma_k^2}} \right) + \frac{1}{2N} \sum_{j=1}^N \frac{1}{2} \operatorname{erfc} \left( \frac{\sqrt{\tilde{E}_s/2 - E_I(j)}}{\sqrt{2\sigma_k^2}} \right)
\end{aligned} \tag{4.11}$$

Proof of the above equation is given in Appendix I.

#### 4.1.4 Results and Discussion

Performance of the proposed receiver structure for the physical layer of IEEE 802.11ah standard is compared with the conventional algorithms in the presence of interference. IEEE 802.11ah is an emerging standard for IoT application operating at sub-1-GHz license-exempt bands and is based on OFDM [12]. There are various challenges for the deployment of IEEE 802.11ah [13], and in this section, high interference in an outdoor deployment of IEEE 802.11ah is addressed.

Table 4.1: Simulation parameters

PARAMETERS	SPECIFICATIONS
FFT size	64 ( $32\mu s$ )
No. of data subcarriers	52
No. of pilot subcarriers	4
No. of null subcarriers	8
Cyclic prefix (CP)	$16 (8\mu s)/8 (4\mu s)$
Channel bandwidth	2 MHz
Modulation scheme	BPSK, QPSK
Channel	Frequency selective with 5 and 10 taps
Channel coding	Convolution codes (1/2)

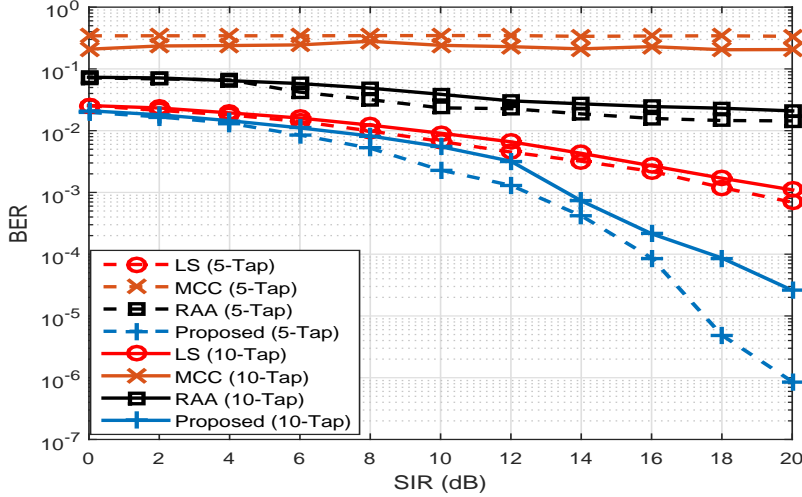


Figure 4.4: BER vs SIR at 30 dB SNR for IEEE 802.15.4 device as an interferer for BPSK modulated data with CP of length 8.

## Simulation Results

The simulation parameters are detailed in Table 4.1. Two different interference models are considered in this work as: 1) IEEE 802.15.4 device, and 2) impulsive noise (SaS) generated with  $\alpha = 1$  and  $\gamma = 0.1$ . Both IEEE 802.11ah and IEEE 802.15.4 are operating in the same band [12]. The IEEE 802.15.4 standard is designed for low rate wireless personal area network with various PHY modes. BPSK PHY is considered which is direct sequence spread spectrum based approach employing BPSK modulation and operating at 915 MHz with 40 kbps data rate [91]. From IEEE 802.11ah specifications, for the proposed receiver,  $N=64$  samples is used for PDF estimation of the residual error. By using kernel density estimation, the channel is estimated for  $\mu = 0.0005$ . To evaluate the BER performance of IEEE 802.11ah for CP of length 8 and 16, two channel model is chosen which gives channel length equal to 5-tap and 10-tap. The 5-tap channel model is generated by sampling the ITU-VB at 2 MHz, and 10-tap channel model is generated by sampling the COST-207 TU channel model at 2 MHz. These two channel models specify power delay profile of urban environment of sub-1 GHz band. All the simulations are ensembled over 200-runs.

Fig. 4.4 demonstrates the BER vs SIR at fixed 30 dB SNR for IEEE 802.15.4

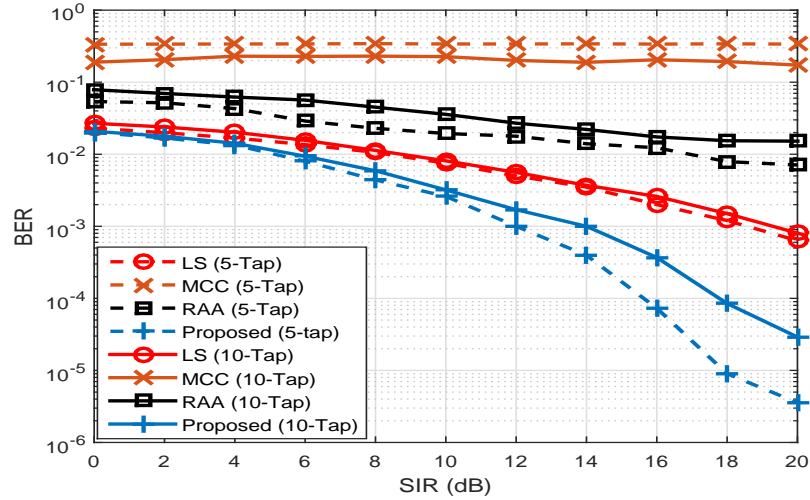


Figure 4.5: BER vs SIR at 30 dB SNR for IEEE 802.15.4 device as an interferer for BPSK modulated data with CP of length 16.

device as an interferer for BPSK modulated data with CP of length 8. Fig. 4.4 shows that the proposed receiver provides 6 dB gain at  $\text{BER} = 10^{-3}$  for 5-tap and 10-tap channel lengths, respectively as compared to LS algorithm. It is also observed from Fig. 4.4 that the performance of MCC and RAA is poor since both the MCC and RAA require large number ( $> 500$ ) of training samples for convergence, however the IEEE 802.11ah standard mandates only 64 samples for CIR estimation [13]. As observed, the BER for the 5-tap channel is lower as compared to BER for the 10-tap channel. This is because, as the channel length increases, the estimation error of the true CIR also increases which leads to high BER.

Fig. 4.5 shows the BER vs SIR at 30 dB SNR for IEEE 802.15.4 transmitter as an interferer for BPSK modulated data with CP of length 16. Again at BER of  $10^{-3}$  the proposed receiver provides 9 dB and 6 dB gain for 5-tap and 10-tap channel, respectively as compared to LS algorithm. Fig. 4.6 and Fig. 4.7 show the BER vs geometric SIR (GSIR) [92] at 30 dB SNR for impulsive noise as an interferer for BPSK modulated data with CP of length 8 and 16, respectively. It is again observed from Fig. 4.6 and Fig. 4.7 that the proposed receiver structure performs well in terms of BER as compared to the LS estimator. It is also observed from Fig. 4.6 that at high GSIR, the BER performance of both the proposed and

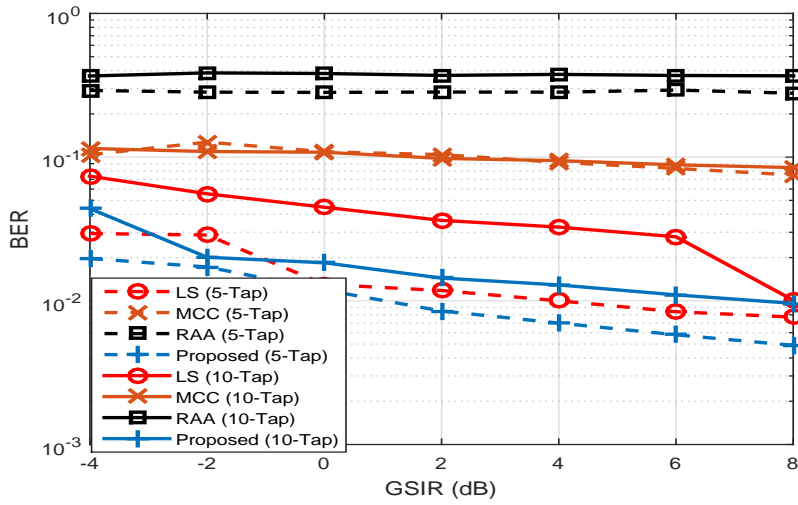


Figure 4.6: BER vs GSIR at 30 dB SNR for impulsive noise as an interferer for BPSK modulated data with CP of length 8.

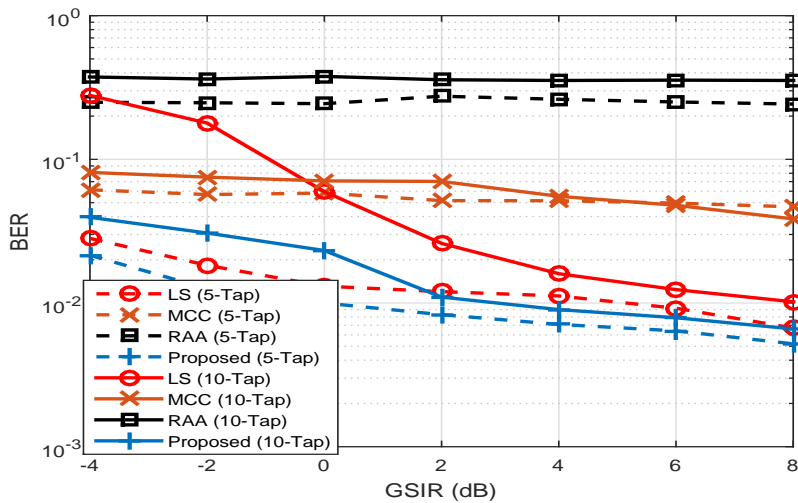


Figure 4.7: BER vs GSIR at 30 dB SNR for impulsive noise as an interferer for BPSK modulated data with CP of length 16.

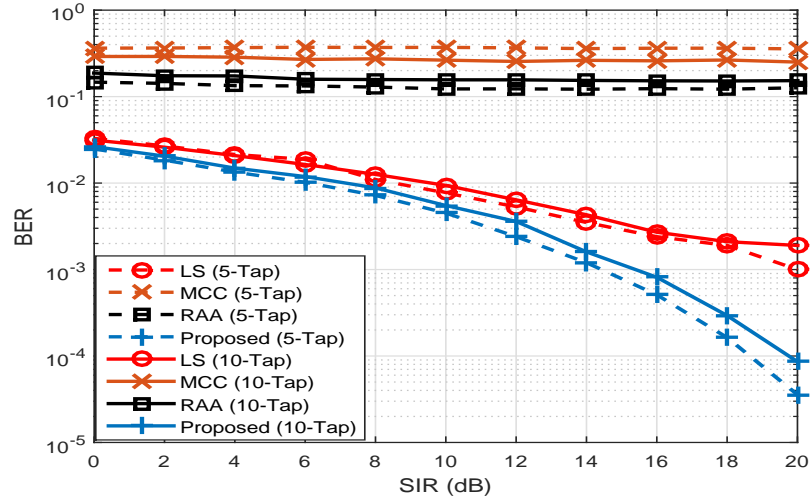


Figure 4.8: BER vs SIR at 30 dB SNR for IEEE 802.15.4 device as an interferer for QPSK modulated data with CP of length 8.

LS method is same. The reason for same BER performance of both the proposed and LS is because the residual error follows Gaussian distribution due to high GSIR for BPSK modulated data.

Fig. 4.8 shows the BER vs SIR at 30 dB SNR for IEEE 802.15.4 transmitter as an interferer for QPSK modulated data with CP of length 8. Fig. 4.8 shows that the proposed receiver provides 7 dB and 6.5 dB gain at  $BER = 2 \times 10^{-3}$  for 5-tap and 10-tap channel lengths, respectively as compared to LS algorithm. Fig. 4.9 shows the BER vs SIR at 30 dB SNR for IEEE 802.15.4 transmitter as an interferer for QPSK modulated data with CP of length 16 and it shows that the proposed receiver provides 3 dB and 5 dB gain at  $BER = 2 \times 10^{-3}$  for 5-tap and 10-tap channel lengths, respectively as compared to the LS algorithm. It is also observed from Fig. 4.8 and Fig. 4.9 that the BER performance of LS algorithm is better for CP of length 16 as compared to CP of length 8. Hence, the LS algorithm provides good BER performance at the cost of degraded spectral efficiency. On the other hand, the proposed receiver structure provides good BER performance and spectral efficiency.

Fig. 4.10 and Fig. 4.11 show the BER vs GSIR at 30 dB SNR for impulsive noise as an interferer for QPSK modulated data with CP of length 8 and 16, respectively.

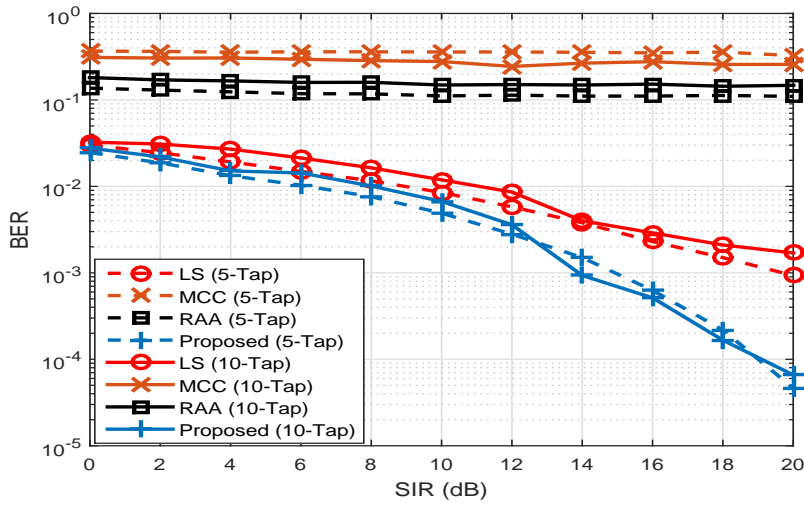


Figure 4.9: BER vs SIR at 30 dB SNR for IEEE 802.15.4 device as an interferer for QPSK modulated data with CP of length 16.

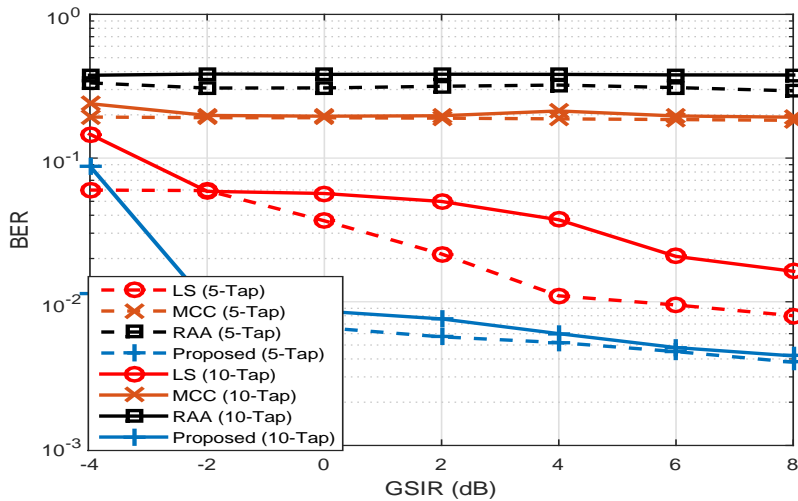


Figure 4.10: BER vs SIR at 30 dB SNR for impulsive noise as an interferer for QPSK modulated data with CP of length 8.

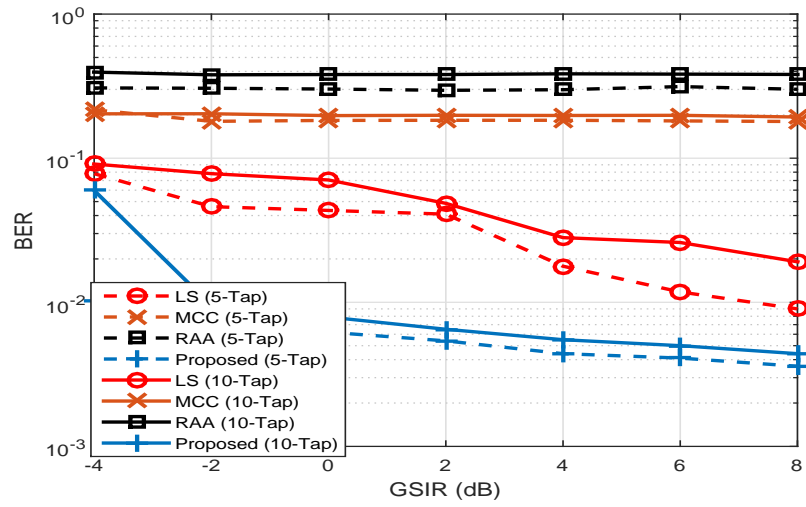


Figure 4.11: BER vs SIR at 30 dB SNR for impulsive noise as an interferer for QPSK modulated data with CP of length 16.



Figure 4.12: Experimental Setup.

It is observed from Fig. 4.10 and Fig. 4.11 that the proposed receiver structure outperforms the conventional algorithms in terms of BER.

#### 4.1.5 Experimental Results

The aim of this experiment is to show the feasibility and robustness of the proposed receiver structure in terms of BER as compared to existing algorithms. An experimental measurement station has been set up at Signal and Software Group research lab in IIT Indore as shown in Fig. 4.12 to evaluate over the air performance of physical layer of IEEE 802.11ah for BPSK and QPSK modulated data in the presence of interference generated by IEEE 802.15.4 standard. The set up consists of two desktops (having Intel(R) Xenon(R) CPU E5-1260 v3 @ 3.50 GHz processor with 64 GB RAM) which are connected to NI-USRP 2952R board through MXI-Express x4 cable and PCIe-8371 interface card. Amongst the two USRP 2952R boards, one USRP board is used as a transceiver which transmits and receives the signal at 915 MHz, and another board is used to generate IEEE 802.15.4 based interference signal at the same channel. The system parameters for experimental results are same as used in simulation results. Robustness and versatility of the proposed receiver is verified by practically generated IEEE 802.15.4 based interference. The results shown in Fig. 4.13 and Fig. 4.14 are ensembled over twenty trials. The proposed algorithm is implemented on LabVIEW CSDS 1.0 in conjunction with some functionality (NPML and Viterbi algorithm) implemented in MATLAB. The transceiver and interference USRP are 1.2m apart in line of sight. The antenna used for the experiment is VERT900 omnidirectional vertical antenna at 3 dBi gain.

Fig. 4.13 shows the BER vs SIR for IEEE 802.15.4 as an interferer for BPSK modulated data. From Fig. 4.13, it is observed that the proposed receiver structure provides 3.8 dB gain at  $\text{BER} = 2 \times 10^{-3}$  for CP of length 8 and 4 dB gain at  $\text{BER} = 2 \times 10^{-3}$  for CP of length 16 as compared to LS based receiver structure. It is also observed from Fig. 4.13 that the BER performance for CP of length 8 and CP of length 16 is same for the proposed receiver structure. Fig. 4.14 shows the BER

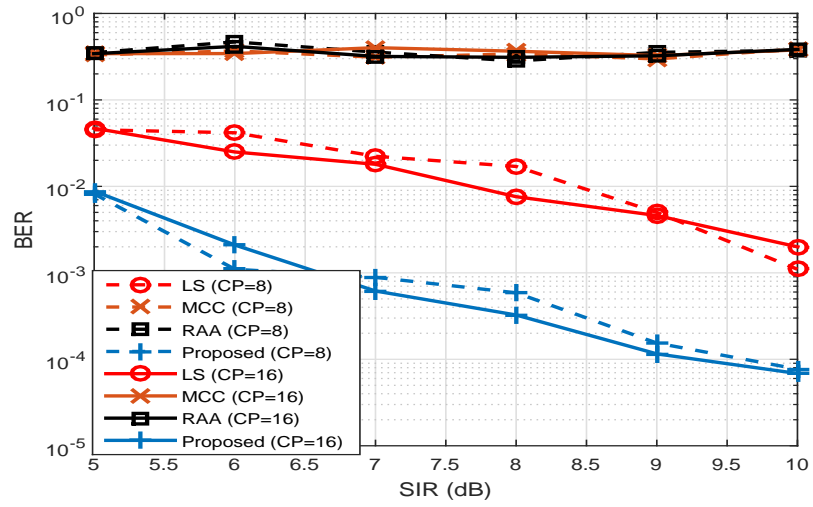


Figure 4.13: BER vs SIR at 30 dB SNR for IEEE 802.15.4 device as an interferer for BPSK modulated data.

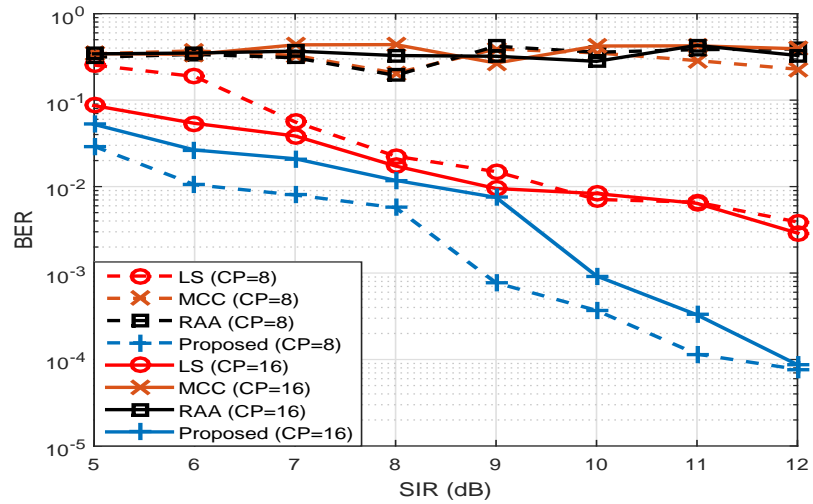


Figure 4.14: BER vs SIR at 30 dB SNR for IEEE 802.15.4 device as an interferer for QPSK modulated data.

vs SIR for IEEE 802.15.4 as an interferer for QPSK modulated data. It is observed from Fig. 4.14 that the proposed receiver structure provides 3.5 dB gain at  $\text{BER} = 4 \times 10^{-3}$  for CP of length 8 and 2.8 dB gain at  $\text{BER} = 4 \times 10^{-3}$  for CP of length 16 as compared to CP based receiver structure. It is also observed from Fig. 4.14 that the proposed method with CP of length 8 gives better performance than CP of length 16 at low CIR, while LS has the same performance for both the CP of length 8 and 16. Hence, it is inferred that the proposed receiver increases the spectral efficiency. Fig. 4.13 and Fig. 4.14 validate the simulation results which show robustness of the proposed receiver structure over other existing algorithms. Note that the difference in BER performance (achieving the same BER at different SIR) of experimental and their corresponding simulation results is due to different channel taps in experimental setup as compared to the channel taps considered in simulations, real transmission channel, non-linearities and other non-ideal characteristics of hardware components.

## 4.2 Summary

In this chapter, a robust generic OFDM based receiver structure in high interference environment is proposed. The proposed receiver uses NPML technique for channel estimation, and then the transition probability is calculated with the help of estimated PDF of residual error. This transition probability is used in the Viterbi algorithm for calculation of the branch metric and finally to decode the data. The simulation and experimental results validate robustness of the proposed receiver as compared to the conventional LS based receiver and other algorithms for the variety of interference limited environment.

# Chapter 5

## Implementation on Software

## Defined Radio and Field

## Programmable Gate Arrays

SDR technology brings the flexibility, cost efficiency and power to drive communications forward, where on the air performance of algorithms can be tested. There are various applications and algorithms like real-time SS using SDR [93], communication systems development using GNU Radio with USRP [94], IEEE 802.11a compatible OFDM receiver design based on a general purpose processor [95], LTE receiver framework using GNU radio [96] etc has been performed.

FPGA provide ease of validating algorithmic modifications and employ various reconfigurable processing elements such as complex programmable logic devices, memory based look-up-table (LUTs), and high-speed digital signal processing (DSPs) elements that are optimized for implementation of complex signal processing algorithms [97]. Hence several FPGA based algorithms and architectures implementation have been proposed in the literature. In [98], FPGA implementation of orthogonal matching pursuit for signal construction has been proposed. An FPGA implementation of direction of arrival estimation algorithm and a 2.48Gb/s FPGA-based quasi-cyclic low density parity check decoder have been proposed in [97] and

[99], respectively. In [97] and [99], algorithmic compiler of NI LabVIEW was used to translate the high level description of algorithms to very high speed integrated circuit hardware description language (VHDL) and further generated an optimized hardware implementation of algorithms. The algorithmic compiler also provides an exact usage of FPGA resources.

This chapter has been organized in two parts: In the first part, the performance of various blocks of physical layer of IEEE 802.22 standard is evaluated using USRP-2952R. In the second part, FPGA implementation of ITD algorithm on USRP-2952R is presented along with the utilization of FPGA's resource.

## **5.1 An IEEE 802.22 Transceiver and its Performance Analysis on Software Defined Radio**

In this section, an implementation framework for physical layer of IEEE 802.22 WRAN standard for normal mode is demonstrated and analyzed. This transceiver is implemented using the NI LabVIEW programming software on the NI-USRP 2952R. Different blocks of IEEE 802.22 based on their execution time are analyzed, and identify the critical blocks of IEEE 802.22 that should be optimized for real-time applications for commercial product development and field deployments. Further, the difference between theoretical and practical performance of the considered error control codes for IEEE 802.22 specified block size are also highlighted.

### **5.1.1 IEEE 802.22 Transceiver Implementation and Algorithms**

#### **IEEE 802.22 Implementation**

The IEEE 802.22 transceiver is implemented on LabVIEW CSDS in conjunction with some functionality implemented in MATLAB. Downlink with "normal" mode of operation is considered. The data transmission is in the form of Superframe

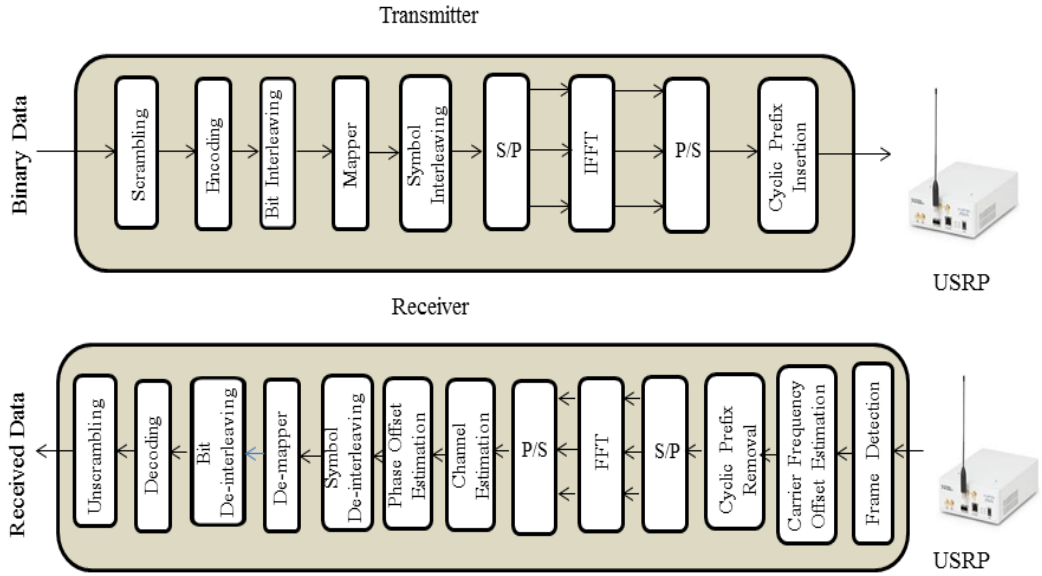


Figure 5.1: Block diagram of IEEE 802.22 transceiver

of 160 ms and each Superframe consists of frame with 10 ms. The first frame of each Superframe consists of Superframe preamble, frame preamble, SCH and then frame payload as per specification [6]. In this part, single frame transmission which consists of 26 OFDM symbols for CP of 1/4 and 6 MHz bandwidth is considered. The SCH is QPSK modulated with coding rate of 1/2 and four repetitions. The remaining 23 OFDM symbols are frame payload. The block diagram of IEEE 802.22 transceiver is shown in Fig. 5.1.

At the transmitter, the physical layer of IEEE 802.22 as given in Fig. 5.1 under “Transmitter” is implemented on Host-PC where the frame payload is scrambled for each data OFDM symbol. After that the scrambled bits are encoded by either CC or LDPC with 1/2 code rate. The encoded bits are interleaved and mapped to either QPSK or 16-QAM, or 64-QAM. The mapped symbols are again interleaved and perform OFDM modulation with the FFT size of 2048 and CP of 1/4. The Host-PC transmits the baseband I/Q signal to the USRP through MXI-Express x4 cable and PCIe-8371 interface card. The digital upconverter in the USRP interpolates the I/Q signal to 400 MS/s, and then converted into analog signal using DAC with 16 bit resolution. Finally, the mixer upconverts the signal to 460 MHz for transmission

from antenna. The data block size for CC is 1920 bits and the dimension of parity check matrix for LDPC is  $1152 \times 2304$ .

At the receiver, the USRP receives analog signal at 460 MHz from antenna. The mixers downconverts the signal into baseband I/Q signals. These I/Q signals are digitized by ADC with 14 bit resolution and then the digital downconverter decimates the signal at 6 MS/s. The downconverted signal is passed to the Host-PC through MXI-Express x4 cable and PCIe-8371 interface card. The physical layer of IEEE 802.22 as given in Fig. 5.1 under “Receiver” is implemented on Host-PC where the frame detection is performed using STS. After frame detection, CFO estimation is performed using LTS. Then the OFDM demodulation including CP removal is performed on the CFO compensated data and then the data is equalized with the help of estimated channel (channel is estimated with the help of LTS preamble). There is a sudden jump of phase between consecutive OFDM symbols after removing null subcarriers [100]. Thus, phase estimation is performed on the basis of pilot tones in each OFDM symbol. Then symbol de-interleaving and de-mapping is performed on the phase compensated data, and finally the bits are recovered after bit de-interleaving, channel decoding and unscrambling. Hard-decision Viterbi decoder [101] is used for CC and simple bit-flipping decoding (ten iterations) [102] is used for LDPC.

## Algorithms

In this section, the algorithms used for frame detection, CFO estimation, channel estimation, and phase estimation which are implemented in NI-LabVIEW are discussed.

- **Frame Detection**

Let  $x_s(n)$  and  $y(n)$  be the STS and received samples without removing CP, respectively. Then the frame can be detected by calculating the maximum cross correlation

of  $x_s(n)$  and  $y(n)$  given (in [103]) as:

$$z = \max_d \sum_{n=1}^{L_{cp}} x_s^*(n)y(n+d) \quad d = 0, 1, \dots \quad (5.1)$$

where  $L_{cp}$  denotes the CP length. The value of  $d$  for which the above equation gives first maximum value identifies starting of the frame.

- **Carrier Frequency Offset Estimation**

CFO estimation is performed by using two identical pattern of time-domain LTS after removing CP. Let  $y_l(n)$  be the received time-domain LTS, then CFO,  $\hat{\epsilon}$  is calculated as [103]:

$$\hat{\epsilon} = \frac{1}{\pi N} \sum_{n=1}^{N/2} y_l^*(n)y_l(n+N/2) \quad (5.2)$$

where,  $N$  is the total number of subcarriers.

- **Channel Estimation**

The channel estimation is performed in frequency-domain by using the LTS. Let  $X_l(k_c)$  and  $Y_l(k_c)$  be the frequency-domain transmit and receive LTS, respectively. Then, the least square channel estimation is given as:

$$\hat{H}(k_c) = \frac{Y_l(k_c)}{X_l(k_c)} \quad (5.3)$$

Linear interpolation is used to estimate the channel for zero value in LTS.

- **Phase Estimation**

There is a sudden jump of phase between consecutive OFDM symbols after removing null subcarriers. Thus, this phase jump is to be estimated and compensated for it. The phase estimation is based on the pilot subcarriers in each OFDM symbols. The phase  $\beta_m$  at  $m^{th}$  OFDM symbol can be estimated as [100]:

$$\alpha_m = \angle \left( \sum_K X_m(P)\hat{Y}_m(P) \right) \quad (5.4)$$

$$\beta_m = 2\alpha_m + \alpha_{m-1} \quad (5.5)$$

where  $X_m(P)$  represents the transmitted pilot symbol at  $m^{th}$  OFDM symbol, and  $\hat{Y}_m(P)$  represents the received pilot symbol at  $m^{th}$  OFDM symbol after channel estimation and compensation.

## 5.1.2 Results and Discussion

### Execution Time for Physical Layer of IEEE 802.22

In this subsection, the performance analysis of physical layer blocks of IEEE 802.22 is evaluated in terms of execution time for one OFDM symbol. The preamble data is BPSK modulated, whereas the frame payload is either QPSK or 16-QAM or 64-QAM modulated. The other system parameters are summarized in Table 5.1. Fig. 5.2 (a) shows the execution time of various blocks of IEEE 802.22. It is observed from Fig. 5.2 (a) that the CFO estimation consumes least processing time. OFDM modulation and demodulation including CP insertion and removal takes comparable processing time as CFO estimation for one OFDM symbol. Channel estimation and interleaver have same processing time which is higher than OFDM, but much lesser than frame detection. The frame detection requires maximum execution time and hence should be optimized first. The frame detection depends on the number of samples used for correlation. The execution time of frame detection given in Fig. 5.2 (a) is for 10,000 samples. The execution time of frame detection can be reduced by reducing the number of samples for correlation.

Fig. 5.2 (b), Fig. 5.3 (a) and Fig. 5.3 (b) show the execution time for encoding and decoding of one OFDM symbol for QPSK, 16-QAM and 64-QAM along with scrambling. Encoding, decoding, and scrambling for an OFDM symbol depends on the modulation technique used. Hence, as modulation order increases execution time of encoding, decoding, and scrambling increases. It is observed from Fig. 5.2 (b), Fig. 5.3 (a) and Fig. 5.3 (b) that the encoding of CC has least processing time because of 6 shift registers and 8 XOR-gates. Viterbi decoding has second least

Table 5.1: System configuration

PARAMETERS	VALUE
USRP	2952R
CPU	Intel(R) Xenon(R) CPU E5-1620 v3 @ 3.50 GHz
Transmission mode	SISO
Carrier frequency	460 MHz
Cyclic prefix (CP)	1/4
Channel bandwidth	6 MHz
Modulation scheme	QPSK, 16-QAM, 64-QAM
Channel estimation	Least Square estimation
Channel coding/decoding	Convolutional coding/Viterbi decoder, LDPC coding/simple bit-flipping decoding
Code rate	1/2

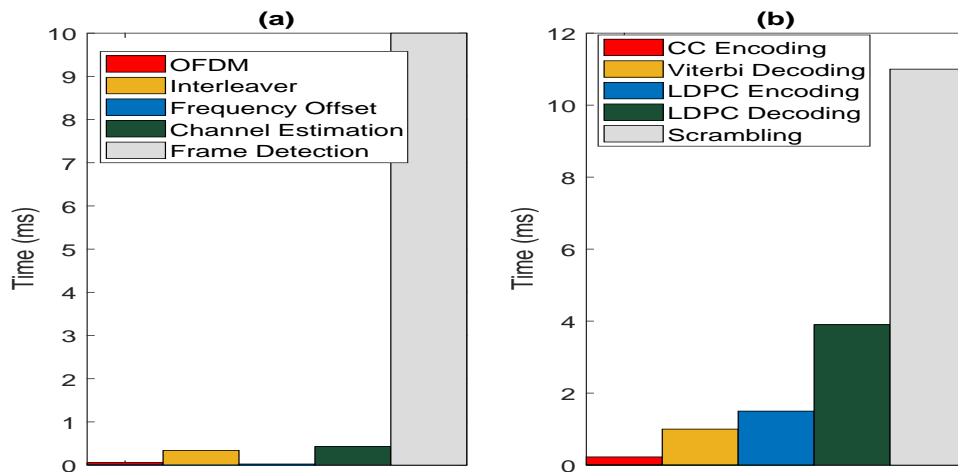


Figure 5.2: Execution time of (a) Various blocks of IEEE 802.22 and; (b) Comparison of different encoding and decoding technique for QPSK modulation with scrambling.

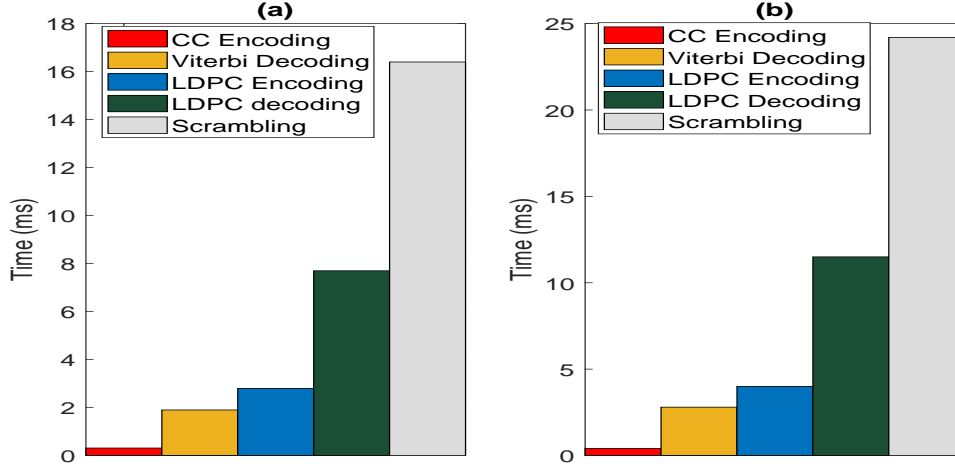


Figure 5.3: Execution time of (a) Comparison of different encoding and decoding technique for 16-QAM modulation with scrambling and; (b) Comparison of different encoding and decoding technique for 64-QAM modulation with scrambling.

execution time for all the considered modulation. Encoding time of LDPC code is slightly higher than the Viterbi decoder. However, the encoding time of LDPC codes can be reduced by using sparse nature of parity-check matrix. The decoding time of LDPC code is higher as compared to the encoding time of LDPC code. The execution time of LDPC codes can be reduced by using parallel decoding as used in Viterbi decoder. It is observed that, scrambling takes the maximum computational time. This also increases as the modulation order increases. Hence, the execution time for scrambling needs to be optimized for real time application.

### Experimental and Simulation Results for Physical Layer of IEEE 802.22

In this subsection, the performance of IEEE 802.22 standard is evaluated in terms of BER for CC and LDPC channel coding for QPSK, 16-QAM and 64-QAM modulation scheme. Since the implementation of IEEE 802.22 standard has not been sufficiently optimized, the transceiver cannot operate in real-time. Hence, an offline experiment is considered for evaluating the over-the-air performance of IEEE 802.22 standard shown as experimental results (represented as legend ‘Exp.’). The performance of CC and LDPC channel codes in computer without USRP known as simulation results (represented as legend ‘Sim.’) are also evaluated.

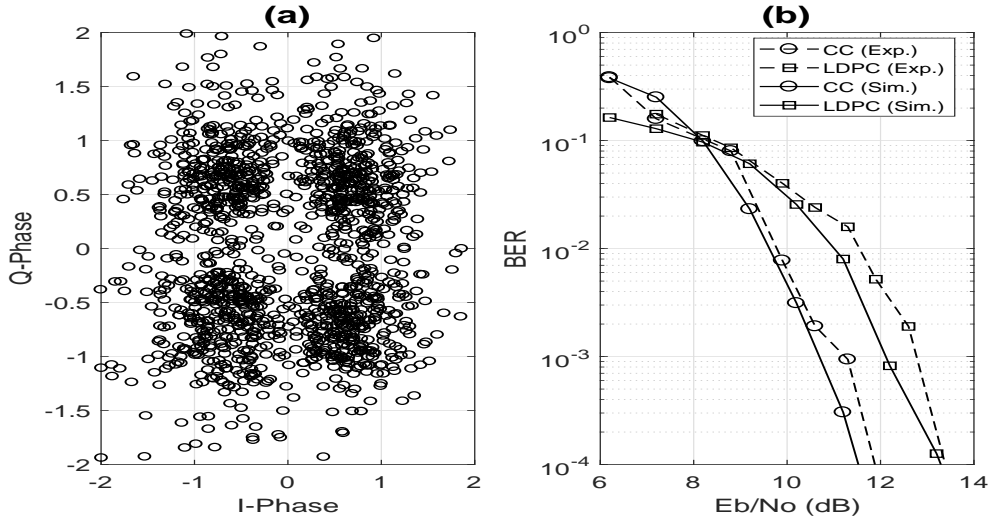


Figure 5.4: QPSK modulation: (a) Signal constellation diagram after channel equalization at 12 dB Eb/No and; (b) BER vs SNR for CC and LDPC

In the offline experiment, the transmitter section generates symbol for different combinations of channel coding and modulation scheme, which are then saved to a file. These symbols from the file are then sent to USRP for over-the-air transmission. The receiver USRP receives the signal, down-converts it and saves the received samples to a file for further processing by receiver section in the GPP. The received file contains a frame (26 OFDM symbols including preamble and SCH), the STS is used for frame detection and LTS is used for channel estimation. As the transmitter and receiver are static (assuming quasi-static), the channel is almost constant for a frame and hence the estimated channel is used for equalization for rest of the OFDM symbols. The simulation results are obtained for ensemble of 50-runs, while the experimental results are obtained for few runs. Thus, the curves for experimental results are not smooth.

Fig. 5.4 (a) shows the signal constellation diagram after channel equalization with QPSK modulation at 12 dB Eb/No for offline experiment. Fig. 5.4 (b) shows the BER vs SNR for CC and LDPC with QPSK modulation for both experimental and simulation results. Fig. 5.4 (b) shows that the CC gives better performance than LDPC. CC provides 1.5 dB gain over LDPC at  $10^{-4}$  BER for both experiment and simulation. The signal constellation diagram after channel equalization with 16-

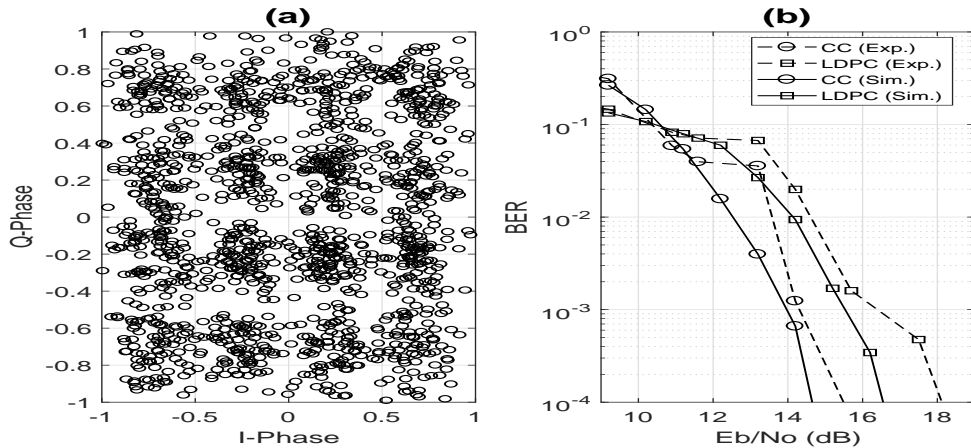


Figure 5.5: 16-QAM modulation: (a) Signal constellation diagram after channel equalization at 15.7 dB  $E_b/N_0$  and; (b) BER vs SNR for CC and LDPC

QAM modulation at 15.7 dB  $E_b/N_0$  for offline experiment is shown in Fig. 5.5 (a). Fig. 5.5 (b) shows the BER vs SNR for CC and LDPC with 16-QAM modulation and it shows that the CC outperforms the LDPC by 2.8 dB gain for experimental and 2.5 dB gain for simulation at  $10^{-4}$  BER.

Fig. 5.6 (a) shows the signal constellation diagram after channel equalization with 64-QAM modulation at 18.4 dB  $E_b/N_0$ . Fig. 5.6 (b) demonstrates the BER vs SNR for CC and LDPC with 64-QAM modulation and it shows that the CC gives better performance than LDPC. The CC gives 2.8 dB gain for experimental and 2.5 dB gain for simulation over LDPC at  $10^{-4}$  BER. *Both the experimental and simulation results show similar trend for BER curves and also show that the CC performs better than LDPC for the considered code rate and encoded data block size.* However, in future different data block size and code rate are also considered for observing the same BER trend or different. The simulation results represent lower bounds on experimental results. This is due to the real transmission channel, non-ideal and non-linear behaviour of some low-cost hardware components, finite precision arithmetic, and others [104].

The poor performance of LDPC than CC for all the considered modulation scheme is due to the fact, that the simple hard-decision based bit-flipping decoding algorithm for LDPC gives good performance at high SNR. However, there are decoding algorithms based on soft-decision like sum-product algorithm (SPA) which gives

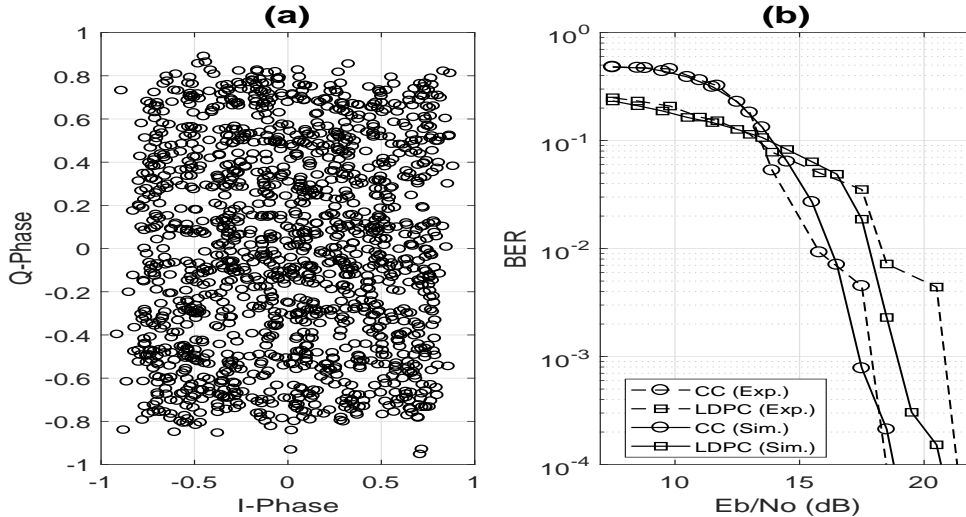


Figure 5.6: 64-QAM modulation: (a) Signal constellation diagram after channel equalization at 18.4 dB Eb/No and; (b) BER vs SNR for CC and LDPC

good performance at low SNR for LDPC. Furthermore, the computational complexity of soft-decision based algorithms are much higher than the hard-decision based algorithms. There is another way to increase the performance of LDPC at low SNR by increasing the coded block size or larger parity check matrix. However, this also increases the encoding and decoding complexity of LDPC and is not included in the latest IEEE 802.22 specification.

## 5.2 FPGA Implementation of Iterative Time-Domain Algorithm

In this section, an algorithmic compiler based FPGA implementation of ITD sparse channel estimation algorithm for IEEE 802.22 standard is presented. The algorithm is implemented on Xilinx Kintex-7 410T FPGA in the NI-USRP 2952R operating at 20 MHz by using high throughput math functions. The algorithmic compiler in the NI LabVIEW CSDS converts the high-level description of entire algorithm to very high speed integrated circuit hardware description language. Actual usage of FPGA's resource such as slices, lookup tables and others are also provided. Additionally, the BER performance of the considered algorithm for different modulation

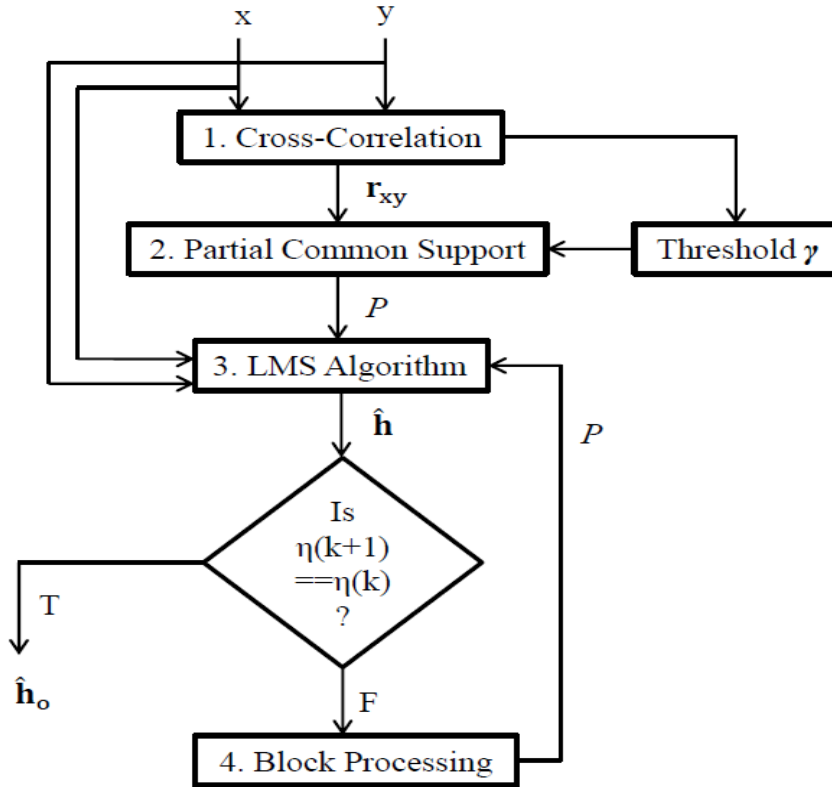


Figure 5.7: Flow chart of ITD algorithm

techniques obtained from MATLAB and FPGA implementations is compared.

### 5.2.1 FPGA Implementation

In this subsection, the ITD algorithm on Xilinx Kintex-7 410T FPGA in the NI-USRP 2952R by using algorithmic compiler of NI LabVIEW CSDS at 20 MHz clock rate is implemented. The ITD algorithm is implemented in NI LabVIEW CSDS (which is not a hardware description language). The algorithmic compiler of NI LabVIEW converts the high level description to VHDL description which is run on the FPGA in NI-USRP. Fig. 5.7 shows the flowchart of ITD algorithm. In the flowchart, cross-correlation and partial common support execute only at the beginning of the algorithm. The LMS algorithm and block processing are executed iteratively till the stopping criteria (line 4 of Algorithm 1 (given in Subsection 2.1.2)) is satisfied. The operation which is performed in block processing is given from line 10 to 12 of Algorithm 1. It is also observed from line 10 to 12 of Algorithm 1 that

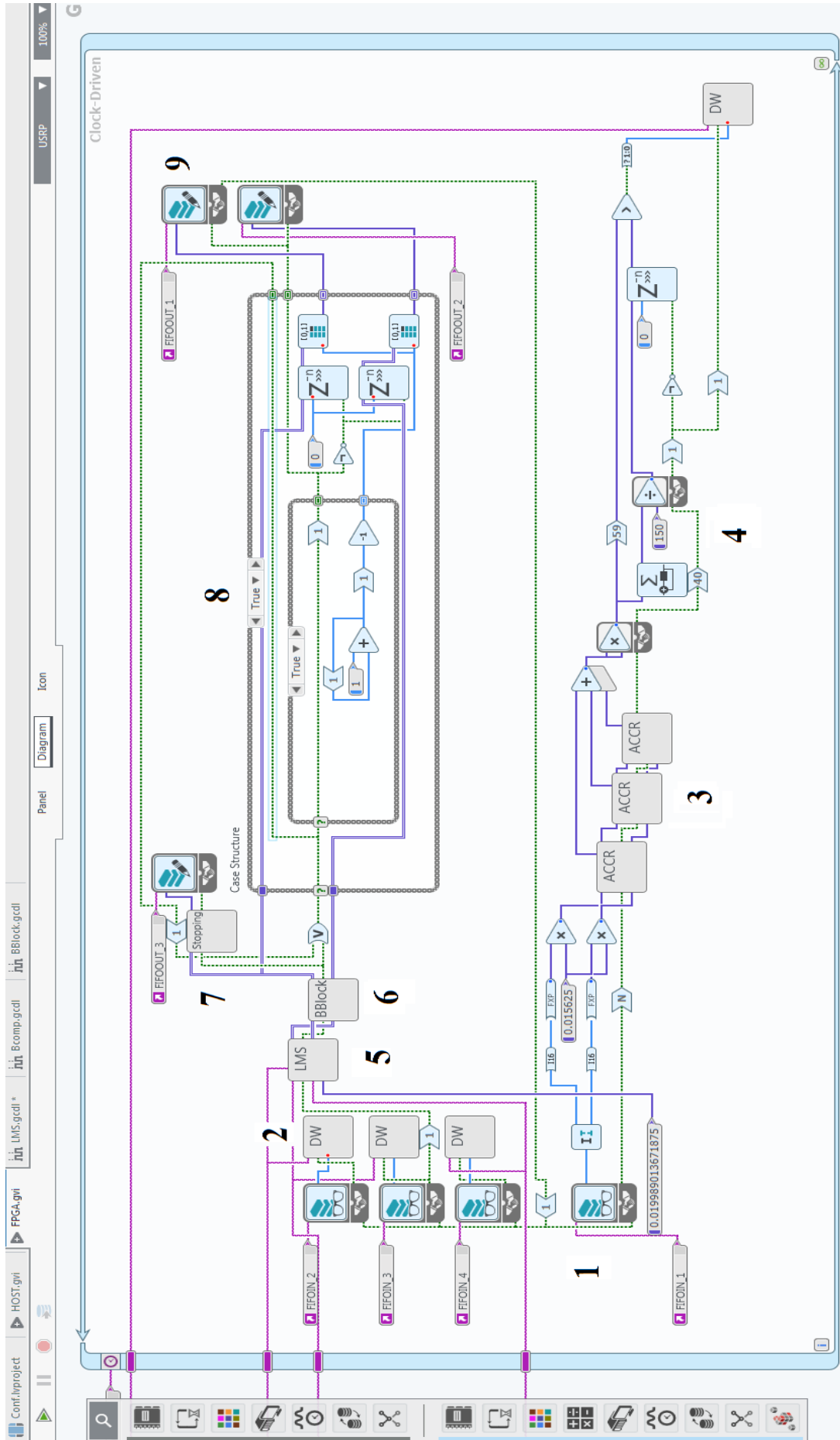


Figure 5.8: Top level Graphical Virtual Instrument of ITD algorithm using NI-LabVIEW CSDS on NI-USRP 2952R.

Table 5.2: Comparison of resource utilization of Xilinx Kintex-7 410T FPGA by cross-correlation of real value and complex value

Parameters	CC Real	CC Complex
Total slice (63,550)	6,778 (10.7%)	23,264 (36.7%)
LUT (2,54,200)	15,019 (5.9%)	35,398 (13.9%)
BRAMs (795)	8 (1%)	8 (1%)
DSPs (1,540)	150 (9.8%)	1,200 (78%)
Registers (5,08,400)	9,752 (1.9%)	33,242 (6.5%)

there is a possibility of parallel processing of each block.

Fig. 5.8 shows the top level Graphical Virtual Instrument (GVI) of ITD algorithm using NI-LabVIEW CSDS on NI-USRP 2952R. The high-level operation of the ITD algorithm is described in the following steps:

1. Serial data  $\mathbf{x}$  and  $\mathbf{y}$  is received from host to target using WRITE Direct Memory Access First In First Out (DMA-FIFO) in the host and READ FIFO in the target. In the proposed case, the host is PC and the target is Xilinx Kintex-7 FPGA in USRP-2952R. The data is fixed point number of 16 bit signed integer of format Q10.6 with 10 integer bits and 6 fractional bits.
2. Since the algorithm is iterative,  $\mathbf{x}$  and  $\mathbf{y}$  are required for each iteration and hence stored in the block random access memory (BRAM) of FPGA.
3. Cross-correlation of  $\mathbf{x}$  and  $\mathbf{y}$  is performed. To save the FPGA's resource, only real values of  $\mathbf{x}$  and  $\mathbf{y}$  for cross-correlation is proposed to use. Table I shows the comparison of resource utilization of Xilinx Kintex-7 410T FPGA by cross-correlation of real value and complex value. It is observed from Table 5.2 that huge amount of resource is saved specially DSPs.
4. Threshold  $\gamma$  is calculated and on the basis of this threshold initial active tap detection or partial common support  $P$  is calculated and stored in BRAM of FPGA.

5. The LMS algorithm is performed with the help of  $\mathbf{x}$ ,  $\mathbf{y}$  and  $P$  which are stored in the BRAM. To estimate the complex channel coefficients using FPGA, a finite impulse response (FIR) filter should be executed four times and also requires memory to store the output of each execution. This four times execution of an FIR filter increases the latency of the algorithm. To reduce the latency of the algorithm, parallel execution of four FIR filters as shown in Fig. 5.9 (a) is performed. However, this parallel processing increases the FPGA's resources.
6. Block processing is performed for line 10 to 12 of Algorithm 1. Each block consists of 7 consecutive channel coefficients. In this case, parallel execution of 6 blocks (ceil ratio of the total channel coefficients i.e 41 to the channel coefficients of each block i.e. 7) which reduces the latency of the algorithm as shown in Fig. 5.9 (b) is performed. Similar to the above this parallel execution leads to increase in the FPGA's resources.
7. If the stopping criterion as given in line 4 of the Algorithm 1 is satisfied, the algorithm terminates and the final sparse channel coefficients are obtained.
8. Since the output of 6<sup>th</sup> step is parallel and WRITE FIFO writes data serially to the host. Hence, parallel to serial conversion is required.
9. Send data back to Host serially by using WRITE FIFO in the target and READ DMA FIFO in the host.

## 5.2.2 Results and Discussion

In this subsection, the BER performance of ITD algorithm for sparse channel estimation obtained from MATLAB and FPGA at IEEE 802.22 standard based receiver is compared. The communication channel for IEEE 802.22 is sparse in nature [16]. The estimated channel coefficients obtained by MATLAB and FPGA are floating point and fixed point, respectively. The COST-207 TU channel is used which gives

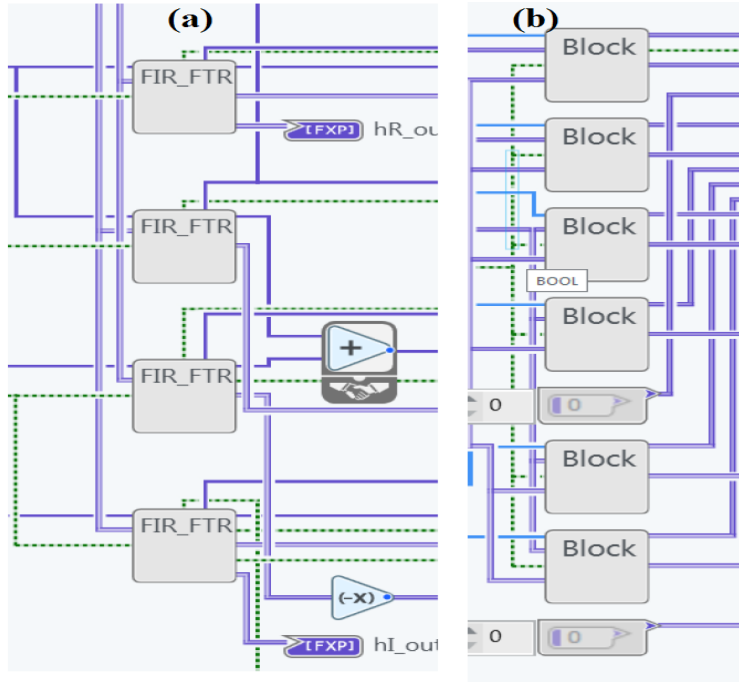


Figure 5.9: (a) Parallel FIR filter processing, and (b) Parallel block processing

Table 5.3: Simulation parameters

Parameters	Specifications
FFT size	2048 ( $256\mu s$ )
No. of data subcarriers	1440
No. of pilot subcarriers	240
No. of null subcarriers	368
Cyclic prefix (CP)	$1/32$ ( $8\mu s$ )
Channel bandwidth	7 MHz
Modulation scheme	QPSK, 16-QAM, 64-QAM
Channel	Frequency selective with 41 taps
Channel coding	Convolution codes ( $1/2$ )

6 active taps out of 41 taps at 8 MHz sampling rate [20]. The IEEE 802.22 standard is based on OFDM with 2048 FFT size. The first two OFDM symbols of super-frame of IEEE 802.22 consists of STS and LTS, respectively [20]. The STS is used for cross-correlation which is used to obtain partial common support and the LTS is used for channel estimation. The results are obtained over an ensemble of 20-runs with step-size for LMS algorithm equal to 0.02. The simulation parameters are given in Table 5.3.

Fig. 5.10, Fig. 5.11 and Fig. 5.12 show the BER vs SNR for QPSK, 16-QAM and 64-QAM modulation, respectively. It is observed from these three figures that the

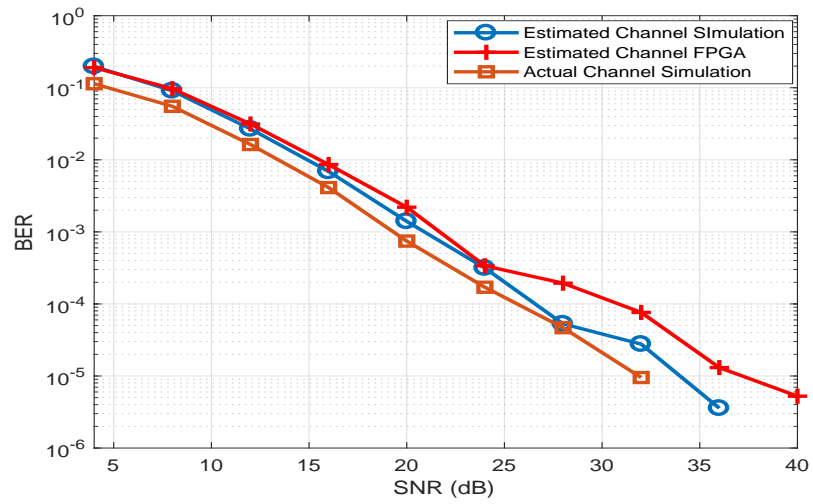


Figure 5.10: BER vs SNR for QPSK modulation

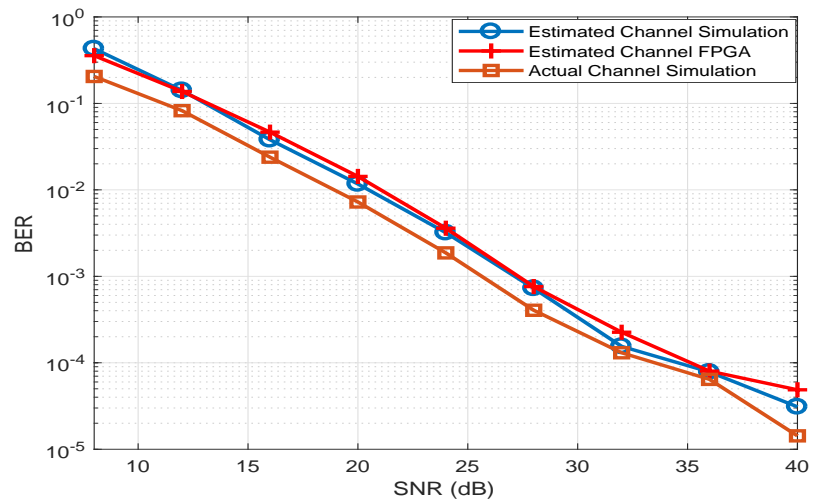


Figure 5.11: BER vs SNR for 16-QAM modulation

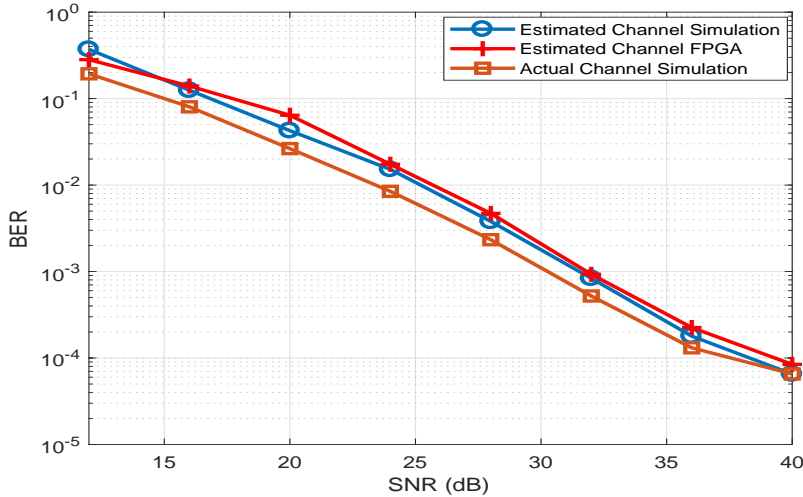


Figure 5.12: BER vs SNR for 64-QAM modulation

channel coefficients obtained from both floating point (MATLAB) and fixed point (FPGA) give same BER results. It is also observed from results that the cross-correlation using real values of signal on FPGA do not affect the BER performance because in MATLAB, the cross-correlation is performed on complex signal. Table 5.4 shows the comparison of resource utilization of Xilinx Kintex-7 410T FPGA by ITD algorithm with serial and parallel block processing. It is observed from Table 5.4 that ITD algorithm takes nearly same time to generate VHDL code with serial and parallel block processing. However, ITD with parallel block processing takes 1.5 times more total compilation time than ITD with serial block processing. The large compilation time of ITD algorithm with parallel block processing is due to large synthesizing, logic optimization and placing time of extra 5 blocks. Further ITD algorithm with serial and parallel block processing require same amount of BRAMs and Registers. Again due to the extra 5 blocks in ITD algorithm with parallel block processing the requirement of total slice, LUT and DSPs are 1.5, 1.5 and 2 times more than that of ITD algorithm with serial block processing.

Table 5.5 shows the clock cycle consumed by various stages of ITD algorithm with serial and parallel block processing. It is observed from Table 5.5 that except block processing stage, rest of the stages require same clock cycle for ITD algorithm with both serial and parallel block processing. In block processing stage, serial

Table 5.4: Comparison of resource utilization of Xilinx Kintex-7 410T FPGA by ITD algorithm with serial and parallel block processing

<b>Parameters</b>	<b>Serial BP</b>	<b>Parallel BP</b>
Clock rate (MHz)	20	20
Time to VHDL (sec)	23	32
Total compile (min)	53	80
Total slice (63,550)	20,775 (32.7%)	31,102 (48.9%)
LUT (2,54,200)	50,584 (19.9%)	74,588 (29.3%)
BRAMs (795)	21 (2.6%)	21 (2.6%)
DSPs (1,540)	418 (27%)	838 (54.4%)
Registers (5,08,400)	26,597 (5.2%)	37,541 (7.4%)

Table 5.5: Clock cycle consumed by various stages of ITD algorithm with serial and parallel block processing

<b>Stages</b>	<b>Serial BP</b>	<b>Parallel BP</b>
Cross-correlation	190	190
Partial common support	60	60
LMS	2596	2596
Block processing	210	35
Stopping	33	33

block processing requires 6 times more clock cycle because of extra blocks processing serially. Hence, the latency of ITD algorithm with serial block processing is higher than that of the parallel block. Since the last three stages of Table 5.5 execute more than one time and hence, the latency of ITD algorithm with serial block processing is much higher than that of parallel block processing.

It is concluded that huge amount of FPGA's resources are saved by taking cross-correlation of real values instead of complex values of  $\mathbf{x}$  and  $\mathbf{y}$ . These saved FPGA's resources can be used in parallel block processing which decreases the latency of the ITD algorithm.

### 5.3 Summary

In this chapter, the IEEE 802.22 standard is conceived for providing wireless access to rural areas on TVWS at VHF/UHF band. The signal processing framework for IEEE 802.22 standard based transceiver using the LabVIEW programming software is developed and evaluated over-the-air performance of IEEE 802.22 standard based system using NI-USRP 2952R. As contrary to the general observation, the CC performs better as compared to LDPC for all the modulation scheme at the considered code rate and coded data block size. However, the performance of LDPC can be improved by using large coded data block size or/and soft-decision based decoding algorithm.

Further, an algorithmic compiler based FPGA implementation of an ITD based algorithm for sparse channel estimation in the presence of Gaussian noise is presented. Only real values based cross-correlation is proposed instead of complex values which drastically reduces the FPGA's resources. Further, the saved FPGA's resources can be used in parallel block processing which reduces the overall latency of the ITD algorithm.

# Chapter 6

## Conclusion and Future Work

In this chapter, main contributions and insights of the work addressed in this thesis have been concluded. Further, scope for future work has been discussed.

### 6.1 Conclusion

In this thesis, an ITD algorithm for sparse channel estimation in the presence of Gaussian noise and its FPGA implementation using LabVIEW CSDS is proposed. Only real values based cross-correlation is proposed instead of complex values which drastically reduces the FPGA's resources. Further quadratic transformation based NG-NPML and ZA-NG-NPML adaptive algorithms for sparse channel estimation in the presence of non-Gaussian noise are proposed. Simulation results show robustness of the proposed method in terms of convergence rate and MSE floor. In addition, analytical expressions of MSE, and EMSE for the proposed adaptive algorithms are derived.

Further, Grassmann and LogDet based SS are proposed in the presence of white and colored Gaussian noise, respectively. Simulation results show that the proposed methods detect very low power PU's signal. The analytical expressions of threshold detection and probability of signal detection for the proposed algorithms are derived. Lower bound for the probability of detection of signal is also derived using separating function for Grassmann based SS. Further sensing time can be reduced by coopera-

tive SS by making the proposed method feasible for real-time sensing. Experimental verification on the SDR is also performed and it is found that the proposed method fulfills the requirement of maximum protection of the DTV signal.

A new OFDM based receiver structure operating in high interference environment is proposed. The proposed receiver is based on NPML channel estimation followed by Viterbi decoder. The Viterbi decoder's branch metric is updated based on the distribution of residual error. Both simulations and real-world experimental results on standard compliant platform show that the proposed algorithm performs better in terms of bit error rate than other receivers in all the considered interference models. Additionally, analytical expression for the probability of symbol error is also derived.

An implementation framework for physical layer of IEEE 802.22 WRAN standard is demonstrated and analyzed. This transceiver is implemented using NI-LabVIEW programming software on the NI-USRP 2952R. Different blocks of IEEE 802.22 based on their execution time are also analyzed, and identify the critical blocks of IEEE 802.22 that should be optimized for real-time applications.

## 6.2 Future work

In future, finding the separating function for the proposed SS methods which gives optimal bound for probability of signal detection, and the selection of optimum number of the secondary users and their locations for CSS can be explored. Impact of PU's duty cycle on SS will also analyzed.

Improvement in the proposed sparse channel estimation and proposed new algorithms for mmWave massive MIMO communication. Signal detection for multiple users for massive MIMO communication can also explored in future. Full-duplex communication can also be explored which double the spectral efficiency of communication system. Further, full-duplex with cognitive radio can also be explored which increases the spectral efficiency of secondary users.

# Appendix A

## Derivation of (2.12)

Let  $p_{tap}$  be the probability that the detected tap is an active tap,  $\Upsilon$  represents threshold,  $\sigma_{tap}^2$  is the variance of active channel taps, and  $\sigma_{ndtap}^2$  is the variance of non-active detected taps. The probability of detection of non-active taps above  $\Upsilon$  [105] is given as

$$P_D = p_{tap}(1 - e^{\frac{-\Upsilon^2}{2(\sigma_{ndtap}^2 + \sigma_{tap}^2)}}) + (1 - p_{tap})e^{\frac{-\Upsilon^2}{2\sigma_{ndtap}^2}} \quad (\text{A.1})$$

Differentiating  $P_D$  with respect to  $\Upsilon$ , to minimize the non-active taps detection which, gives optimum value of  $\Upsilon$  as:

$$\Upsilon_{opt} = \sigma_{ndtap} \sqrt{2 \frac{1+V}{V} \ln\left(\frac{1-p_{tap}}{p_{tap}}(1+V)\right)} \quad (\text{A.2})$$

where  $V = \sigma_{tap}^2/\sigma_{ndtap}^2$ . Let  $\bar{\Upsilon}_{opt,i}^2 = \lambda_{opt,i}^2/(2\sigma_{ndtap,i}^2)$  is the optimum value of  $\Upsilon$  at  $i^{th}$  iteration, then the power of active taps ( $P_{AT}$ ) and the power of non-active taps above  $\Upsilon$  ( $P_{NAT|\Upsilon}$ ) at  $i^{th}$  iteration will be given [106] as:

$$P_{AT} = \sigma_{tap}^2 \left(1 - \left(1 + \frac{\bar{\Upsilon}_{opt,i}^2}{1+V_i}\right) e^{-\frac{\bar{\Upsilon}_{opt,i}^2}{1+V_i}}\right) \quad (\text{A.3})$$

and

$$P_{NAT|\lambda} = \sigma_{ndtap,i}^2 (1 + \bar{\Upsilon}_{opt,i}^2) e^{-\bar{\Upsilon}_{opt,i}^2} \quad (\text{A.4})$$

where  $V$  at  $i^{th}$  iteration be given as  $V_i = \sigma_{tap}^2 / \sigma_{ndtap,i}^2$ . The following approximation for high  $V_i$  can be used and at convergence as:

$$\bar{\Upsilon}_{opt,i}^2 \approx \ln\left(\frac{1 - p_{tap}}{p_{tap}} V_i\right) \quad (\text{A.5})$$

$$P_{NAT|\lambda} \approx \sigma_{ndtap,i}^2 \left(1 + \ln\left(\frac{1 - p_{tap}}{p_{tap}} V_i\right)\right) \frac{p_{tap}}{(1 - p_{tap}) V_i} \quad (\text{A.6})$$

$$P_{AT} \approx \sigma_{tap}^2 \frac{\ln^2\left(\frac{1 - p_{tap}}{p_{tap}} V_i\right)}{2V_i^2} \quad (\text{A.7})$$

The variance of non-active detected taps at  $(i + 1)^{th}$  iteration can then be approximated as:

$$\sigma_{ndtap,i+1}^2 = p_{tap} P_{AT} + (1 - p_{tap}) P_{NAT|\Upsilon} \quad (\text{A.8})$$

After substituting (A.6) and (A.7) in (A.8), the above equation can be written as:

$$\sigma_{ndtap,i+1}^2 \approx \sigma_{ndtap,i}^2 (1 - p_{tap}) \quad (\text{A.9})$$

Hence,

$$\sigma_{ndtap,i}^2 = \sigma_{ndtap,0}^2 (1 - p_{tap})^i \quad (\text{A.10})$$

Now, the variance of taps ( $\sigma_{Dtap}^2$ ) detected at  $i^{th}$  iteration can be written as:

$$\sigma_{Dtap,i}^2 = \sigma_{tap}^2 + \sigma_{ndtap,i}^2 \quad (\text{A.11})$$

It is observed from (A.10) and (A.11) that,  $\sigma_{Dtap}^2$  decreases as iteration increases.

As  $h(n)$  is i.i.d., hence  $\sigma_{Dtap}^2$  is nearly equal to the mean of  $|h^D(n)|^2$  ( $h^D(n)$  is the detected channel coefficients). Therefore, mean of  $|h^D(n)|$  (equal to  $\tilde{h}$  step 15 in Algorithm 1) also decreases as iteration increases, which analytically proves the chosen threshold  $\tilde{h}$  as  $T_h$ .

# Appendix B

## Derivation of (2.28)

Case 1 ( $\hat{h}_k(l)r_{k+1}(l) > 0$ ): For the first case, after expanding (2.27) yields

$$D = \sum_{l=0}^{L-1} \left| \sqrt{A + \alpha_k |r_{k+1}(l)|} - 2B - \sqrt{A} \right|^2 \quad (\text{B.1})$$

where

$$A = \alpha_k \left( \left| |\hat{h}_k(l)| - |h_k(l)|^2 \right| + \beta \right) \quad (\text{B.2})$$

$$B = \alpha_k |\hat{h}_k(l)| |r_{k+1}(l)| \quad (\text{B.3})$$

and  $\alpha_k |r_{k+1}^2(l)|$  is neglected. The (B.1) can be written as:

$$D = \sum_{l=0}^{L-1} \left| \sqrt{A} \left( 1 + \frac{\alpha_k |r_{k+1}(l)| (1 - 2|\hat{h}_k(l)|)}{A} \right)^{1/2} - \sqrt{A} \right|^2 \quad (\text{B.4})$$

By using Taylor series expansion and keeping the significant terms, the above equation can be approximated as:

$$D \approx \sum_{l=0}^{L-1} \left| \sqrt{A} \left( 1 + \frac{\alpha_k |r_{k+1}(l)| (1 - 2|\hat{h}_k(l)|)}{2A} \right) - \sqrt{A} \right|^2 \quad (\text{B.5})$$

The above equation can be further simplified as:

$$D \approx \sum_{l=0}^{L-1} \frac{\alpha_k^2 r_{k+1}(l) r_{k+1}(l) (1 - 2|\hat{h}_k(l)|)^2}{4A} \quad (\text{B.6})$$

The above equation can be written as:

$$D \approx \frac{\mathbf{r}_{k+1}^T \alpha_k (\mathbf{I} - 2|\hat{\mathbf{H}}_k|)^2 \mathbf{r}_{k+1}}{4 \left( \left| |\hat{\mathbf{H}}_k| - |\hat{\mathbf{H}}_k|^2 \right| + \beta \mathbf{I} \right)} \quad (\text{B.7})$$

$|\hat{\mathbf{H}}_k|$  is given as:

$$|\hat{\mathbf{H}}_k| = \begin{bmatrix} |\hat{h}_k(0)| & 0 & \cdot & \cdot & 0 \\ 0 & |\hat{h}_k(1)| & \cdot & \cdot & 0 \\ \cdot & \cdot & \cdot & \cdot & \cdot \\ \cdot & \cdot & \cdot & \cdot & \cdot \\ 0 & 0 & \cdot & \cdot & |\hat{h}_k(L-1)| \end{bmatrix} \quad (\text{B.8})$$

By comparing (2.23) with (B.7), the Riemannian metric tensor given as:

$$\mathbf{G}_k = \frac{\alpha_k (\mathbf{I} - 2|\hat{\mathbf{H}}_k|)^2}{4 \left( \left| |\hat{\mathbf{H}}_k| - |\hat{\mathbf{H}}_k|^2 \right| + \beta \mathbf{I} \right)} \quad (\text{B.9})$$

Hence,

$$\mathbf{G}_k^{-1} = \frac{4 \left( \left| |\hat{\mathbf{H}}_k| - |\hat{\mathbf{H}}_k|^2 \right| + \beta \mathbf{I} \right)}{\alpha_k (\mathbf{I} - 2|\hat{\mathbf{H}}_k|)^2} \quad (\text{B.10})$$

The  $\beta$  should be small so that it does not dominate the Riemannian metric tensor at any stage of iteration. After substituting (B.10) in (2.21) and dropping the constant “4”, the NG update of channel at  $(k+1)^{th}$  iteration is given by:

$$\hat{\mathbf{h}}_{k+1} = \hat{\mathbf{h}}_k + \mu \frac{\left( \left| |\hat{\mathbf{H}}_k| - |\hat{\mathbf{H}}_k|^2 \right| + \beta \mathbf{I} \right)}{\alpha_k (\mathbf{I} - 2|\hat{\mathbf{H}}_k|)^2} \nabla_{\hat{\mathbf{h}}_k} \mathcal{J}(\hat{\mathbf{h}}_k) \quad (\text{B.11})$$

Assume that at any iteration  $(\mathbf{I} - 2|\hat{\mathbf{H}}_k|) = 0$ , then the above equation goes to infinity and there is no solution. Hence, to overcome this problem (B.11) can be modified as:

$$\hat{\mathbf{h}}_{k+1} = \hat{\mathbf{h}}_k + \mu \frac{\left( \left| |\hat{\mathbf{H}}_k| - |\hat{\mathbf{H}}_k|^2 \right| + \beta \mathbf{I} \right)}{\alpha_k \mathbf{\Gamma}_2} \nabla_{\hat{\mathbf{h}}_k} \mathcal{J}(\hat{\mathbf{h}}_k) \quad (\text{B.12})$$

where  $\mathbf{\Gamma}_2 = (\mathbf{I} + 2|\hat{\mathbf{H}}_k|)^2$ .

Case 2 ( $\hat{h}_k(l)r_{k+1}(l) < 0$ ): For the second case, after expanding (2.27) yields

$$D = \sum_{l=0}^{L-1} \left| \sqrt{A - \alpha_k |r_{k+1}(l)| + 2B} - \sqrt{A} \right|^2 \quad (\text{B.13})$$

where  $A$  and  $B$  are given by (B.2) and (B.3) respectively. After solving the above equation as in Case 1, the channel update equation for the Case 2 is given by:

$$\hat{\mathbf{h}}_{k+1} = \hat{\mathbf{h}}_k + \mu \frac{\left( \left| |\hat{\mathbf{H}}_k| - |\hat{\mathbf{H}}_k|^2 \right| + \beta \mathbf{I} \right)}{\alpha_k (\mathbf{I} + 2|\hat{\mathbf{H}}_k|)^2} \nabla_{\hat{\mathbf{h}}_k} \mathcal{J}(\hat{\mathbf{h}}_k) \quad (\text{B.14})$$

Hence, for both the cases, the final channel update equation is given by (B.14).

# Appendix C

## Derivation of (2.33)

Let  $\tilde{\mathbf{h}}_k$  is the weight error vector which is defined as:

$$\tilde{\mathbf{h}}_k = \mathbf{h} - \hat{\mathbf{h}}_k \quad (\text{C.1})$$

then the transformed domain weight error vector can be represented as:

$$\acute{\mathbf{h}}_k = \mathbf{G}_{\hat{\mathbf{h}}_k}^{-1/2} \tilde{\mathbf{h}}_k = \mathbf{G}_{\hat{\mathbf{h}}_k}^{-1/2} \mathbf{h} - \check{\mathbf{h}}_k \quad (\text{C.2})$$

From Fig. 2.5,  $e(n) = \mathbf{h}^T \mathbf{x}(n) + v(n) - \check{\mathbf{h}}_k^T \mathbf{s}(n)$ , which can be further written as  $e(n) = \mathbf{h}^T \mathbf{G}_k^{-1/2} \mathbf{s}(n) + v(n) - \acute{\mathbf{h}}_k^T \mathbf{s}(n)$  and finally

$$e(n) = \acute{\mathbf{h}}_k^T \mathbf{s}(n) + v(n) \quad (\text{C.3})$$

or

$$e_k = \acute{\mathbf{h}}_k^T \tilde{\mathbf{q}}_k + \tilde{v} = \tilde{\mathbf{q}}_k^T \acute{\mathbf{h}}_k + \tilde{v} \quad (\text{C.4})$$

where  $\tilde{v} = v(i) - v(j)$ . Now (2.32) can be written in terms of transformed weight error vector as:

$$\mathbf{G}_{k+1}^{-1/2} \mathbf{h} - \acute{\mathbf{h}}_{k+1} = \mathbf{G}_k^{-1/2} \mathbf{h} - \acute{\mathbf{h}}_k + \frac{\mu}{\sigma_k^2} \sum_{i=1}^M \frac{\sum_{j=1}^M e_k \tilde{\mathbf{q}}_k K(e_k)}{\sum_{j=1}^M K(e_k)} \quad (\text{C.5})$$

Let assume  $\mathbf{G}_{k+1}^{-1/2} \mathbf{h} \approx \mathbf{G}_{\hat{\mathbf{h}}_k}^{-1/2} \mathbf{h}$  because the gain matrix do not change significantly from  $k^{th}$  to  $(k+1)^{th}$  index (near convergence), so the above equation can be written as:

$$\hat{\mathbf{h}}_{k+1} = \hat{\mathbf{h}}_k - \frac{\mu}{\sigma_k^2} \sum_{i=1}^M \frac{\sum_{j=1}^M \tilde{\mathbf{q}}_k e_k K(e_k)}{\sum_{j=1}^M K(e_k)} \quad (\text{C.6})$$

After substituting (C.4) into (C.6), the transformed weight error vector at  $(k+1)^{th}$  iteration is given as:

$$\hat{\mathbf{h}}_{k+1} = \hat{\mathbf{h}}_k - \frac{\mu}{\sigma_k^2} \sum_{i=1}^M \frac{\sum_{j=1}^M \tilde{\mathbf{q}}_k (\tilde{\mathbf{q}}_k^T \hat{\mathbf{h}}_k + \tilde{v}) K(e_k)}{\sum_{j=1}^M K(e_k)} \quad (\text{C.7})$$

Let  $\Delta_k = \mathbb{E}[\hat{\mathbf{h}}_k]$ , then the above equation can be written as:

$$\Delta_{k+1} \approx \Delta_k - \frac{\mu M}{\sigma_k^2} \frac{\left( \mathbb{E}[\tilde{\mathbf{q}}_k \tilde{\mathbf{q}}_k^T \hat{\mathbf{h}}_k K(e_k)] + \mathbb{E}[\tilde{\mathbf{q}}_k \tilde{v} K(e_k)] \right)}{\mathbb{E}[K(e_k)]} \quad (\text{C.8})$$

Since  $\hat{\mathbf{h}}_k$  is independent with  $\tilde{\mathbf{q}}_k$  and  $K(e_k)$ , and therefore  $\hat{\mathbf{h}}_k$  with  $\tilde{\mathbf{q}}_k$  and  $K(e_k)$  [48]. Also assume that  $\tilde{\mathbf{q}}_k$  is asymptotically uncorrelated with  $K(e_k)$  [107, 108]. Hence, by using above assumptions,  $\mathbb{E}[\tilde{\mathbf{q}}_k \tilde{\mathbf{q}}_k^T \hat{\mathbf{h}}_k K(e_k)]$  can be written as  $\mathbb{E}[\tilde{\mathbf{q}}_k \tilde{\mathbf{q}}_k^T] \Delta_k \mathbb{E}[K(e_k)]$ . Further,  $\mathbb{E}[\tilde{\mathbf{q}}_k \tilde{v} K(e_k)] = 0$  as  $\tilde{\mathbf{q}}_k$  is a zero mean and statistically independent of  $\tilde{v}$ . The above equation can then be written as:

$$\Delta_{k+1} \approx \Delta_k - \frac{\mu M}{\sigma_k^2} \mathbf{R}_{\mathbf{q},k} \Delta_k = \left( \mathbf{I} - \frac{\mu M}{\sigma_k^2} \mathbf{R}_{\mathbf{q},k} \right) \Delta_k \quad (\text{C.9})$$

For  $l^{th}$  tap,

$$\Delta_{k+1}(l) \approx \left( 1 - \frac{\mu M}{\sigma_k^2} \lambda_{\mathbf{q},k}(l) \right) \Delta_k(l) \quad (\text{C.10})$$

For stability or convergence of the proposed algorithm, the following condition satisfy

$$-1 < 1 - \frac{\mu M}{\sigma_k^2} \lambda_{\mathbf{q},k}(l) < 1 \quad \forall l \quad (\text{C.11})$$

For the stability of the proposed NG-NPML algorithm, the step-size  $\mu$  satisfying

$$0 < \mu < \frac{2\sigma_k^2}{M\lambda_{\mathbf{q},k}^{max}} \quad (\text{C.12})$$

It is observed from the above equation that the upper bound (on right hand side of (C.12)) on  $\mu$  varies at each iteration. However, this upper bound does not change significantly near convergence since  $Tr(\mathbf{R}_{\mathbf{q},k}) = Tr(\mathbb{E}[\mathbf{G}_k^{1/2}\mathbf{R}_{\mathbf{q}}\mathbf{G}_k^{1/2}])$ ,  $\mathbf{R}_{\mathbf{q}}$  is constant (as  $\mathbf{q}$  is constant), and it is assumed that near convergence  $\mathbf{G}_k$  does not change significantly, and hence from (C.12), the upper bound is constant near convergence.

# Appendix D

## Derivation of (2.34)

By using (C.3), the MSE is given by:

$$\xi_k = \xi_0 + \xi_{e,k} \quad (\text{D.1})$$

where  $\xi_k = \mathbb{E}[e_k^2]$ ,  $\xi_{e,k} = \mathbb{E}[\mathbf{h}_k^T \tilde{\mathbf{q}}_k \tilde{\mathbf{q}}_k^T \mathbf{h}_k]$  is the EMSE and cross term is zero. To evaluate the steady-state MSE, firstly the steady-state EMSE is calculated. Lets define

$$f(e_k) = \epsilon_k K(e_k) = e_k \exp\left(\frac{-e_k^2}{2\sigma_k^2}\right) \quad (\text{D.2})$$

$$\tilde{f}(e_k) = K(e_k) = \exp\left(\frac{-e_k^2}{2\sigma_k^2}\right) \quad (\text{D.3})$$

$$\Xi_k = \mathbf{h}_k^T \tilde{\mathbf{q}}_k \quad (\text{D.4})$$

Hence, the steady-state EMSE is given by:

$$\xi_{e,\infty} = \lim_{k \rightarrow \infty} \mathbb{E}[\Xi_k^2] \quad (\text{D.5})$$

By using (C.7) and some mathematical manipulation and approximation, the following relation holds for energy conservation [107, 108]:

$$\mathbb{E}[||\mathbf{h}_{k+1}||^2] \approx \mathbb{E}[||\mathbf{h}_k||^2] - \frac{2\mu M \mathbb{E}[\Xi_k f(e_k)]}{\sigma_k^2 \mathbb{E}[\tilde{f}(e_k)]} + \frac{\mu^2 M^2 \mathbb{E}[||\tilde{\mathbf{q}}_k||^2 f^2(e_k)]}{\sigma_k^4 \mathbb{E}[\tilde{f}^2(e_k)]} \quad (\text{D.6})$$

where  $\|\tilde{\mathbf{q}}_k\|^2 = \text{Tr}(\mathbf{R}_{\mathbf{q},k})$ . Assume that the estimator is in steady-state such that

$$\lim_{k \rightarrow \infty} \mathbb{E}[\|\mathbf{h}_{k+1}\|^2] = \lim_{k \rightarrow \infty} \mathbb{E}[\|\mathbf{h}_k\|^2] \quad (\text{D.7})$$

Hence, in the steady-state (D.7) becomes

$$2 \lim_{k \rightarrow \infty} \frac{\mathbb{E}[\Xi_k f(e_k)]}{\mathbb{E}[\tilde{f}(e_k)]} = \frac{\mu M}{\sigma_k^2} \lim_{k \rightarrow \infty} \frac{\mathbb{E}[\|\tilde{\mathbf{q}}_k\|^2 f^2(e_k)]}{\mathbb{E}[\tilde{f}^2(e_k)]} \quad (\text{D.8})$$

Taylor series expansion of the function  $f(\cdot)$  [108] for the derivation of steady-state EMSE is performed. Taking the Taylor series expansion of  $f(e_k)$  and  $\tilde{f}(e_k)$  with respect to  $\Xi_k$  around  $\tilde{v}$  yields

$$f(e_k) = f(\Xi_k + \tilde{v}) = f(\tilde{v}) + f'(\tilde{v})\Xi_k + \frac{1}{2}f''(\tilde{v})\Xi_k^2 + o(\Xi_k^2) \quad (\text{D.9})$$

$$\tilde{f}(e_k) = \tilde{f}(\Xi_k + \tilde{v}) = \tilde{f}(\tilde{v}) + \tilde{f}'(\tilde{v})\Xi_k + \frac{1}{2}\tilde{f}''(\tilde{v})\Xi_k^2 + o(\Xi_k^2) \quad (\text{D.10})$$

where  $o(\Xi_k^2)$  is the third and higher-order terms. Let assume  $\mathbb{E}[o(\Xi_k^2)]$  is very small and  $\|\tilde{\mathbf{q}}_k\|^2$  is asymptotically uncorrelated with  $f^2(e_k)$  [107, 109], then

$$\mathbb{E}[\Xi_k f(e_k)] \approx \mathbb{E}[\Xi_k f(\tilde{v}) + f'(\tilde{v})\Xi_k^2] \approx \mathbb{E}[f'(\tilde{v})]\xi_k \quad (\text{D.11})$$

$$\mathbb{E}[f^2(e_k)] \approx \mathbb{E}[f^2(\tilde{v})] + \mathbb{E}[f(\tilde{v})f''(\tilde{v}) + |f'(\tilde{v})|^2]\xi_k \quad (\text{D.12})$$

$$\mathbb{E}[\tilde{f}(e_k)] \approx \mathbb{E}[\tilde{f}(\tilde{v})] + \frac{1}{2}\mathbb{E}[\tilde{f}''(\tilde{v})]\xi_k \quad (\text{D.13})$$

$$\mathbb{E}[\tilde{f}^2(e_k)] \approx \mathbb{E}[\tilde{f}^2(\tilde{v})] + \mathbb{E}[\tilde{f}(\tilde{v})\tilde{f}''(\tilde{v}) + |\tilde{f}'(\tilde{v})|^2]\xi_k \quad (\text{D.14})$$

After substituting (D.11)-(D.14) into (D.8) yields

$$2 \frac{\mathbb{E}[f'(\tilde{v})]\xi_{e,k}}{\mathbb{E}[\tilde{f}(\tilde{v})] + \frac{1}{2}\mathbb{E}[\tilde{f}''(\tilde{v})]\xi_{e,k}} = \frac{\mu M \text{Tr}(\mathbf{R}_{\mathbf{q},k}) \left( \mathbb{E}[f^2(\tilde{v})] + \mathbb{E}[f(\tilde{v})f''(\tilde{v}) + |f'(\tilde{v})|^2]\xi_{e,k} \right)}{\sigma_k^2 \left( \mathbb{E}[\tilde{f}^2(\tilde{v})] + \mathbb{E}[\tilde{f}(\tilde{v})\tilde{f}''(\tilde{v}) + |\tilde{f}'(\tilde{v})|^2]\xi_{e,k} \right)} \quad (\text{D.15})$$

After some simple manipulation and assumption that  $\xi_{e,k}^2$  is very small at steady-state, and small value of  $\mu$ , (D.15) can be approximated as

$$\xi_{e,k} \approx \frac{\mu MTr(\mathbf{R}_{\mathbf{q},k})\mathbb{E}[f^2(\tilde{v})]\mathbb{E}[\tilde{f}(\tilde{v})]}{2\sigma_k^2\mathbb{E}[f'(\tilde{v})]\mathbb{E}[\tilde{f}^2(\tilde{v})]} \quad (\text{D.16})$$

Here,

$$f'(\tilde{v}) = \exp\left(\frac{-\tilde{v}^2}{2\sigma_k^2}\right)\left(1 - \frac{\tilde{v}^2}{\sigma_k^2}\right) \quad (\text{D.17})$$

After substituting (D.2), (D.3) and (D.17) into (D.16), the steady state EMSE can be approximated as:

$$\lim_{k \rightarrow \infty} \xi_{e,k} = \lim_{k \rightarrow \infty} \frac{\mu MTr(\mathbf{R}_{\mathbf{q},k})\mathbb{E}[\exp\left(\frac{-\tilde{v}^2}{\sigma_k^2}\right)\tilde{v}^2]\mathbb{E}[\exp\left(\frac{-\tilde{v}^2}{2\sigma_k^2}\right)]}{2\sigma_k^2\mathbb{E}[\exp\left(\frac{-\tilde{v}^2}{2\sigma_k^2}\right)\left(1 - \frac{\tilde{v}^2}{\sigma_k^2}\right)]\mathbb{E}[\exp\left(\frac{-\tilde{v}^2}{\sigma_k^2}\right)]} \quad (\text{D.18})$$

At steady-state, the mean of residual error,  $\mathbb{E}[e(n)]$ , is zero and hence  $\mathbb{E}[e_k]$  is also zero. Therefore, the EMSE of residual error at steady-state is given as:

$$\mathbb{E}[e^2(n)]_{e,\infty} = \lim_{k \rightarrow \infty} \xi_{e,k}/2 \quad (\text{D.19})$$

After substituting (D.18) into (D.1), the steady-state MSE is given by:

$$\xi_\infty = \xi_0 + \lim_{k \rightarrow \infty} \frac{\mu MTr(\mathbf{R}_{\mathbf{q},k})\mathbb{E}[\exp\left(\frac{-\tilde{v}^2}{\sigma_k^2}\right)\tilde{v}^2]\mathbb{E}[\exp\left(\frac{-\tilde{v}^2}{2\sigma_k^2}\right)]}{2\sigma_k^2\mathbb{E}[\exp\left(\frac{-\tilde{v}^2}{2\sigma_k^2}\right)\left(1 - \frac{\tilde{v}^2}{\sigma_k^2}\right)]\mathbb{E}[\exp\left(\frac{-\tilde{v}^2}{\sigma_k^2}\right)]} \quad (\text{D.20})$$

Similarly, the MSE of residual error at steady-state is given as:

$$\mathbb{E}[e^2(n)]_\infty = \xi_\infty/2 \quad (\text{D.21})$$

# Appendix E

## Derivation of (2.41)

After pre-multiplication of  $\mathbf{G}_{k+1}^{-1/2}$  to (2.39), leads to:

$$\check{\mathbf{h}}_{k+1} = \mathbf{G}_{k+1}^{-1/2} \hat{\mathbf{h}}_k - \rho \mathbf{G}_{k+1}^{-1/2} \nabla_{\hat{\mathbf{h}}_k} (\|\hat{\mathbf{h}}_k\|_1) + \frac{\mu}{\sigma_k^2} \sum_{i=1}^M \frac{\sum_{j=1}^M e_k \mathbf{G}_{k+1}^{-1/2} \mathbf{G}_k \mathbf{q} K(e_k)}{\sum_{k=1}^M K(e_k)} \quad (\text{E.1})$$

It is assumed that  $\mathbf{G}_{k+1}^{-1/2} \approx \mathbf{G}_k^{-1/2}$  near convergence and/or large order channels [48] and hence (E.1) can be written as:

$$\check{\mathbf{h}}_{k+1} = \check{\mathbf{h}}_k - \rho \mathbf{G}_k^{-1/2} \nabla_{\hat{\mathbf{h}}_k} (\|\hat{\mathbf{h}}_k\|_1) + \frac{\mu}{\sigma_k^2} \sum_{i=1}^M \frac{\sum_{j=1}^M e_k \tilde{\mathbf{q}}_k K(e_k)}{\sum_{k=1}^M K(e_k)} \quad (\text{E.2})$$

$\tilde{\mathbf{q}}_k$  is assumed to be zero mean Gaussian random variable for large order channel by the central limit theorem [48].

The above equation can be written in terms of transformed weight error vector as:

$$\mathbf{G}_{k+1}^{-1/2} \mathbf{h} - \hat{\mathbf{h}}_{k+1} = \mathbf{G}_k^{-1/2} \mathbf{h} - \hat{\mathbf{h}}_k - \rho \mathbf{G}_k^{-1/2} \nabla_{\hat{\mathbf{h}}_k} (\|\hat{\mathbf{h}}_k\|_1) + \frac{\mu}{\sigma_k^2} \sum_{i=1}^M \frac{\sum_{j=1}^M e_k \tilde{\mathbf{q}}_k K(e_k)}{\sum_{k=1}^M K(e_k)} \quad (\text{E.3})$$

The above equation can be rewritten as:

$$\hat{\mathbf{h}}_{k+1} = \hat{\mathbf{h}}_k + \rho \mathbf{G}_k^{-1/2} \nabla_{\hat{\mathbf{h}}_k} (\|\hat{\mathbf{h}}_k\|_1) - \frac{\mu}{\sigma_k^2} \sum_{i=1}^M \frac{\sum_{j=1}^M e_k \tilde{\mathbf{q}}_k K(e_k)}{\sum_{k=1}^M K(e_k)} \quad (\text{E.4})$$

After substituting (C.4) into (E.4), the transformed weight error vector at  $(k+1)^{th}$  iteration is given as:

$$\hat{\mathbf{h}}_{k+1} = \hat{\mathbf{h}}_k + \rho \mathbf{G}_k^{-1/2} \nabla_{\hat{\mathbf{h}}_k} (\|\hat{\mathbf{h}}_k\|_1) - \frac{\mu}{\sigma_k^2} \sum_{i=1}^M \frac{\sum_{j=1}^M \tilde{\mathbf{q}}_k (\tilde{\mathbf{q}}_k^T \hat{\mathbf{h}}_k + \tilde{v}) K(e_k)}{\sum_{k=1}^M K(e_k)} \quad (\text{E.5})$$

The above equation can be written as:

$$\Delta_{k+1} \approx \Delta_k + \rho \mathbb{E}[\mathbf{G}_k^{-1/2} \nabla_{\hat{\mathbf{h}}_k} (\|\hat{\mathbf{h}}_k\|_1)] - \frac{\mu M}{\sigma_k^2} \frac{(\mathbb{E}[\tilde{\mathbf{q}}_k \tilde{\mathbf{q}}_k^T \hat{\mathbf{h}}_k K(e_k)] + \mathbb{E}[\tilde{\mathbf{q}}_k \tilde{v} K(e_k)])}{\mathbb{E}[K(e_k)]} \quad (\text{E.6})$$

Using the independent assumption of  $\hat{\mathbf{h}}_k$  with  $\tilde{\mathbf{q}}_k$  and  $K(e_k)$ , and therefore  $\hat{\mathbf{h}}_k$  with  $\tilde{\mathbf{q}}_k$  and  $K(e_k)$  [110], and also assume that  $S_k$  is asymptotically uncorrelated with  $K(e_k)$  [107, 108]. Hence, by using above assumptions,  $\mathbb{E}[\tilde{\mathbf{q}}_k \tilde{\mathbf{q}}_k^T \hat{\mathbf{h}}_k K(e_k)]$  can be written as  $\mathbb{E}[\tilde{\mathbf{q}}_k \tilde{\mathbf{q}}_k^T] \Delta_k \mathbb{E}[K(e_k)]$ . Further,  $\mathbb{E}[\tilde{\mathbf{q}}_k \tilde{v} K(e_k)] = 0$  as  $\tilde{\mathbf{q}}_k$  is a zero mean and statistically independent of  $\tilde{v}$ . The above equation can then be written as:

$$\Delta_{k+1} \approx \left( \mathbf{I} - \frac{\mu M}{\sigma_k^2} \mathbf{R}_{\mathbf{q},k} \right) \Delta_k + \rho z_k \quad (\text{E.7})$$

where  $\mathbf{R}_{\mathbf{q},k} = \mathbb{E}[\tilde{\mathbf{q}}_k \tilde{\mathbf{q}}_k^T]$  is the auto-correlation matrix, and  $z_k = \mathbb{E}[\mathbf{G}_k^{-1/2} \nabla_{\hat{\mathbf{h}}_k} (\|\hat{\mathbf{h}}_k\|_1)]$ . The eigenvalue decomposition of  $\mathbf{R}_{\mathbf{q},k} = \mathbf{U} \Omega \mathbf{U}^T$ , where  $\Omega$  is diagonal matrix and  $\mathbf{U}$  is the unitary matrix with  $\mathbf{U}^T \mathbf{U} = \mathbf{U} \mathbf{U}^T = \mathbf{I}$ . Let  $\tilde{\Delta}_{k+1} = \mathbf{U}^T \Delta_{k+1}$ , then (E.7) can be written as:

$$\tilde{\Delta}_{k+1} \approx \left( \mathbf{I} - \frac{\mu M}{\sigma_k^2} \Omega \right) \tilde{\Delta}_k + \rho \mathbf{U}^T z_k \quad (\text{E.8})$$

Taking  $l_2$  norm on both sides of (E.8) and invoking triangle inequality property of norm, gives:

$$\|\tilde{\Delta}_{k+1}\|_2 \leq \left\| \left( \mathbf{I} - \frac{\mu M}{\sigma_k^2} \Omega \right) \right\|_2 \|\tilde{\Delta}_k\|_2 + \rho \|\mathbf{U}^T z_k\|_2 \quad (\text{E.9})$$

The above equation can be written as:

$$\|\Delta_{k+1}\|_2 \leq \sqrt{\sum_{i=0}^{L-1} \left( 1 - \frac{\mu M \lambda_{\mathbf{q},k}(l)}{\sigma_k^2} \right)^2} \|\Delta_k\|_2 + \rho c_k \quad (\text{E.10})$$

where  $\lambda_{q,k}$  is the eigenvalue of  $\mathbf{R}_{\mathbf{q},k}$ ,  $c_k = \sqrt{\sum_{i=0}^{L-1} g_{ii,k}^{-1}}$  (where  $g_{ii,k}$  is the diagonal element of  $\mathbf{G}_k$ ) is a positive constant for first three cases given in (2.40) and  $c_k = 0$  for the last case of (2.40). For stability or convergence of the proposed algorithm, the following condition must satisfy

$$-1 < 1 - \frac{\mu M \lambda_{\mathbf{q},k}(l)}{\sigma_k^2} < 1 \quad (\text{E.11})$$

and hence step-size  $\mu$  satisfy the following condition:

$$0 < \mu < \frac{2\sigma_k^2}{M \lambda_{\mathbf{q},k}^{max}} \quad (\text{E.12})$$

# Appendix F

## Derivation of (3.37)

Under  $\mathcal{H}_1$ ,  $A = p/(p + q)$  and hence  $\frac{\partial g(A)}{\partial A} = \left[ \frac{\partial g(A)}{\partial p} \quad \frac{\partial g(A)}{\partial q} \right]^T$ .

For  $g(A) = \sqrt{\ln(A/\gamma_{GCM})}$ ,

$$\frac{\partial g(A)}{\partial p} = \frac{1}{2A} \ln\left(\frac{A}{\gamma_{GCM}}\right)^{-1/2} \frac{q}{(p+q)^2} \quad (\text{F.1})$$

and

$$\frac{\partial g(A)}{\partial q} = -\frac{1}{2A} \ln\left(\frac{A}{\gamma_{GCM}}\right)^{-1/2} \frac{p}{(p+q)^2} \quad (\text{F.2})$$

By using (F.1) and (F.2)

$$\frac{\partial g(A)}{\partial A} = \frac{1}{2A} \ln\left(\frac{A}{\gamma_{GCM}}\right)^{-1/2} \left[ \frac{q}{(p+q)^2} \quad \frac{-p}{(p+q)^2} \right]^T \quad (\text{F.3})$$

Now, the FIM,  $\mathbf{I}_\theta$ , of  $\theta$  is given as:

$$\mathbf{F}_\theta = -\mathbb{E}\left[\frac{\partial^2 \ln f(x; \theta)}{\partial \theta^2}\right] \quad (\text{F.4})$$

So, the FIM,  $\mathbf{I}_A$ , of  $A$  is given as:

$$\mathbf{F}_A = -\mathbb{E}\left[\frac{\partial^2 \ln f(\rho)}{\partial A^2}\right] \quad (\text{F.5})$$

As  $A$  consists of two variable  $p$  and  $q$ , and hence  $\mathbf{F}_A$  is  $2 \times 2$  matrix given as:

$$\mathbf{F}_A = -\mathbb{E} \begin{bmatrix} \frac{\partial^2 \ln f(\rho)}{\partial p^2} & \frac{\partial^2 \ln f(\rho)}{\partial p \partial q} \\ \frac{\partial^2 \ln f(\rho)}{\partial p \partial q} & \frac{\partial^2 \ln f(\rho)}{\partial q^2} \end{bmatrix} \quad (\text{F.6})$$

Assume that the  $\rho$  is i.i.d., then from (3.24), for  $M_s$  samples,  $f(\rho)$  can be expressed under  $\mathcal{H}_1$  as:

$$f(\rho) = \prod_{k=1}^{M_s} \frac{\rho(k)^{p-1} (1 - \rho(k))^{q-1}}{B(p, q)} \quad (\text{F.7})$$

by taking  $\ln$  (i.e.  $\log_e$ ) on both sides

$$\ln f(\rho) = \sum_{k=1}^{M_s} (p-1) \ln \rho(k) + (q-1) \ln(1 - \rho(k)) + \ln \Gamma(p+q) - \ln \Gamma p - \ln \Gamma q \quad (\text{F.8})$$

So,

$$\frac{\partial \ln f(\rho)}{\partial p} = \sum_{k=1}^{M_s} \ln \rho(k) + M_s \frac{\Gamma'(p+q)}{\Gamma(p+q)} - M_s \frac{\Gamma' p}{\Gamma p} \quad (\text{F.9})$$

$$\frac{\partial \ln f(\rho)}{\partial q} = \sum_{k=1}^{M_s} \ln(1 - \rho(k)) + M_s \frac{\Gamma'(p+q)}{\Gamma(p+q)} - M_s \frac{\Gamma' q}{\Gamma q} \quad (\text{F.10})$$

$$\frac{\partial^2 \ln f(\rho)}{\partial p^2} = M_s \frac{\Gamma(p+q) \Gamma''(p+q) - (\Gamma'(p+q))^2}{(\Gamma(p+q))^2} - M_s \frac{\Gamma p \Gamma'' p - (\Gamma' p)^2}{(\Gamma p)^2} \quad (\text{F.11})$$

$$\frac{\partial^2 \ln f(\rho)}{\partial q^2} = M_s \frac{\Gamma(p+q) \Gamma''(p+q) - (\Gamma'(p+q))^2}{(\Gamma(p+q))^2} - M_s \frac{\Gamma q \Gamma'' q - (\Gamma' q)^2}{(\Gamma q)^2} \quad (\text{F.12})$$

$$\frac{\partial^2 \ln f(\rho)}{\partial p \partial q} = \frac{\partial^2 \ln f(\rho)}{\partial q \partial p} = M_s \frac{\Gamma(p+q) \Gamma''(p+q) - (\Gamma'(p+q))^2}{(\Gamma(p+q))^2} \quad (\text{F.13})$$

Thus, after substituting (F.11), (F.12) and (F.13) into (F.6)  $\mathbf{F}_A = \mathbf{C}$  is obtained as given in (3.39), since (F.3) is equivalent to  $\mathbf{b}$  as given in (3.38) and hence (3.37) after substituting (F.3) and (F.6) into (3.36) are obtained.

# Appendix G

## Derivation of (3.41)

For  $g(A) = \ln(A/\gamma_{GCM})$ ,

$$\frac{\partial g(A)}{\partial p} = \frac{1}{A} \frac{q}{(p+q)^2} \quad (\text{G.1})$$

and

$$\frac{\partial g(A)}{\partial q} = -\frac{1}{A} \frac{p}{(p+q)^2} \quad (\text{G.2})$$

By using (H.1) and (H.2)

$$\frac{\partial g(A)}{\partial A} = \frac{1}{A} \left[ \frac{q}{(p+q)^2} \quad \frac{-p}{(p+q)^2} \right]^T \quad (\text{G.3})$$

which is equivalent to  $\mathbf{d}$  as given in (3.42). After substituting (F.6) and (G.3) into (3.36), leads to (3.41).

# Appendix H

## Derivation of (4.10)

The probability of symbol error, given  $X$  was transmitted can be represented as:

$$P_e(\hat{X}|X)|_{X \in C} = \int_{l_l}^{u_l} \hat{f}(E + \sqrt{\tilde{E}_s}) dE|_{X \in C} \quad (\text{H.1})$$

where  $l_l$  and  $u_l$  are the lower and upper limit for the  $X$  to be decoded erroneously. Let  $s_e(k_c)$  be BPSK modulated, where 0's and 1's are mapped to -1's and +1's respectively. The  $P_e$ , when the transmitted signal was -1 can be written as:

$$P_e(\hat{X} | -1) = \int_0^\infty \hat{f}(E_R + \sqrt{\tilde{E}_s}) dE_R \quad (\text{H.2})$$

where  $E_R$  represents the real value of  $E$ . Then with the help of (2.15) and (2.16) for estimated PDF in the frequency domain, the above expression can be written as:

$$P_e(\hat{X} | -1) = \int_0^\infty \frac{1}{N} \sum_{j=1}^N \phi(E_R - E_R(j) + \sqrt{\tilde{E}_s}) dE_R \quad (\text{H.3})$$

$$= \int_0^\infty \frac{1}{N} \sum_{j=1}^N \frac{1}{\sqrt{2\pi\sigma_k^2}} \exp\left(\frac{-(E_R - E_R(j) + \sqrt{\tilde{E}_s})^2}{2\sigma_k^2}\right) dE_R \quad (\text{H.4})$$

The above equation can be written as:

$$P_e(\hat{X} | -1) = \frac{1}{N} \sum_{j=1}^N \frac{1}{\sqrt{2\pi\sigma_k^2}} \int_0^\infty \exp\left(\frac{-(E_R - E_R(j) + \sqrt{\tilde{E}_s})^2}{2\sigma_k^2}\right) dE_R \quad (\text{H.5})$$

Let

$$z = \frac{E_R - E_R(j) + \sqrt{\tilde{E}_s}}{\sqrt{2}\sigma_k} \quad (\text{H.6})$$

then

$$dz = \frac{dE_R}{\sqrt{2}\sigma_k} \quad (\text{H.7})$$

After substituting (H.6) and (H.7) in (H.5), the probability of error can be rewritten as:

$$P_e(\hat{X} | -1) = \frac{1}{N} \sum_{j=1}^N \frac{1}{\sqrt{\pi}} \int_{(\sqrt{\tilde{E}_s} - E_R(j))/\sqrt{2}\sigma_k}^{\infty} \exp(-z^2) dz \quad (\text{H.8})$$

The above equation can be written in terms of complementary error function as:

$$P_e(\hat{X} | -1) = \frac{1}{N} \sum_{j=1}^N \frac{1}{2} \operatorname{erfc}\left(\frac{\sqrt{\tilde{E}_s} - E_R(j)}{\sqrt{2}\sigma_k}\right) \quad (\text{H.9})$$

Similarly, the probability of error, when the transmitted signal was +1 can be represented as:

$$P_e(\hat{X} | +1) = \int_{-\infty}^0 \frac{1}{N} \sum_{j=1}^N \phi(E_R - E_R(j) - \sqrt{\tilde{E}_s}) dE_R \quad (\text{H.10})$$

By using same procedure as used for calculation of  $P_e(\hat{X} | -1)$ , the above equation can be written as:

$$P_e(\hat{X} | +1) = \frac{1}{N} \sum_{j=1}^N \frac{1}{2} \operatorname{erfc}\left(\frac{\sqrt{\tilde{E}_s} + E_R(j)}{\sqrt{2}\sigma_k}\right) \quad (\text{H.11})$$

Hence, the average probability of symbol error in AWGN channel is given as:

$$P_e = \frac{1}{2N} \sum_{j=1}^N \frac{1}{2} \operatorname{erfc}\left(\frac{\sqrt{\tilde{E}_s} - E_R(j)}{\sqrt{2}\sigma_k}\right) + \frac{1}{2N} \sum_{j=1}^N \frac{1}{2} \operatorname{erfc}\left(\frac{\sqrt{\tilde{E}_s} + E_R(j)}{\sqrt{2}\sigma_k}\right) \quad (\text{H.12})$$

The term 1/2 in both the above expressions is due to equiprobable BPSK symbols.

# Appendix I

## Derivation of (4.11)

For QPSK, the constellation set  $C$  consists of  $\{-1+i1, 1+i1, 1-i1, -1-i1\}$  and hence  $E$  is also complex ( $\in \mathbb{C}$ ). Thus, the PDF of in-phase component and quadrature component of  $E$  are separately calculated. Hence, on the basis of PDF of real and imaginary  $E$ , and following the same procedure as used in BPSK, the probability of symbol error when the transmitted symbol was “ $-1+i1$ ” can be calculated as:

$$P_e(\hat{X}|-1+i1) = \frac{1}{4N} \sum_{j=1}^N \frac{1}{2} \operatorname{erfc}\left(\frac{\sqrt{\tilde{E}_s/2} - E_R(j)}{\sqrt{2\sigma_k^2}}\right) + \frac{1}{4N} \sum_{j=1}^N \frac{1}{2} \operatorname{erfc}\left(\frac{\sqrt{\tilde{E}_s/2} + E_I(j)}{\sqrt{2\sigma_k^2}}\right) \quad (\text{I.1})$$

where  $E_I$  represent the imaginary part of  $E$ . Similarly, the probability of symbol error when the transmitted symbol was “ $1+i1$ ” can be calculated as:

$$P_e(\hat{X}|1+i1) = \frac{1}{4N} \sum_{j=1}^N \frac{1}{2} \operatorname{erfc}\left(\frac{\sqrt{\tilde{E}_s/2} + E_R(j)}{\sqrt{2\sigma_k^2}}\right) + \frac{1}{4N} \sum_{j=1}^N \frac{1}{2} \operatorname{erfc}\left(\frac{\sqrt{\tilde{E}_s/2} + E_I(j)}{\sqrt{2\sigma_k^2}}\right) \quad (\text{I.2})$$

the probability of symbol error when the transmitted symbol was “ $1-i1$ ” can be calculated as:

$$P_e(\hat{X}|1-i1) = \frac{1}{4N} \sum_{j=1}^N \frac{1}{2} \operatorname{erfc}\left(\frac{\sqrt{\tilde{E}_s/2} + E_R(j)}{\sqrt{2\sigma_k^2}}\right) + \frac{1}{4N} \sum_{j=1}^N \frac{1}{2} \operatorname{erfc}\left(\frac{\sqrt{\tilde{E}_s/2} - E_I(j)}{\sqrt{2\sigma_k^2}}\right) \quad (\text{I.3})$$

and similarly the probability of symbol error when the transmitted symbol was “-1-i1” can be calculated as:

$$P_e(\hat{X}|-1-i1) = \frac{1}{4N} \sum_{j=1}^N \frac{1}{2} \operatorname{erfc}\left(\frac{\sqrt{\tilde{E}_s/2} - E_R(j)}{\sqrt{2\sigma^2}}\right) + \frac{1}{4N} \sum_{j=1}^N \frac{1}{2} \operatorname{erfc}\left(\frac{\sqrt{\tilde{E}_s/2} - E_I(j)}{\sqrt{2\sigma_k^2}}\right) \quad (\text{I.4})$$

Hence, the average probability of symbol error in AWGN channel is given as:

$$\begin{aligned} P_e = & \frac{1}{2N} \sum_{j=1}^N \frac{1}{2} \operatorname{erfc}\left(\frac{\sqrt{\tilde{E}_s/2} + E_R(j)}{\sqrt{2\sigma_k^2}}\right) + \frac{1}{2N} \sum_{j=1}^N \frac{1}{2} \operatorname{erfc}\left(\frac{\sqrt{\tilde{E}_s/2} - E_R(j)}{\sqrt{2\sigma_k^2}}\right) \\ & + \frac{1}{2N} \sum_{j=1}^N \frac{1}{2} \operatorname{erfc}\left(\frac{\sqrt{\tilde{E}_s/2} + E_I(j)}{\sqrt{2\sigma^2}}\right) + \frac{1}{2N} \sum_{j=1}^N \frac{1}{2} \operatorname{erfc}\left(\frac{\sqrt{\tilde{E}_s/2} - E_I(j)}{\sqrt{2\sigma_k^2}}\right) \end{aligned} \quad (\text{I.5})$$



# References

- [1] A. N. Mody, “IEEE 802.22-cognitive radio-based regional area and smart utility networks,” [online].<http://smartgrid.epri.com>.
- [2] A. K. Mishra and D. L. Johnson, *White Space Communication*. Springer, 2015.
- [3] “Regulatory Requirements for White Space Device in the UHF TV Band, OFCOM,” Tech. Rep., 2012.
- [4] M. Nekovee, “Quantifying the availability of TV white spaces for cognitive radio operation in the UK,” in *Proc. IEEE Intl. Conf. Commun. Workshops*, Dresden, Germany, 2009, pp. 1–5.
- [5] IEEE 802.22 Working Group on Wireless Regional Area Networks, “Functional requirements for the 802.22 WRAN, Doc: IEEE 802.22-05/0007r46,” Tech. Rep., 2005.
- [6] —, “Cognitive wireless RAN medium access control (MAC) and Physical layer (PHY) specifications: Policies and procedures for operation in the TV Bands amendment: Enhancement for broadband services and monitoring applications,” Tech. Rep., 2011.
- [7] —, “Standard for spectrum characterization and occupancy sensing,” Tech. Rep., 2014.
- [8] P. Gronsund, P. Pawelczak, J. Park, and D. Cabric, “System level performance

- of IEEE 802.22-2011 with sensing-based detection of wireless microphones,” *IEEE Commun. Mag.*, vol. 52, no. 1, pp. 200–209, 2014.
- [9] H. Harada, “White space communication systems: An overview of regulation, standardization and trial,” *IEICE Trans. Commun.*, vol. 97, no. 2, pp. 261–274, 2014.
- [10] G. Naik, S. Singhal, A. Kumar, and A. Karandikar, “Quantitative assessment of TV white space in India,” in *Twentieth National Conf. Commun.* IEEE, 2014, pp. 1–6.
- [11] C. R. Stevenson, G. Chouinard, Z. Lei, W. Hu, S. J. Shellhammer, and W. Caldwell, “IEEE 802.22: The first cognitive radio wireless regional area network standard,” *IEEE Commun. Mag.*, vol. 47, no. 1, pp. 130–138, 2009.
- [12] M. Park, “IEEE 802.11 ah: sub-1-GHz license-exempt operation for the Internet of Things,” *IEEE Commun. Mag.*, vol. 53, no. 9, pp. 145–151, 2015.
- [13] S. Aust, R. V. Prasad, and I. G. Niemegeers, “Outdoor long-range WLANs: A lesson for IEEE 802.11 ah,” *IEEE Commun. Surveys & Tutorials*, vol. 17, no. 3, pp. 1761–1775, 2015.
- [14] W. Sun, M. Choi, and S. Choi, “IEEE 802.11 ah: A long range 802.11 WLAN at sub 1 GHz,” *Journal of ICT Standardization*, vol. 1, no. 1, pp. 83–108, 2013.
- [15] E. Khorov, A. Lyakhov, A. Krotov, and A. Guschin, “A survey on IEEE 802.11 ah: An enabling networking technology for smart cities,” *Comput. Commun.*, vol. 58, pp. 53–69, 2015.
- [16] Y. Zeng, C. Xu, and Y. C. Li, “WRAN discrete channel B, IEEE 802.22-07/0185r1,” Tech. Rep., 2007.
- [17] T. Kamenosono, M. Kaneko, K. Hayashi, and M. Sakai, “Compressed sensing-based channel estimation methods for LTE-Advanced multi-user downlink

- MIMO system,” in *Proc. IEEE Veh. Technol. Conf.*, Glasgow, Scotland, May 2015, pp. 1–5.
- [18] P. De, J. Bao, and T. Poon, “A calculation-efficient algorithm for decision feedback equalizers,” *IEEE Trans. Cons. Elect.*, vol. 45, no. 3, pp. 526–532, Aug. 1999.
- [19] M. Kokshoorn, H. Chen, P. Wang, Y. Li, and B. Vucetic, “Millimeter wave MIMO channel estimation using overlapped beam patterns and rate adaptation,” *IEEE Trans. Signal Process.*, vol. 65, no. 3, pp. 601–616, Feb. 2017.
- [20] A. Bishnu and V. Bhatia, “On performance analysis of IEEE 802.22 (PHY) for COST-207 channel models,” in *Proc. IEEE Conf. Standards Commun. Networking*, Tokyo, Japan, 2015, pp. 229–234.
- [21] R. Jain, “Channel models a tutorial,” in *WiMAX forum AATG*, 2007, pp. 1–6.
- [22] G. Taubock and F. Hlawatsch, “A compressed sensing technique for OFDM channel estimation in mobile environments: Exploiting channel sparsity for reducing pilots,” in *Proc. IEEE Intl. Conf. Acoustics Speech Signal Process.*, Las Vegas, USA, Apr. 2008, pp. 2885–2888.
- [23] H. Xie, G. Andrieux, Y. Wang, J. F. Diouris, and S. Feng, “Threshold based most significant taps detection for sparse channel estimation in OFDM system,” in *Proc. IEEE Intl. Conf. Signal Proces. Commun. Computing*, Kunming, China, Nov. 2013, pp. 1–5.
- [24] W. Ding, F. Yang, W. Dai, and J. Song, “Time–frequency joint sparse channel estimation for MIMO-OFDM systems,” *IEEE Commun. Lett.*, vol. 19, no. 1, pp. 58–61, Jan. 2015.
- [25] Y. Li, Y. Wang, and F. Albu, “Sparse channel estimation based on a reweighted least-mean mixed-norm adaptive filter algorithm,” in *Proc. IEEE*

- 24th European Signal Process. Conf.*, Budapest, Hungary, Dec. 2016, pp. 2380–2384.
- [26] Y. Li, Y. Wang, and T. Jiang, “Low complexity norm-adaption least mean square/fourth algorithm and its applications for sparse channel estimation,” in *Proc. IEEE Wireless Commun. Netw. Conf.*, Doha, Qatar, Sep. 2016, pp. 1–6.
- [27] D. L. Duttweiler, “Proportionate normalized least-mean-squares adaptation in echo cancelers,” *IEEE Trans. Acoust., Speech, Signal Process.*, vol. 8, no. 5, pp. 508–518, 2000.
- [28] H. Deng and M. Doroslovacki, “Improving convergence of the PNLMS algorithm for sparse impulse response identification,” *IEEE Signal Process. Lett.*, vol. 12, no. 3, pp. 181–184, 2005.
- [29] P. Loganathan, A. W. Khong, and P. A. Naylor, “A class of sparseness-controlled algorithms for echo cancellation,” *IEEE Trans. Acoust., Speech, Language Process.*, vol. 17, no. 8, pp. 1591–1601, 2009.
- [30] Y. Chen, Y. Gu, and A. O. Hero, “Sparse LMS for system identification,” in *Proc. IEEE Int. Conf. Acoust., Speech, Signal Process.*, Taipei, Taiwan, 2009, pp. 3125–3128.
- [31] A. C. Cirik, O. Taghizadeh, L. Lampe, R. Mathar, and Y. Hua, “Linear transceiver design for full-duplex multi-cell MIMO systems,” *IEEE Access*, vol. 4, pp. 4678–4689, 2016.
- [32] V. Bhatia and B. Mulgrew, “Non-parametric likelihood based channel estimator for Gaussian mixture noise,” *Elsevier Signal Process.*, vol. 87, no. 11, pp. 2569–2586, 2007.
- [33] K. Pelekanakis and M. Chitre, “Adaptive sparse channel estimation under symmetric alpha-stable noise,” *IEEE Trans. Wireless Commun.*, vol. 13, no. 6, pp. 3183–3195, 2014.

- [34] T. Zhang, H.-Q. Jiao, and Z. Lei, “Individual-activation-factor memory proportionate affine projection algorithm with evolving regularization,” *IEEE Access*, vol. 5, pp. 4939–4946, 2017.
- [35] M. A. Chitre, J. R. Potter, and S.-H. Ong, “Optimal and near-optimal signal detection in snapping shrimp dominated ambient noise,” *IEEE J. Ocean. Eng.*, vol. 31, no. 2, pp. 497–503, 2006.
- [36] V. G. Chavali and C. R. da Silva, “Classification of digital amplitude-phase modulated signals in time-correlated non-Gaussian channels,” *IEEE Trans. on Commun.*, vol. 61, no. 6, pp. 2408–2419, 2013.
- [37] A. Liu, V. Lau, and W. Dai, “Joint burst LASSO for sparse channel estimation in multi-user massive MIMO,” in *Proc. IEEE Int. Conf. Commun.*, Kuala Lumpur, Malaysia, 2016, pp. 1–6.
- [38] S. F. Cotter and B. D. Rao, “Sparse channel estimation via matching pursuit with application to equalization,” *IEEE Trans. on Commun.*, vol. 50, no. 3, pp. 374–377, 2002.
- [39] G. Z. Karabulut and A. Yongacoglu, “Sparse channel estimation using orthogonal matching pursuit algorithm,” in *Proc. IEEE 60th Veh. Technol. Conf.*, Los Angeles, CA, USA, 2004, pp. 3880–3884.
- [40] A. Singh and J. C. Principe, “Using correntropy as a cost function in linear adaptive filters,” in *Proc. IEEE Int. Joint Conf. Neural Networks*, Atlanta, GA, USA, 2009, pp. 2950–2955.
- [41] F. Huang, J. Zhang, and S. Zhang, “Maximum Versoria criterion-based robust adaptive filtering algorithm,” *IEEE Trans. Circuits Syst. II, Exp. Briefs*, vol. 64, no. 10, pp. 1252–1256, 2017.
- [42] D. B. Haddad, M. R. Petraglia, and A. Petraglia, “A unified approach for sparsity-aware and maximum correntropy adaptive filters,” in *Proc. IEEE 24th European Signal Process. Conf.*, Budapest, Hungary, 2016, pp. 170–174.

- [43] T. Hwang, C. Yang, G. Wu, S. Li, and G. Y. Li, “OFDM and its wireless applications: A survey,” *IEEE Transactions on Vehicular Technology*, vol. 58, no. 4, pp. 1673–1694, 2009.
- [44] A. Bishnu, A. Jain, and A. Shrivastava, “A new scheme of ICI self-cancellation in OFDM system,” in *Proc. IEEE Intl. Conf. Commun. Syst. Net. Technol.*, Gwalior, India, 2013, pp. 120–123.
- [45] —, “Optimized sinc power pulse for inter carrier interference mitigation in OFDM system,” in *Proc. IEEE Annual India Conf.*, Mumbai, India, 2013, pp. 1–4.
- [46] B. W. Silverman, *Density Estimation for Statistics and Data Analysis*. CRC Press, 1998.
- [47] S. L. Gay and S. C. Douglas, “Normalized natural gradient adaptive filtering for sparse and non-sparse systems,” in *Proc. IEEE Int. Conf. Acoust., Speech, Signal Process.*, vol. 2, Orlando, FL, USA, 2002, pp. 1405–1408.
- [48] R. L. Das and M. Chakraborty, “On convergence of proportionate-type normalized least mean square algorithms,” *IEEE Trans. Circuits Syst. II, Exp. Briefs*, vol. 62, no. 5, pp. 491–495, 2015.
- [49] T. Y. Al-Naffouri and A. H. Sayed, “Adaptive filters with error nonlinearities: Mean-square analysis and optimum design,” *EURASIP J. on Appl. Signal Process.*, vol. 2001, no. 1, pp. 192–205, 2001.
- [50] F. Wan, W.-P. Zhu, and M. Swamy, “Semi-blind most significant tap detection for sparse channel estimation of OFDM systems,” *IEEE Trans. Circuits Syst. I, Reg. Papers*, vol. 57, no. 3, pp. 703–713, 2010.
- [51] R. L. Das and M. Chakraborty, “Improving the performance of the PNLMS algorithm using  $l_1$  norm regularization,” *IEEE Trans. Acoust., Speech, Language Process.*, vol. 24, no. 7, pp. 1280–1290, 2016.

- [52] B. Wang and K. R. Liu, “Advances in cognitive radio networks: A survey,” *IEEE J. Sel. Topics Signal Process.*, vol. 5, no. 1, pp. 5–23, 2011.
- [53] A. Ghasemi and E. S. Sousa, “Spectrum sensing in cognitive radio networks: Requirements, challenges and design trade-offs,” *IEEE Commun. Mag.*, vol. 46, no. 4, 2008.
- [54] R. Rao, Q. Cheng, and P. K. Varshney, “Subspace-based cooperative spectrum sensing for cognitive radios,” *IEEE Sensors J.*, vol. 11, no. 3, pp. 611–620, 2011.
- [55] A. M. Mossaa and V. Jeoti, “Cognitive radio: Cyclostationarity-based classification approach for analog TV and wireless microphone signals,” in *Proc. IEEE Innovative Tech. Intell. Sys. Ind. Appl.*, Monash, Malaysia, 2009, pp. 107–111.
- [56] S. Hou and R. C. Qiu, “Kernel feature template matching for spectrum sensing,” *IEEE Trans. Veh. Tech.*, vol. 63, no. 5, pp. 2258–2271, 2014.
- [57] Y. Zeng and Y.-C. Liang, “Spectrum-sensing algorithms for cognitive radio based on statistical covariances,” *IEEE Trans. Veh. Tech.*, vol. 58, no. 4, pp. 1804–1815, 2009.
- [58] J. Renard, L. H.-J. Lampe, and F. Horlin, “Scaled largest eigenvalue detection for stationary times-series,” *IEEE Trans. Signal Process.*, vol. 64, no. 5, pp. 1161–1172, 2016.
- [59] Z. Li, D. Wang, P. Qi, and B. Hao, “Maximum-eigenvalue-based sensing and power recognition for multiantenna cognitive radio system,” *IEEE Trans. Veh. Technol.*, vol. 65, no. 10, pp. 8218–8229, 2016.
- [60] F. A. Bhatti, G. B. Rowe, and K. W. Sowerby, “Spectrum sensing using principal component analysis,” in *Proc. IEEE Wireless Commun. Net. Conf.*, Shanghai, China, 2012, pp. 725–730.

- [61] Y. Zeng and Y.-C. Liang, “Eigenvalue-based spectrum sensing algorithms for cognitive radio,” *IEEE Trans. Commun.*, vol. 57, no. 6, pp. 1784–1793, 2009.
- [62] P. Zhang and R. Qiu, “GLRT-based spectrum sensing with blindly learned feature under rank-1 assumption,” *IEEE Trans. Commun.*, vol. 61, no. 1, pp. 87–96, 2013.
- [63] F. Lin, R. C. Qiu, Z. Hu, S. Hou, J. P. Browning, and M. C. Wicks, “Generalized FMD detection for spectrum sensing under low signal-to-noise ratio,” *IEEE Commun. Lett.*, vol. 16, no. 5, pp. 604–607, 2012.
- [64] C. Vladeanu, C.-V. Nastase, and A. Martian, “Energy detection algorithm for spectrum sensing using three consecutive sensing events,” *IEEE Wireless Commun. Lett.*, vol. 5, no. 3, pp. 284–287, 2016.
- [65] S. K. Sharma, S. Chatzinotas, and B. Ottersten, “Eigenvalue-based sensing and SNR estimation for cognitive radio in presence of noise correlation,” *IEEE Trans. Veh. Technol.*, vol. 62, no. 8, pp. 3671–3684, 2013.
- [66] ———, “Maximum eigenvalue detection for spectrum sensing under correlated noise,” in *Proc. IEEE Int. Conf. Acoustics, Speech Signal Process.*, Florence, Italy, 2014, pp. 7268–7272.
- [67] N. Gupta and V. A. Bohara, “An adaptive subcarrier sharing scheme for OFDM-based cooperative cognitive radios,” *IEEE Trans. Cognitive Commun. Networking*, vol. 2, no. 4, pp. 370–380, 2016.
- [68] H. Chen, M. Zhou, L. Xie, and J. Li, “Cooperative spectrum sensing with M-ary quantized data in cognitive radio networks under SSDF attacks,” *IEEE Trans. Wireless Commun.*, vol. 16, no. 8, pp. 5244–5257, 2017.
- [69] V. Matta, P. Braca, S. Marano, and A. H. Sayed, “Distributed detection over adaptive networks: Refined asymptotics and the role of connectivity,” *IEEE Trans. Signal Inf. Process. Netw.*, vol. 2, no. 4, pp. 442–460, 2016.

- [70] G. Ganesan and Y. Li, “Cooperative spectrum sensing in cognitive radio networks,” in *Proc. IEEE First Intl. Symp. New Frontiers in Dynamic Spectrum Access Networks*, Baltimore, MD, USA, USA, 2005, pp. 137–143.
- [71] H. Kim and K. G. Shin, “In-Band spectrum sensing in IEEE 802.22 WRANs for incumbent protection,” *IEEE Trans. Mob. Comp.*, vol. 9, no. 12, pp. 1766–1779, 2010.
- [72] J. Hamm and D. D. Lee, “Grassmann discriminant analysis: A unifying view on subspace-based learning,” in *Proc. ACM 25th Intl. Conf. Mach. Lear.*, Helsinki, Finland, 2008, pp. 376–383.
- [73] H. Wang, X. Chai, X. Hong, G. Zhao, and X. Chen, “Isolated sign language recognition with Grassmann covariance matrices,” *ACM Trans. Access. Comp.*, vol. 8, no. 4, pp. 14:1–14:21, 2016.
- [74] C. O. Sakar and O. Kursun, “Discriminative feature extraction by a neural implementation of canonical correlation analysis,” *IEEE Trans. Neural Netw. Learning Syst.*, vol. 28, no. 1, pp. 164–176, 2017.
- [75] A. Ghasemi and E. S. Sousa, “Collaborative spectrum sensing for opportunistic access in fading environments,” in *Proc. IEEE Int. Symp. New Frontiers Dynamic Spectrum Access Networks*, Baltimore, MD, USA, USA, 2005, pp. 131–136.
- [76] I. S. Gradshteyn and I. M. Ryzhik, *Table of integrals, series, and products*. Academic press, 2014.
- [77] A. Ghobadzadeh, S. Gazor, M. R. Taban, A. A. Tadaion, and M. Gazor, “Separating function estimation tests: A new perspective on binary composite hypothesis testing,” *IEEE Trans. Signal Process.*, vol. 60, no. 11, pp. 5626–5639, 2012.
- [78] A. DasGupta, *Fundamentals of Probability: A First Course*. Springer Science & Business Media, 2010.

- [79] M. Naderpour, A. Ghobadzadeh, A. Tadaion, and S. Gazor, “Generalized Wald test for binary composite hypothesis test,” *IEEE Signal Process. Lett.*, vol. 22, no. 12, pp. 2239–2243, 2015.
- [80] V. Tawil, “51 captured DTV signal,” 2006. [online]. Available: <http://grouper.ieee.org/groups/802/22/Meetingdocuments/2006May>.
- [81] S. Shellhammer, V. Tawil, G. Chouinard, M. Muterspaugh, and M. Ghosh, “Spectrum sensing simulation model,” *IEEE 802.22-06/0028r10*, 2006.
- [82] A. Bishnu and V. Bhatia, “DTV signal capture,” Apr. 2017. [online]. <http://iiti.ac.in/Downloads/PAFW/PAFW/>.
- [83] N. Tadayon and S. Aïssa, “A multichannel spectrum sensing fusion mechanism for cognitive radio networks: Design and application to IEEE 802.22 WRANs,” *IEEE Trans. Cognitive Commun. Networking*, vol. 1, no. 4, pp. 359–371, 2015.
- [84] A. Sharma and K. K. Paliwal, “Fast principal component analysis using fixed-point algorithm,” *Pattern Recog. Lett.*, vol. 28, no. 10, pp. 1151–1155, 2007.
- [85] I. Horev, F. Yger, and M. Sugiyama, “Geometry-aware principal component analysis for symmetric positive definite matrices,” *Machine Learning*, vol. 106, no. 4, pp. 493–522, 2017.
- [86] M. Marcus and H. Minc, *A Survey of Matrix Theory and Matrix Inequalities*. Courier Corporation, 1992.
- [87] J. K. Tugnait, L. Tong *et al.*, “Single-user channel estimation and equalization,” *IEEE Signal Process. Mag.*, vol. 17, no. 3, pp. 17–28, 2000.
- [88] S. Lin and D. J. Costello, *Error Control Coding*. Pearson Education India, 2004.
- [89] T. Li, W. H. Mow, and M. Siu, “Joint erasure marking and list Viterbi algorithm for decoding in unknown non-Gaussian noise,” *IEEE Trans. Wireless Commun.*, vol. 7, no. 3, pp. 787–792, 2008.

- [90] S. Al-Sayed, A. M. Zoubir, and A. H. Sayed, “Robust adaptation in impulsive noise,” *IEEE Trans. Signal Process.*, vol. 64, no. 11, pp. 2851–2865, 2016.
- [91] N. Salman, I. Rasool, and A. H. Kemp, “Overview of the IEEE 802.15.4 standards family for low rate wireless personal area networks,” in *Proc. IEEE Int. Symposium Wireless Commun. Syst.*, York, UK, 2010, pp. 701–705.
- [92] F. Yang and X. Zhang, “BER and SER analyses for M-ary modulation schemes under symmetric alpha-stable noise,” in *Proc. IEEE Global Commun.*, Austin, TX, USA, 2014, pp. 3983–3988.
- [93] A. Martian, “Real-time spectrum sensing using software defined radio platforms,” *Telecommun. Syst.*, vol. 64, no. 4, pp. 749–761, 2017.
- [94] R. Gandhiraj and K. Soman, “Modern analog and digital communication systems development using GNU Radio with USRP,” *Telecommun. Syst.*, vol. 56, no. 3, pp. 367–381, 2014.
- [95] M. Khurram and S. H. Mirza, “A general purpose processor based IEEE 802.11a compatible OFDM receiver design,” in *Proc. IEEE GCC Conf.*, Manama, Bahrain, 2006, pp. 1–5.
- [96] J. Demel, S. Koslowski, and F. K. Jondral, “A LTE receiver framework using GNU Radio,” *J. Signal Process. Syst.*, vol. 78, no. 3, pp. 313–320, 2015.
- [97] A. A. Hussain, N. Tayem, M. O. Butt, A.-H. Soliman, A. Alhamed, and S. Alshebeili, “FPGA hardware implementation of DOA estimation algorithm employing LU decomposition,” *IEEE Access*, vol. 6, pp. 17 666–17 680, 2018.
- [98] H. Rabah, A. Amira, B. K. Mohanty, S. Almaadeed, and P. K. Meher, “FPGA implementation of orthogonal matching pursuit for compressive sensing reconstruction,” *IEEE Trans. Very Large Scale Integr. Syst.*, vol. 23, no. 10, pp. 2209–2220, 2015.

- [99] S. Mhaske, D. Uliana, H. Kee, T. Ly, A. Aziz, and P. Spasojevic, “A 2.48 Gb/s FPGA-based QC-LDPC decoder: An algorithmic compiler implementation,” in *Proc. IEEE Sarnoff Symp.*, Newark, NJ, USA, 2015, pp. 88–93.
- [100] “LabVIEW Communications 802.11 Application Framework 1.1 White Paper,” Tech. Rep., 2007.
- [101] A. Viterbi, “Error bounds for convolutional codes and an asymptotically optimum decoding algorithm,” *IEEE Trans. Inf. Theory*, vol. 13, no. 2, pp. 260–269, 1967.
- [102] R. Gallager, “Low-density parity-check codes,” *IRE Trans. Inf. Theory*, vol. 8, no. 1, pp. 21–28, 1962.
- [103] Y. S. Cho, J. Kim, W. Y. Yang, and C. G. Kang, *MIMO-OFDM Wireless Communications with MATLAB*. John Wiley & Sons, 2010.
- [104] P. Atungire, T. F. Rahman, F. Granelli, and C. Sacchi, “Open-field emulation of cooperative relaying in LTE-A downlink using the GNU radio platform,” *IEEE Network*, vol. 28, no. 5, pp. 20–26, 2014.
- [105] S. Zahedpour, S. Feizi, A. Amini, M. Ferdosizadeh, and F. Marvasti, “Impulsive noise cancellation based on soft decision and recursion,” *IEEE Trans. Instr. Meas.*, vol. 58, no. 8, pp. 2780–2790, Aug. 2009.
- [106] M. Soltanolkotabi, A. Amini, and F. Marvasti, “OFDM channel estimation based on adaptive thresholding for sparse signal detection,” in *Proc. IEEE 17th European Signal Process. Conf.*, Glasgow, Scotland, Aug. 2009, pp. 1685–1689.
- [107] B. Chen, L. Xing, J. Liang, N. Zheng, and J. C. Principe, “Steady-state mean-square error analysis for adaptive filtering under the maximum correntropy criterion,” *IEEE Signal Process. Lett.*, vol. 21, no. 7, pp. 880–884, 2014.

- [108] N. R. Yousef and A. H. Sayed, “A unified approach to the steady-state and tracking analyses of adaptive filters,” *IEEE Trans. Signal Process.*, vol. 49, no. 2, pp. 314–324, 2001.
- [109] B. Lin, R. He, X. Wang, and B. Wang, “The steady-state mean-square error analysis for least mean  $p$ -order algorithm,” *IEEE Signal Process. Lett.*, vol. 16, no. 3, pp. 176–179, 2009.
- [110] S. Haykin, *Adaptive Filter Theory*. Prentice Hall, 2002.

# List of publications

## Patents:

1. A. Bishnu, and V. Bhatia, "Method and Apparatus for Low Complexity Natural Gradient Based OFDM Channel Estimator," Application no. 201621034423, (Published).
2. A. Bishnu, and V. Bhatia, "Method and Apparatus for Detection of Active Taps Location in OFDM System," Application no. 201621036738, (Published).
3. A. Bishnu, and V. Bhatia, "Method and Apparatus for Low Power Source Spectrum Sensing," Application no. 201721021637, (Published).

## Book Chapter:

1. A. Bishnu, and V. Bhatia, "Cognitive Radio Networks: IEEE 802.22 Standards," in *Sensing Techniques for Next Generation Cognitive Radio Networks*, A. Bagwari, J. Bagwari, and G. S. Tomar, Hershey PA, USA, IGI Global, 2018, pp. 27-50.

## Journals:

1. A. Bishnu, and V. Bhatia, "Convergence Analysis of Zero Attracting Natural Gradient Non-Parametric Maximum Likelihood Algorithm," *IEEE Trans. Circuits Syst. II, Exp. Briefs*, 2018 (Accepted).
2. A. Bishnu, and V. Bhatia, "Receiver for IEEE 802.11ah in Interference Limited Environment," *IEEE Internet of Things J.*, vol. 5, no. 5, pp. 4109-4118, 2018.
3. A. Bishnu, and V. Bhatia, "LogDet Covariance based Spectrum Sensing under Colored Noise," *IEEE Trans. Veh. Technol.*, vol. 67, no. 7, pp. 6716-6720, 2018.

4. A. Bishnu, and V. Bhatia, "Grassmann Manifold based Spectrum Sensing for TV White Space," *IEEE Trans. Cognitive Commun. Networking*, vol. 4, no. 3, pp. 462-472, 2018.
5. A. Bishnu, and V. Bhatia, "An IEEE 802.22 Transceiver Framework and its Performance Analysis on Software Defined Radio for TV White Space," *Springer Telecommun. Syst.*, vol. 68, no. 4, pp. 657-668, 2018.
6. A. Bishnu, and V. Bhatia, "Sparse Channel Estimation for Interference Limited OFDM systems and its Convergence Analysis," *IEEE Access*, vol. 5, pp. 17781-17794, 2017.
7. A. Bishnu, and V. Bhatia, "Iterative Time-Domain Based Sparse Channel Estimation for IEEE 802.22," *IEEE Wireless Commun. Lett.*, vol. 6, no. 3, pp. 290-293, 2017.

#### Conferences:

1. A. Bishnu, and V. Bhatia, "Algorithmic Compiler based FPGA Implementation of Iterative-Time Domain Algorithm for Sparse Channel Estimation," in *Proc. IEEE Int. Conf. on Advanced Networks and Telecommun. Sys. (IEEE ANTS)*, (Accepted) 2018.
2. A. Bishnu, S. K. Das, M. Soni, and V. Bhatia, "Comparative Analysis of Low Cost Photodetectors for Visible Light Communication," in *Proc. IEEE Int. Conf. on Advanced Networks and Telecommun. Sys. (IEEE ANTS)*, (Accepted) 2018.
3. A. Bishnu, and V. Bhatia, "A Zero Attracting Natural Gradient Non-Parametric Maximum Likelihood Algorithm for Sparse Channel Estimation," in *Proc. IEEE Global Commun. Conf. (IEEE GLOBECOM)*, Singapore, pp. 1-6, 2017.
4. S. Parvez, A. Bishnu, and V. Bhatia, "Performance comparison of Space Frequency Block Codes and Maximum Ratio Receiver Combining in the presence

- of Co-Channel Interference for LTE,” in *Proc. IEEE Conf. Inform., Commun. Technol.(IEEE CICT)*, Gwalior, India, pp. 1-6. 2017.
5. A. Bishnu, and V. Bhatia, “Natural Gradient Non-Parametric Maximum Likelihood Algorithm for Sparse Channel Estimation in Non-Gaussian Noise,” in *Proc. IEEE Signal Process. Commun. (IEEE SPCOM)*, Bengaluru, India, pp. 1-5, 2016.
  6. A. Bishnu, and V. Bhatia, “On Performance Analysis of IEEE 802.22 (PHY) for COST-207 Channel Models,” in *Proc. IEEE Conf. Standards Commun. Networking (IEEE CSCN)*, Tokyo, Japan, pp. 66-72, 2015.